HIGH-CAPACITY COMMUNICATION SYSTEMS USING ADVANCED OPTICAL AND WIRELESS TECHNOLOGIES

A Dissertation
Presented to
The Academic Faculty

by

Ming Zhu

In Partial Fulfillment
of the Requirements for the Degree
Doctor of Philosophy in the
School of Electrical and Computer Engineering

Georgia Institute of Technology
May, 2015

HIGH-CAPACITY COMMUNICATION SYSTEMS USING ADVANCED OPTICAL AND WIRELESS TECHNOLOGIES

Approved by:

Dr. Gee-Kung Chang, Advisor
School of Electrical and Computer Engineering
Georgia Institute of Technology

Dr. Xiaoli Ma
School of Electrical and Computer Engineering
Georgia Institute of Technology

Dr. John R. Barry
School of Electrical and Computer Engineering
Georgia Institute of Technology

Dr. Umakishore Ramachandran
School of Computer Science
Georgia Institute of Technology

Dr. Ali Adibi
School of Electrical and Computer Engineering
Georgia Institute of Technology

Date Approved: February 19, 2015

To my family, boyfriend, and friends,

for their unconditional support and encouragement

ACKNOWLEDGEMENTS

I would like to take this great opportunity to express my sincere gratitude to the many people who made this dissertation possible.

First, I am very grateful to my advisor, Professor Gee-Kung Chang. He fostered an exceptionally innovative research environment which inspired me to explore novel theories and experiments for integrated optical wireless access networks. His vast industry experience and visionary academic leadership were crucial catalysts for my growth as a researcher. I am extremely fortunate to have him guiding me in the past five years, and I look forward to his support and advice in my upcoming professional career.

I would also like to thank Professor Xiaoli Ma, Professor John R. Barry, Professor Ali Adibi, and Professor Umakishore Ramachandran for serving as my PhD thesis committee members and their valuable suggestions on my dissertation.

Finally, I would like to thank all my colleagues in my research group for their unending support, encouragement, as well as friendship that have accompanied me during my journey at Georgia Tech. Thanks to Hung-Chang Chien, Yu-Ting Hsueh, Shu-Hao Fan, Jesse Hsin, Cheng Liu, Jing Wang, Lin Cheng, Mu Xu, Feng Lu, Md Ibrahim Khalil, and many other graduate students and researchers whom I have been working with during my PhD study.

TABLE OF CONTENTS

ACKNOWLEDGEMENTS ..... **iv**

LIST OF TABLES ..... **viii**

LIST OF FIGURES ..... **ix**

LIST OF ABBREVIATIONS ..... **xiv**

SUMMARY ..... **xvii**

CHAPTER 1 INTRODUCTION **1**

1.1 Motivation 1

1.2 Research Background and Challenges 6

1.2.1 Radio-over-Fiber (RoF) Systems for Wireless Broadband Access 7

1.2.2 Optical Mobile Backhaul (MBH) and Mobile Fronthaul (MFH) 13

1.3 Outline 21

CHAPTER 2 MULTI-BAND MULTI-SERVICE ROF SYSTEMS **23**

2.1 Introduction 23

2.2 All-Band and Band-Mapped Mm-Wave RoF System Overview 24

2.3 Wi-Fi, WiMAX, and 60-GHz Mm-Wave in an All-Band DWDM-RoF-PON 29

2.4 Real-Time TV, Wi-Fi, and Gigabit Data in a Band-Mapped 60-GHz RoF System 34

2.5 Summary 41

CHAPTER 3 OFDMA-BASED MOBILE BACKHAUL AND LOW-LATENCY SYNCHRONOUS CLOCK DISTRIBUTION AND RECOVERY **42**

3.1 Introduction 42

3.2 Synchronous Clock Distribution and Recovery for DWDM-OFDMA-Based Optical MBH 43

3.2.1 Architecture and Synchronization Requirements 43

3.2.2 Operational Principles 47

3.2.3 Experimental Setup and Results 48

3.3 Synchronous Clock Distribution and Recovery for Coherent UDWDM-OFDMA-Based Optical MBH 58

3.3.1 Architecture and Operational Principles 59

3.3.2 Experimental Setup and Results 61

3.4 Summary 65

CHAPTER 4 SPECTRALLY-EFFICIENT OPTICAL FIBER SOLUTIONS FOR MOBILE FRONTHAUL 67

4.1 Introduction 67

4.2 MFH Supporting LTE-Advanced Carrier Aggregation and 8×8 MIMO 68

4.2.1 Architectures and Performance Requirements 68

4.2.2 SCM Transmission in the Optical MFH 73

4.2.3 Real-Time MFH Testbed with Video Streaming 82

4.3 Spectrally-efficient Structures for MFH UL 86

4.3.1 Motivation and Technical Challenges 86

4.3.2 Architectures and Operational Principles 87

4.3.3 Experimental Setups and Results 94

4.4 Summary 102

CHAPTER 5 CONCLUSIONS 105

5.1 Contributions 105

5.2 Future Research Topics..... 107

REFERENCES..... 110

VITA..... 117

LIST OF TABLES

Table 1. CPRI line bit rate option list 19

Table 2. Mobile backhaul synchronization requirements 45

LIST OF FIGURES

Figure 1. The evolution of transmission capacity in optical fibers reported by state-of-the-art laboratory transmission demonstrations [1]. 2

Figure 2. Mobile video will generate over 69 percent of mobile data traffic by 2018..... 2

Figure 3. Tools to increase wireless data capacity. 3

Figure 4. Wireless spectrum allocation for selected commercial systems in the United State and potential applications in the future. 4

Figure 5. Fiber is expected to make up an increasing portion of installed mobile backhaul connections [10]. 6

Figure 6. Schematic structure of the radio-over-fiber system..... 9

Figure 7. Backhaul and fronthaul network architectures. 17

Figure 8. Traditional RAN and Cloud-RAN architectures. 17

Figure 9. System architectures of (a) all-band RoF and (b) band-mapped 60-GHz RoF for unified multi-service optical-wireless access networks. 25

Figure 10. Spectrum allocations in (a) all-band RoF and (b) band-mapped 60-GHz RoF..... 27

Figure 11. Experimental setup of the all-band DWDM-RoF-PON system delivering legacy Wi-Fi, WiMAX, and advanced 60-GHz services. 29

Figure 12. (a)-(c) Optical spectra measured at locations from a to c in Figure 11. (d) Electrical spectrum for the Wi-Fi and WiMAX signals after the PD. 30

Figure 13. EVM of the (a) 2.5-GHz Wi-Fi-like signal with a constellation at EVM = 0.082, and (b) 5.8-GHz WiMAX-like signal with a constellation at EVM = 0.078. 32

Figure 14. BER performances and eye diagrams for the (a) downconverted downstream mm-wave signal and (b) the upstream signal. 33

Figure 15. Experimental setup of the band-mapped 60-GHz RoF system for TV, Wi-Fi, and OOK data. 34

Figure 16. (a) and (b) Optical spectra measured at locations a, b1, and b2 in Figure 15. (c) Electrical spectrum measured at location c in Figure 15..... 35

Figure 17. Wi-Fi throughput vs. received optical power for different fiber lengths. 38

Figure 18. Wi-Fi throughput in 20-sec interval for conventional Wi-Fi wireless link and multi-service 60-GHz RoF system. 38

Figure 19. BER vs. received optical power of the OOK data, with and without Wi-Fi. 39

Figure 20. (a) Internet access via band-mapped Wi-Fi in 60-GHz RoF. (b) TV signal alone in 60-GHz RoF. (c) TV signal in the multi-service 60-GHz RoF. 40

Figure 21. System architecture of DWDM-OFDMA-based MBH and synchronization requirements. 44

Figure 22. Schematic diagram of low-latency clock distribution and recovery principles for DWDM-OFDMA-based 4^{+}G optical MBH. (a) Electrical spectrum of the combined signal. 46

Figure 23. Experimental setup of the DWDM-OFDMA-based MBH with the proposed low-latency synchronization scheme. 50

Figure 24. (a) and (e) are electrical spectra measured at point a and e in Figure 23. (b)-(d) are optical spectra at 0.02 nm resolution measured at point b to d in Figure 23. 50

Figure 25. BER for OFDMA signals using 10-GHz linear PIN + TIA optical receiver. 52

Figure 26. BER of OFDMA signals using 10-GHz APD + TIA optical receiver. 52

Figure 27. BER for C_{square} using 10-GHz linear PIN + TIA optical receiver. 53

Figure 28. BER for C_{square} using 10-GHz APD + TIA optical receiver. Electrical eye diagrams for (a) C_{square} after power combiner 2, (b) C_{square} with 7 channels and 40-km fiber, and (c) C_{square} with $OFDMA_2$, C_{sine2}, 7 channels, and 40-km fiber at received power of -23.3 dBm. 54

Figure 29. (a) Short term MTIE and (b) long term MIE vs. observation time interval for C_{square} after 40-km SSMF in the 7-λ DWDM-OFDMA system. C_{square} electrical BTB is also shown for reference. 56

Figure 30. (a) Short term MTIE and (b) long term MIE vs. observation time interval for C_{sine} after 40-km fiber transmission in the 7-λ system. C_{sine} electrical BTB is also shown. 57

Figure 31. Schematic diagram of the coherent UDWDM-OFDMA-based MBH with synchronous clock distribution and recovery. (a) Optical spectrum of the launched signal. (b) Electrical spectrum of the signal after coherent

detection (top), and waveform of the clock carried at f_c (bottom). (c) Electrical waveform of the envelope detector output, i.e., clock signal only. 60

Figure 32. Experimental setup of the proposed clock distribution and recovery scheme for coherent UDWDM-OFDMA-based MBH. 61

Figure 33. (a)-(c) The optical spectra (0.01nm resolution) measured at points a-c in Figure 32. (d) and (e) Electrical spectra measured at points d and e in Figure 32. Shown spectra (a)-(d) are for f_s = 12.5 GHz and f_c = 6.25 GHz. Spectrum (e) corresponds to the case f_s = 9 GHz and f_c = 4.5 GHz. 62

Figure 34. BER and constellation for the OFDMA signal with f_s = 12.5 GHz and f_c = 6.25 GHz. OFDMA constellation on λ_2 at BER = 3.3×10^{-3} with joint clock signal transmission over 40-km SSMF is also shown. 63

Figure 35. BER for the OFDMA signal on λ_1 vs. spectral spacing between f_c and OFDMA band edge. 63

Figure 36. BER for the OFDMA signal with f_s = 9 GHz and f_c = 4.5 GHz. 64

Figure 37. (a) Q-factor for the 50MHz OOK square clock. (b) Time-domain clock amplitude waveforms after the BPF (two clock cycles) and after the ED (repetitive clock cycles). 64

Figure 38. DWDM-PON for MFH using the conventional CPRI interface. 69

Figure 39. Proposed MFH architecture 1: DWDM-SCM-PON using conventional AWGs. The frequency conversion plan is inserted as inset (a). 71

Figure 40. Proposed MFH architecture 2: DWDM-SCM-PON using cyclic AWGs (CAWGs) and red-blue wavelength-division multiplexers (R/B WDMs). The wavelength plane is inserted as inset (a). 71

Figure 41. Experimental setup of the generic SCM transmission in the MFH. (a) Optical spectrum of the launched signal. (b) Electrical spectrum of the received 12 × 100-MHz LTE-A-like CA-signals and their images. 74

Figure 42. EVM vs. the number of IFs in the eBTB case and after 20-km transmission with a DML-based optical transmitter. 75

Figure 43. EVM vs. received optical power in three configurations: (a) L = 0 km, V_A = 700 mV; (b) L = 20 km, V_A = 700 mV; (c) L = 20 km, V_A = 350 mV. 77

Figure 44. EVM vs. received optical power with different modulation schemes and fiber length L: (a) 64-QAM, L=0; (b) 64-QAM, L=40 km; (c) 16-QAM, L=40 km; (d) QPSK, L=40 km. 79

Figure 45. Complete single-wavelength configuration with RF processing in the proposed SCM-based MFH. Inset (a)-(f): electrical spectra at selected locations. 81

Figure 46. EVM measurements with f_{RF1} = 2.46 GHz. OL: optical link. 81

Figure 47. EVM measurements with f_{RF2} = 2.6 GHz. 82

Figure 48. MFH testbed with real-time Wi-Fi video streaming integrated in the SCM system. (a) Picture of the Wi-Fi adapter connection. (b)-(e) Electrical spectra at selected locations. 83

Figure 49. Wi-Fi throughput in a 30-s interval for conventional Wi-Fi wireless link and the SCM-based MFH system. 84

Figure 50. Wi-Fi throughput vs. received optical power in the SCM-based MFH. 84

Figure 51. Average EVM of the 2^{nd}-12^{th} 64-QAM-OFDM CA-signals. 85

Figure 52. Proposed MFH architecture (1). DL and UL: DWDM-SCM-PON. (a) and (b) Downstream and upstream wavelength plan, respectively. 88

Figure 53. Proposed MFH architecture (2). DL: IFoF-DWDM-PON; UL: UDWDM over DWDM-PON with phase-noise-insensitive heterodyne detection. (a) and (b) Downstream and upstream wavelength plan, respectively. 91

Figure 54. Three conversion methods to real-valued baseband signal. 92

Figure 55. Experimental setup of the IFoF-based MFH UL. (a) and (b) Optical spectra (0.01nm resolution) measured at point a and b. (c) and (d) Electrical spectra obtained after the ADC and DSP for 20-km transmission and 20/40-km transmission cases. 96

Figure 56. EVM of the UL OFDM signal with respect to PDR. 96

Figure 57. EVM for the UL OFDM signal in BTB and 20-km SSMF cases. 97

Figure 58. EVM for the received UL OFDM signal from RRH_2 after 20-km fiber and signal from RRH_3 after 40-km fiber. 97

Figure 59. Experimental setup of the UDWDM-based MFH upstream. (a) Optical spectrum (0.01nm resolution) of the received signal and the LO. (b)-(d) Electrical spectra measured after the PD. f_1 = 2.5 GHz, f_2 = 3 GHz, f_3 = 3.3 GHz, f_4 = 3.5 GHz, f_5 = 4 GHz. 100

Figure 60. EVM for the OFDM signal at f_1. Constellations at EVM = 7.5% and 12.5% are inserted. 100

Figure 61. BER for the 100-Mb/s OOK signal. 101

Figure 62. BER for the 200-Mb/s OOK signal at f_1 with eye diagrams inserted..... 101

LIST OF ABBREVIATIONS

ADC	Analog-to-digital converter
APD	Avalanche photodiode
ASIC	Application specific integrated circuit
ASE	Amplified spontaneous emission
AWG	Arrayed-waveguide grating
AWG	Arbitrary waveform generator
BBU	Baseband unit
BER	Bit error rate
BERT	Bit error rate tester
BPF	Band-pass filter
BS	Base station
BTB	Back-to-back
BWA	Broadband wireless access
CA	Carrier-aggregated
CATV	Community antenna television
CAWG	Cyclic AWG
CC	Component carrier
CD	Chromatic dispersion
CO	Central office
CoMP	Coordinated Multipoint Transmission
CP	Cyclic prefix
CPRI	Common Public Radio Interface
C-RAN	Cloud radio access network
CW	Continuous wave
CWDM	Coarse wavelength division multiplexing
DAC	Digital-to-analog converters
DAS	Distributed antenna system
DC	Direct current
DEMUX	Demultiplexer
DFB	Distributed feedback
DL	Downlink
DML	Directly modulated laser
DMT	Discrete multitone
DOCSIS	Data Over Cable Service Interface Specification
DSB	Double sideband
DSL	Digital subscriber line
DSP	Digital signal processing
DWDM	Dense wavelength division multiplexing
ECL	External cavity laser
ED	Envelope detector
EDFA	Erbium-doped fiber amplifier
ENOB	Effective number of bits

E/O	Electrical-to-optical
ESA	Electrical spectrum analyzer
EVM	Error vector magnitude
FDM	Frequency division multiplexing
FEC	Forward error correction
FFT	Fast Fourier transform
FPGA	Field programmable gate array
FTTH	Fiber to the home
FTTN	Fiber to the node
GPS	Global positioning system
HDTV	High-definition television
HetNet	Heterogeneous network
HFC	Hybrid fiber-coaxial
IF	Intermediate frequency
IFFT	Inverse fast Fourier transform
IL	Interleaver
IM	Intensity modulator
IMDD	Intensity-modulation and direct-detection
IPTV	Internet Protocol television
IQ-MZM	In-phase/quadrature Mach-Zehnder modulator
LD	Laser diode
LL	Link loss
LO	Local oscillator
LPF	Low-pass filter
LTE	Long Term Evolution
LTE-A	Long Term Evolution-Advanced
MAC	Media access control
MBH	Mobile backhaul
MFH	Mobile fronthaul
MIMO	Multiple-input and multiple-output
Mm-wave	Millimeter wave
MS	Mobile station
MTIE	Maximum time interval error
MUX	Multiplexer
MZM	Mach-Zehnder modulator
OBSAI	Open Base Station Architecture Initiative
OCS	Optical carrier-suppression
O/E	Optical-to-electrical
OFDM	Orthogonal frequency-division multiplexing
OFDMA	Orthogonal frequency division multiple access
OL	Optical link
OLT	Optical line terminal
OMI	Optical modulation index
ONU	Optical network unit
OOK	On-off keying
OpEx	Operational expense

OSNR	Optical signal-to-noise ratio
PA	Power amplifier
PAPR	Peak-to-average power ratio
PC	Personal computer
PD	Photodiode
PDR	Pilot-to-data power ratio
PLL	Phase locked loop
PM	Phase modulator
Pol-Mux	Polarization multiplexing
PON	Passive optical network
PRBS	Pseudo random binary sequence
PTP	Precision Time Protocol
QAM	Quadrature amplitude modulation
QoS	Quality of service
QPSK	Quadrature phase-shift keying
RAU	Remote antenna unit
R/B WDM	Red-blue wavelength-division multiplexer
RF	Radio frequency
RN	Remote node
RoF	Radio-over-Fiber
RRH	Remote radio head
SCM	Subcarrier multiplexing
SCO	Sampling clock offset
SDM	Space division multiplexing
SDN	Software-defined networking
SNR	Signal-to-noise ratio
SSB	Single sideband
SSMF	Standard single mode fiber
STO	Symbol timing offset
SyncE	Synchronous Ethernet
TDM	Time division multiplexing
TIA	Transimpedance amplifier
TIE	Time interval error
TWDM	Time and wavelength division multiplexed
Tx	Transmitter
UE	User equipment
WDM	Wavelength division multiplexing
WLAN	Wireless local area network

SUMMARY

The increasing traffic demand from the use of 3G/4G, streaming, and other broadband wireless services exposes existing bottlenecks in the communications infrastructure and the coordination between the wireless network and its wired counterpart. While wireless systems are constantly evolving to newer generations and higher capacities, their supporting wired networks urgently require advancements in both architecture design and enabling technologies. New optical access systems specifically tailored for the unique natures of various wireless standards are investigated. This dissertation presents the design and experimental verification of high-capacity optical-wireless communication systems using advanced electrical and optical technologies.

Technologies such as high level modulation and multiple-input and multiple-output (MIMO) to increase the spectral efficiency is approaching the Shannon limit. New frequency bands with larger bandwidth are to be explored; for example, millimetre wave (mm-wave) spectrum range (30-300 GHz), especially the license-free spectrum located in 60 GHz. Although fiber-optic systems excel in the high-bandwidth core network, as bandwidth demand increases, more and more progress has been made towards the usage of fiber in the last mile. Radio-over-Fiber (RoF) technology has been proposed as a cost-effective optical access solution to support high-speed wireless communications, especially at the mm-wave band. Signal processing and coordination are centralized at the central office (CO), making the system economical and simple to build, operate, and maintain. Moreover, RoF systems are capable of delivering radio signals with different frequencies and protocols simultaneously. Therefore, the advantage of integrated fiber wireless systems

leads to the first research topic of this dissertation: multi-band multi-service RoF systems. With an emphasis on the uniformity of the RoF platform that accommodates both legacy wireless services and advanced mm-wave services, the first part of the dissertation presents two schemes - analog all-band RoF and band-mapped 60-GHz RoF - to cover distinct application scenarios. In the all-band RoF access architecture, lower RF signals, such as Wi-Fi and cellular signals, and 60-GHz signal are transmitted at their original carrier frequencies for both indoor and outdoor coverages. On the other hand, the band-mapped mm-wave RoF scheme, fully utilizing the wide 7-GHz bandwidth at 60 GHz, delivers multiple converged high-speed services only through 60-GHz wireless link, which is especially suited for in-building broadband wireless access. The experimental verification of an all-band RoF system featuring relaxed component requirement is introduced, followed by a real-time multi-service demonstration in the proposed band-mapped 60-GHz RoF system.

This dissertation also presents the design, analysis, and experimental demonstration of next-generation high-capacity cellular networks to keep up with the ever-growing bandwidth demand and performance requirements. New mobile backhaul (MBH) architectures based on orthogonal frequency division multiple access (OFDMA) are proposed along with a simple and low-latency clock distribution and recovery scheme. The transmission of OFDMA signals in the dense wavelength division multiplexing (DWDM) network with flexible clock rates and DSP-free clock recovery is implemented. Also, a spectrally-efficient, low-complexity clock distribution and recovery scheme for OFDMA-based MBH in coherent ultra-dense WDM (UDWDM) system is demonstrated. Finally, mobile fronthaul (MFH) architectures based on subcarrier multiplexing (SCM) technology,

which significantly reduces the requirements on both the number of wavelengths per cell site and the optical bandwidth of the optical transceivers, are systematically investigated. Additionally, two upstream schemes, tailored for the uplink (UL), are introduced to maintain low complexity, and more importantly, to achieve high spectral efficiency by wavelength sharing.

Therefore, Internet-access-oriented optical-wireless systems using Wi-Fi and other emerging mm-wave technologies are developed along with the optical fronthaul and backhaul for cellular networks in this dissertation. Moreover, with the proposed techniques, heterogeneous networks can be seamlessly provided even with different services, radio nodes, and performance requirements.

CHAPTER 1

INTRODUCTION

1.1 Motivation

In the rapidly-changing "Information Age", individuals are able to share information freely and have instant access to information in various kinds of forms, which was difficult or impossible previously. Bringing about a fast technological evolution in daily life, as well as educational advancements, the Information Age has ushered in rapid global communications and networking to shape modern society. The enabling technologies behind the overwhelming explosion of the data traffic largely rely on optical fiber communication. The first working fiber-optical data transmission system was demonstrated by Manfred Börner at Telefunken Research Labs in Ulm, Germany, in 1965, and patented in 1966. Charles K. Kao and George A. Hockham of a British company, Standard Telephones and Cables, made fibers a practical communication medium for the first time by identifying the right fiber material to achieve small attenuations in transmission, and this earned Kao a Nobel Prize in Physics in 2009. Because of the tremendous advantages in signal transmission over electrical cables such as low loss, enormous bandwidth, and no crosstalk among fiber cables, optical fibers have largely replaced copper wires in core networks. More than 1.5 billion kilometers of optical fiber have been installed around the globe. Owing to a series of significant advancements of fiber optics technologies such as erbium-doped fiber amplifiers (EDFA), wavelength

division multiplexing (WDM) and space division multiplexing (SDM), newly reported fiber capacities remarkably reach one hundred trillion bit/s, as shown in Figure 1 [1].

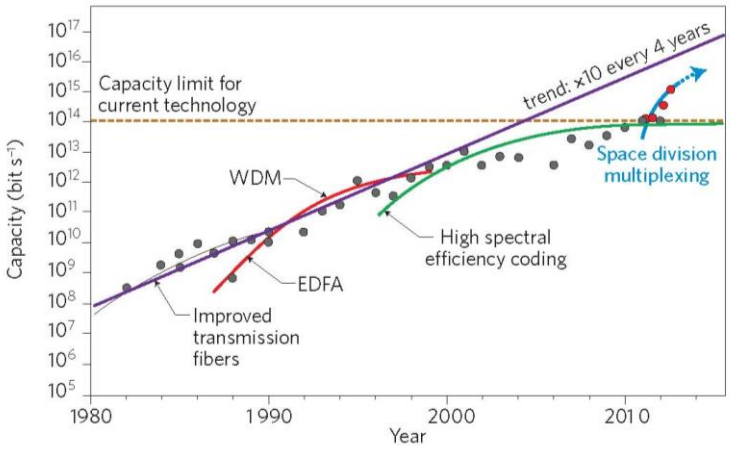

Figure 1. The evolution of transmission capacity in optical fibers reported by state-of-the-art laboratory transmission demonstrations [1].

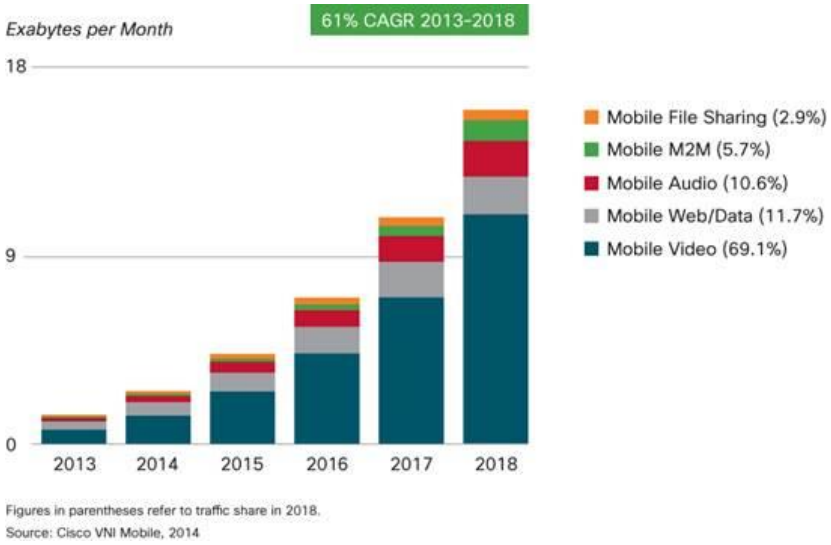

Figure 2. Mobile video will generate over 69 percent of mobile data traffic by 2018.

At the same time, mobile data traffic is gaining lion share of the total IP traffic through an even faster growth rate. Propelled by emerging mobile devices such as smart

phones and tablets, mobile data traffic is projected to increase 11-fold between 2013 and 2018 in the Cisco global mobile data traffic forecast [2]. Mobile video, in particular, will increase 14-fold, accounting for 69 percent of total mobile data traffic by 2018, as shown in Figure 2. On one hand, the resulting huge traffic load indicates that it is having an immediate impact on mobile network today, and will be more intense in the future. On the other hand, low latency and quality of service (QoS) inevitably arise as network requirements in addition to the capacity increase.

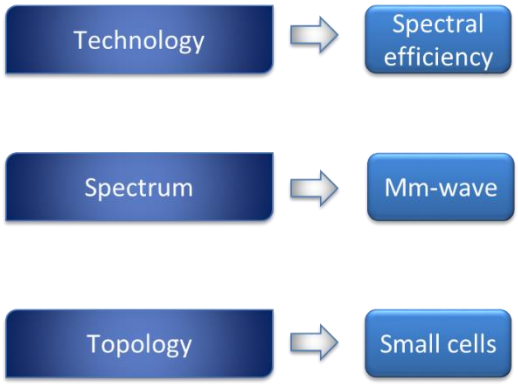

Figure 3. Tools to increase wireless data capacity.

In wireless communication networks, there are three major tools that can be used to increase wireless data capacity, as illustrated in Figure 3. Currently, broadband wireless access (BWA) standards aiming at lower radio frequencies (RFs), such as Wi-Fi [3], WiMAX [4], and Long Term Evolution (LTE) [5] are the dominant technologies for wireless communications because of their universal presence and mobility. However, the lower RF bands are becoming overly congested, as shown in Figure 4. Technologies such as high level modulation and multiple-input and multiple-output (MIMO) can increase the spectral efficiency. For example, LTE-Advanced (LTE-A) and WiMAX 2, can use up to

8×8 MIMO and 128 quadrature amplitude modulation (QAM) in downlink (DL) direction [6]. But it can only take us so far because it is bounded by the Shannon theorem. Secondly, new, higher frequency bands with larger bandwidth need to be further explored since the wireless spectrum below 3 GHz is allocated for many different uses and very congested, as shown in Figure 4. Millimetre wave (mm-wave) spectrum range (30-300 GHz) is recently advocated and investigated to be a promising spectrum for potential wireless communication systems. The abundant license-free spectrum located in 60 GHz has particularly been studied, standardized, and used in various applications [7]. Spectra at 28 GHz, 38 GHz, and 70-80 GHz are also promising for next-generation cellular systems. Finally, high density small cells can provide more capacity than a system using larger cells for a given service area and frequency bandwidth. Much mobile data activity actually takes place in indoor environments. This traffic may be offloaded onto Wi-Fi, femtocells, and picocells. It is noted that high frequencies such as 60 GHz are in fact suitable for small cells due to the high attenuation from free-space path loss and atmospheric absorption, and this minimizes co-channel interference in small cell systems.

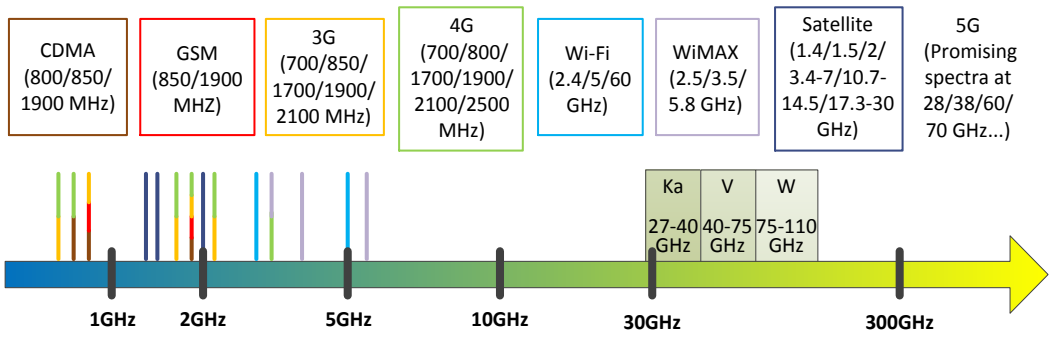

Figure 4. Wireless spectrum allocation for selected commercial systems in the United State and potential applications in the future.

As a result, the massive traffic demand is fundamentally changing the wireless network and exposing existing bottlenecks in the communications infrastructure. Although fiber-optic systems excel in the high-bandwidth core network, as bandwidth demand increases, more and more progress has been made towards the usage of fiber in the last mile. Fiber to the home (FTTH) service has been provided in countries such as US, Japan, and South Korea, in replace of digital subscriber line (DSL). The targeted user data speed is anticipated to reach 1 Gb/s in the near future. The same trend can be found in the realm of mobile backhaul (MBH) [8] and the lately introduced mobile fronthaul (MFH) [9]. Backhaul accounts for the portion between the core network and the small subnetworks at the "edge" of the entire hierarchical telecommunication network. There are three main types of MBH physical mediums: fiber, copper, and microwave. High-capacity fiber is making up an increasing portion of installed MBH connections, as illustrated in Figure 5 [10]. Optical networks provide low latency and high bandwidth for wireless backhaul applications. The microwave portion, on the other hand, will largely remain the same since it is inexpensive, mobile, and easy to deploy. However, fiber plays the major role in the emerging MFH. Fronthaul separates the base station (BS) functions into principle radio components in remote radio heads (RRHs) and signal processing functions in baseband units (BBUs). The links between these two are optical fibers. However, the current MFH solutions are rather short-term approaches, and need improvements in both topology and technology.

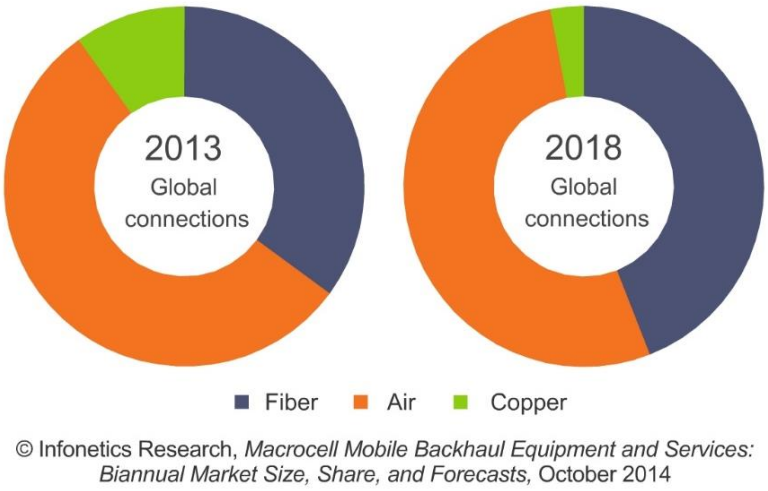

Figure 5. Fiber is expected to make up an increasing portion of installed mobile backhaul connections [10].

The need for high-capacity, reliable, and scalable optical-wireless networks for the next-generation BWA is urgent. From the service aspect, multi-service co-existence is important. An ideal system would be one that offers data access anywhere anytime for users with smart service assignment and selection. In the meantime, investigations on next-generation high-capacity cellular networks are necessary in order to keep up with the ever-growing bandwidth demand and performance requirement. In the fronthaul architecture, optimization of the spectrum utilization needs to be investigated in order for the maximum number of users to be provided in a cost-effective way. As for the backhaul, new network architecture and synchronization techniques are to be explored.

1.2 Research Background and Challenges

The background of the research on high-capacity communication systems using integrated optical and wireless technologies is introduced in this section. Three key research topics

are included: (1) Radio-over-Fiber (RoF) systems for wireless broadband access, (2) optical MBH, and (3) MFH. The challenges of all research areas are also introduced.

1.2.1 Radio-over-Fiber (RoF) Systems for Wireless Broadband Access

The proliferation of smart mobile devices is essentially changing Internet traffic patterns and both wireless and wired network infrastructure. Wireless local area network (WLAN) [3] link speeds are expected to grow towards multi-gigabits/second, propelled by emerging applications such as high-definition television (HDTV), interactive video service, and online gaming. Meanwhile, data rates targets in remarkable 4G standards, such as LTE and LTE-A, have been set to 100 Mb/s and 1 Gb/s per cell site, respectively. However, since the available spectrum for lower RF bands are very limited, advanced modulation formats and multiplexing methods have been investigated extensively. For example, the targeted DL peak data rate in the LTE-A exceeds 1 Gb/s through several techniques, including 64-QAM and eight-layer MIMO. Meanwhile, deploying smaller cells at high frequencies is considered a promising solution to accommodate the sharp data rate increase, reuse the wider spectrum, and reduce interference with existing lower frequency wireless services. Approximately 7-GHz unlicensed bandwidth at 60 GHz is available in North American, Korea, Europe and Japan. However, mm-wave signals will suffer a large free-space propagation loss. Moreover, 60-GHz signal is highly attenuated by atmospheric gases, especially water vapor and oxygen [11]. This seemingly adverse phenomenon, however, can actually benefit the close-range gigabit wireless data transfer applications since nearby transmitters will not interfere with each other and minimize co-channel interference in small cell systems. Several emerging 60-GHz standards, including Wireless HD [12], IEEE 802.15.3c [13], and ECMA 387 [14], are primarily targeting very high data rates over 2

Gb/s for applications such as video streamers and HDTV. IEEE 802.11ad, also known as "WiGig", is also a published standard that aims to achieve a theoretical maximum throughput of up to 7 Gb/s per 2.16 GHz channel bandwidth as a new tri-band Wi-Fi solution.

In order to connect large numbers of small cells with the mobile switching center through high-speed backhaul network, RoF technology has been proposed as a cost-effective solution to support high-speed small-cell wireless communications especially at 60GHz mm-wave band [15]. Figure 6 shows a typical schematic structure of the RoF system. Multiple signals for wireless services are generated, processed, and multiplexed in the central office (CO). Different from conventional optical networks that deliver digital baseband signals through fiber, radio signals are modulated onto light through the RF/optical interface in the CO. Two strategies can be used to perform this conversion: direct modulation and external modulation [16]. In the direct modulation, a directly modulated laser (DML) is driven by the data signal and the intensity of the optical output is modulated directly. In the external modulation, a continuous wave (CW) laser is used to emit light, and connected to an external modulator that modulates the applied electrical signal. There are two main types of modulators for external modulation: intensity modulator (IM) and phase modulator (PM). At the end of the fiber, signals are simultaneously emitted by radio antennas only after optical-to-electrical (O/E) conversion by a photodiode (PD). All signal processing and coordination happen at the CO, making the system economical and simple to build, operate, and maintain than typical wireless distribution networks. RoF systems deliver ready-to-use analog signals with no differentiation in protocols or interfaces, and thus greatly increase the flexibility,

scalability, and simplicity for future upgrade. At a lower carrier RF, transceiver modules with electrical-to-optical (E/O) and O/E conversions are commercially available. However, those transceivers for analog RF signals require better linearity than the ones designed for binary on-off keying (OOK) data. The dominant market for RoF technology today is the distribution of mobile signals over fiber to extend the range and capacity of radio systems indoors; so called fiber distributed antenna system (DAS).

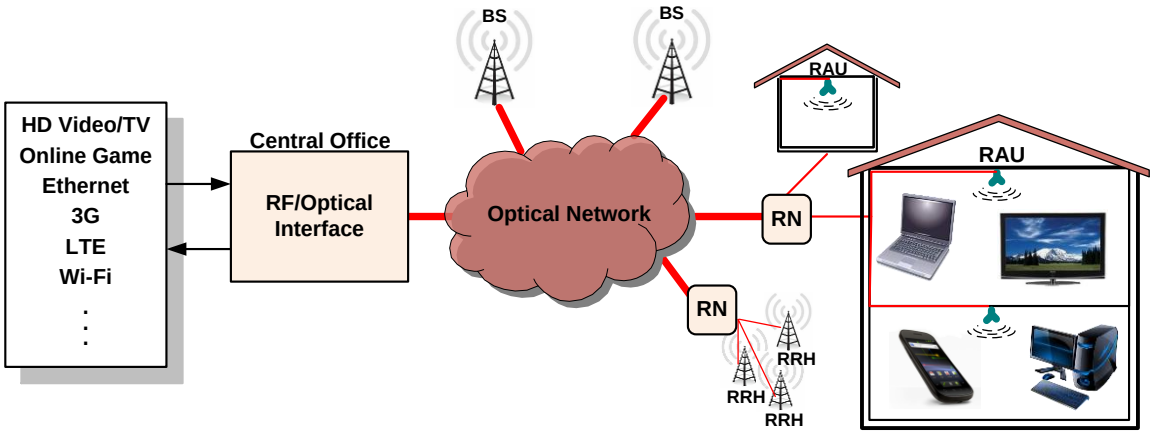

Figure 6. Schematic structure of the radio-over-fiber system.

However, it is noted that the electrical bandwidth limit of current available optoelectronics components is 40 GHz. For a RF signal with carrier frequency beyond 40 GHz, different modulation and detection methods are required. Research works on how to generate 60-GHz signals have been proposed, including techniques related to fiber nonlinearity [17], injection locking [18], and external modulation [19]-[22]. External modulation is the most widely used method because of its simplicity, reliability, and low energy consumption. The external intensity modulation realized by a dual-arm Mach-

Zehnder modulator (MZM) can have three different schemes: double sideband (DSB), single sideband (SSB), and optical carrier-suppression (OCS) [19]. Another mm-wave generation method is based on a more complicated modulator known as an integrated MZM, or in-phase/quadrature MZM (IQ-MZM). This modulator has been shown in previous studies to successfully generate mm-wave signals by using an OCS scheme with one pure optical subcarrier [20] as well as a frequency sextupling scheme [21]. For the mm-wave signal generation by PM, several optical sidebands are produced after driving the PM with a RF signal [22]. In particular, the mm-wave small cell system can benefit the most from RoF architecture due to its features in low attenuation and cost. As a result, large-scale RoF-based systems can be highly desirable and deployable.

As mentioned previously, multi-service co-existence is one of the desired features of communication systems. An example of current deployment would be the combined services of voice, Internet, and TV provided by telecommunication carriers and cable TV (CATV) operators. For instance, AT&T U-verse [23] delivers most of its service over a network consisting of fiber to the node (FTTN) and digital subscriber lines (DSLs). All services are in digital baseband format, i.e. Internet Protocol television (IPTV) and voice over IP. However, CATV companies uses hybrid fiber-coaxial (HFC) network to carry their service bundle. Different from U-verse, services are carried on RF signals in 5 MHz to 1000 MHz frequency band based on frequency division multiplexing (FDM). Data Over Cable Service Interface Specification (DOCSIS), the standard for high-bandwidth data transfer to an existing CATV system, has been updated to the 3.1 version that aims at 10 Gbit/s downstream and 1 Gbit/s upstream using 4096-QAM [24]. This latter approach with RF signals over fiber is in principle the same as RoF. As mm-wave band, specially the 60-

GHz range, becomes more and more prevalent, it is expected that the future RoF network is capable of transmitting multi-band multi-service radio signals at mm-wave band while keeping backward compatibility of legacy wireless services. ECMA 387 defines four channels from 57 GHz to 66 GHz, each of which is 2.16-GHz wide [14]. However, optically generating multi-band 60-GHz signals are still technically difficult. Several approaches to multi-band signals generation and transmission in 60-GHz RoF have been demonstrated. However, these works either used arbitrary waveform generator (AWG) to generate multi-band signals less than 2.5 GHz [25], [26], or transmitted up to two bands by electrical mixers [27]. In Chapter 2, a band-mapping scheme is developed accordingly to fit the existing wireless services and multi-gigabit mm-wave services into 60-GHz sub-bands. It is especially suitable for the indoor wireless access scenario. With the new 60-GHz universal interface, power consumption and component complexity can be greatly reduced. In other applications, lower RF signals and mm-wave signal are transmitted at their original carrier frequencies, giving a variety of coverage from hundreds of meters to several kilometers. A RoF system delivering various services is a promising architecture for fiber-connected massively distributed antennas in heterogeneous networks (HetNets) [28]. However, as mentioned earlier, signals at 40 GHz and beyond requires special optical upconversion techniques for downstream. In the previously reported work of generating and transmitting 2.4-GHz (Wi-Fi), 5.8-GHz (WiMAX), and 60-GHz optical mm-wave signals [29], sophisticated combination of interleavers (ILs) are used in both intelligent gateway router and BSs, which are not favorable for industrial deployment. Furthermore, this setup occupies huge spectrum (120-GHz wide) only for signals up to 60-GHz, and thus cannot be integrated in the spectrally-efficient dense wavelength division multiplexing

passive optical network (DWDM-PON) [30]. Therefore, the key technical innovation of a converged RoF system lies in the design of simple and efficient CO and remote access unit (RAU) to simultaneously integrate lower RF wireless services and mm-wave channels. To eliminate the complicated filtering components and high-bandwidth modulators and greatly increase the optical spectral efficiency, an all-band DWDM-RoF-PON system is introduced in the next Chapter, where Wi-Fi and WiMAX services are realized using subcarrier multiplexing (SCM) technology and the 60-GHz mm-wave signal is achieved by dual-wavelength heterodyne beating method. As for the upstream transmission, wavelength reuse methods have been proposed [31], [32]. They mostly require complicated optical filtering, large spectrum occupation, and fixed data format. Laser source in RAU is preferred in some situations for better flexibility and integration [33].

Architecture-wise, RoF system is desirable to be integrated with the WDM-PON infrastructure to achieve high scalability and efficient utilization of fiber resource. WDM is a technology that multiplexes a number of optical signals onto a single optical fiber by using different wavelengths. It is one of the major techniques in optics to increase fiber link capacity. The spectral grid for coarse WDM (CWDM) is standardized in ITU-T G.694.2, with a channel spacing of 20 nm [34]. ITU-T G.694.1 defines channel spacing for DWDM from 12.5 GHz to 100 GHz [35]. With the increasing bandwidth demand on broadband access, higher capacity PON has been an active research topic. The coherent ultra-dense WDM-PON (UDWDM-PON) is recognized for its wavelength selectivity, high spectral efficiency, enhanced power budget, and long reach [36]. UDWDM channels are very tightly spaced, i.e., with <12.5 GHz spacing. Traditionally, it is only designed for high-speed wired services. Integrating RoF system with coherent UDWDM-PON would

be challenging because the conventional detection scheme in the former system is direct detection while the latter one is coherent detection. In this dissertation, methods to integrate RoF with UDWDM-PON are explored for high spectral efficiency [37].

1.2.2 Optical Mobile Backhaul (MBH) and Mobile Fronthaul (MFH)

In addition to optical-wireless architectures for the WLAN, WiMAX, and potential mm-wave services for Internet access and data transfer, research works of this dissertation also contain the optical MBH [8] and MFH [9] for fourth-generation and beyond (4^{+}G) mobile telecommunications with an emphasis on high capacity and low latency.

As previously mentioned, backhaul links are mostly connected by copper, optical fiber, and microwave radio. Older generation networks – 2G and 3G – commonly rely on leased T1/E1 copper lines for the traditional backhaul connection between cell sites and BS controller [38]. T1/E1 lines are highly suitable for voice service because of its low latency, deterministic QoS, and inherent synchronization ability. However, as the number of mobile subscribers and the bandwidth demand per subscriber both significantly increase, mobile operators need to build large numbers of new high-capacity cell sites. As a result, T1/E1 copper lines would cost a major increase in operational expense (OpEx) and is no longer suitable for future MBH. To address these challenges, mobile carriers are working on the near-term migration from the legacy time division multiplexing (TDM)-based architecture to an all-packet Ethernet-based architecture for the backhaul. However, the original Ethernet is not designed for Carrier Class deployment and does not meet certain requirements, including, most importantly, synchronization. The two primary methods for timing and synchronization are Synchronous Ethernet (SyncE), as defined by the ITU-T in Study Group 15, Question 13 (Q13/15) and the Precision Time Protocol (PTP) as defined

by the IEEE 1588v2 standard [39]. SyncE provides accurate frequency distribution at the physical layer, but is not protocol-transparent; it requires that each node in the network be SyncE enabled, which might not suit all deployment scenarios. The PTP protocol distributes frequency and time synchronization via timing information carried by the packets, yet also needs customized hardware for timing measurements, and suffers from traffic-dependent synchronization accuracy. It has been suggested to combine SyncE and PTP to ensure end-to-end high accuracy [40]. However, this approach involves both physical and packet layer processing, and can also increase processing complexity and delay and pose a challenge to satisfying low-latency requirements of future MBH systems, particularly as data rate requirements for backhaul systems increase beyond 10 Gb/s per-channel.

Ethernet-based network might be good for the near future. In the meantime, in order to accommodate the tremendous mobile data traffic with more efficient and flexible spectrum utilization, new technologies based on coherent UDWDM and orthogonal frequency division multiple access (OFDMA) [41] have been proposed separately for future MBH systems. OFDMA-PON is quite different from the OOK-based system since it contains extra digital signal processing (DSP) which facilitates the dynamic resource allocation through the distribution of the subcarriers. Moreover, the OFDMA format has high spectral efficiency and robust dispersion tolerance. Consequently, it would be the right choice for a high-capacity and long-reach backhaul system. As part of this dissertation, a DWDM-OFDMA-based optical MBH with cost-effective intensity-modulation and direct-detection (IMDD) links is developed. From the technical perspective, synchronization is a fundamental requirement to realize all key features of a MBH. To practically implement

OFDMA-based optical MBH, new low-latency synchronization techniques are needed to provide symbol-level and system-level synchronizations in both the OFDMA transmitter and receiver for accurate real-time transmission [42]. In optical OFDM-based data access networks where latency is not a critical issue, the timing information can be embedded in the received OFDM signal and recovered through intensive DSP, introducing computational delays that may be too high for low-latency MBH applications. Recently, DSP-free synchronous clock distribution based on out-of-band [43] and in-band [44] clock transmissions and electrical filtering have shown for single-wavelength directly-detected optical OFDM systems. However, the frequency and time alignment performance with respect to 4^{+}G mobile backhaul requirements was not evaluated. Moreover, only fixed-rate rather than flexible clocks were considered in [43] and [44], and pre-scalers were needed to derive both low-frequency square wave clocks for digital circuits and high-frequency sine wave clocks for sensitive mixed-signal circuits, such as digital-to-analog converters (DAC) and analog-to-digital converters (ADC). A novel low-complexity and low-latency clock distribution and recovery scheme is also illustrated in this dissertation for the IMDD DWDM-OFDMA-based MBH with flexible clock rates and DSP-free electrical filtering. Compared to existing solutions, the proposed physical-layer approach requires no clock extraction processing thereby minimizing latency, is scalable to higher and variable data rates, and enables synchronous clock distribution without packet-based synchronization that may require hop-by-hop hardware/protocol specificity and network engineering to manage jitter. Moreover, the proposed centralized clock distribution architecture offers a natural compatibility with centralized software-defined networking (SDN)-based management envisioned for future mobile access networks.

Besides the integration of DWDM-PON and OFDMA, a coherent UDWDM-OFDMA-based MBH is also designed and experimentally verified to maximize both frequency and wavelength domain capacities. For OFDMA signal, conventional coherent detection followed by DSP for frequency offset and phase noise recovery can be applied. However, such intensive computation is not favorable for the recovery of clock signal. A spectrally-efficient yet DSP-free technique is thus required. In this dissertation, a novel clock distribution and recovery scheme for UDWDM-OFDMA-based MBH using optical SSB [45] modulation and DSP-free envelope detection is investigated.

Today's mobile internet traffic is surging, while the average revenue per user is flat or even decreasing slowly. To maintain profitability and growth, mobile operators must find solutions to reduce cost as well as to provide better services to the customers. Operators are now looking at deployment architectures using fibers to connect several RRHs at the antenna site with a centralized baseband processing. By contrast to the traditional backhaul architecture, this new method is called fronthaul. Figure 7 illustrates the locations where fronthaul and backhaul are in the complete network. Cloud radio access network (C-RAN) is a fronthaul architecture recognized by many operators and vendors that provides great benefits in controlling ongoing operational costs and also greatly increases the flexibility of the network [9], [46]. The comparison between a traditional RAN and the emerging C-RAN is shown in Figure 8. In the traditional RAN architecture, each tower is equipped with complicated and high power-consuming devices for the entire processing, controlling, and radio reception. This would lead to heavy expenditure for mobile operators to build and operate new cell sites. C-RAN, by separating base station functions into the principal processing and control functions in BBUs and radio

components in RRHs, manages network resources in a more efficient and proactive manner. BBUs are centralized and connected into one entity that is called a BBU pool. Immediately, air conditioning and other site support equipment's power consumption can be largely reduced. Furthermore, signals from RRHs can be routed to any BBU in the pool. Dynamic resource allocation among BBUs is thus enabled.

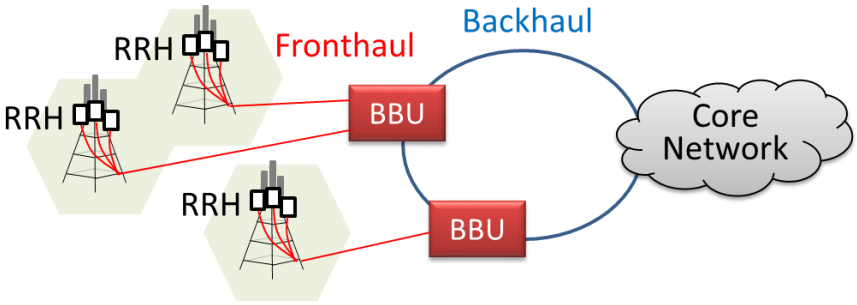

Figure 7. Backhaul and fronthaul network architectures.

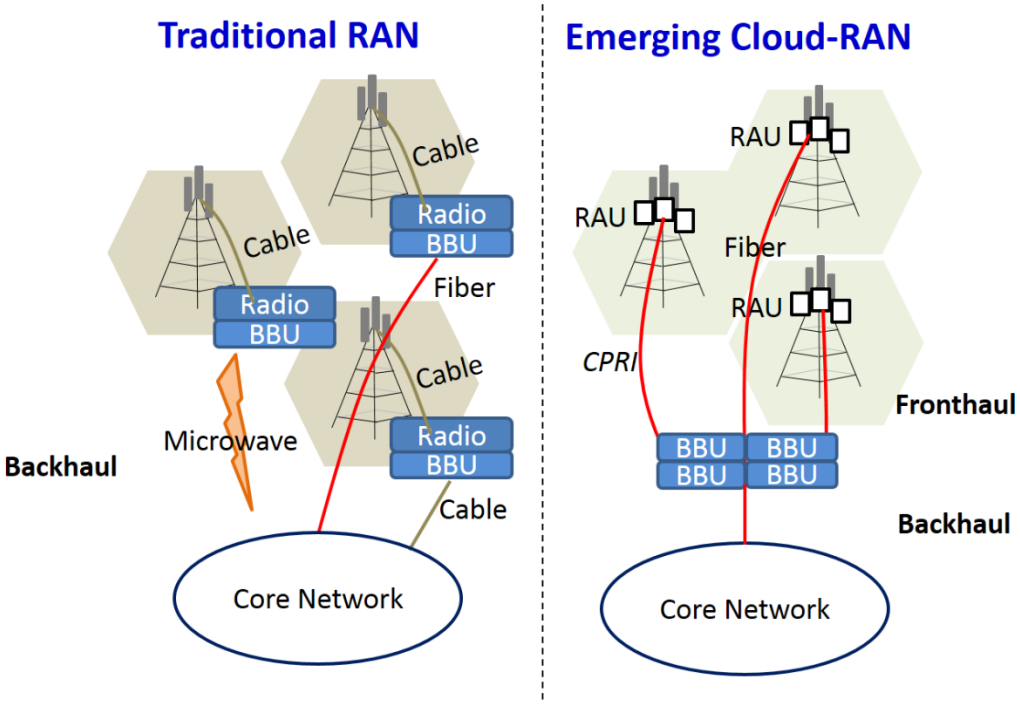

Figure 8. Traditional RAN and Cloud-RAN architectures.

Another benefit of fronthaul is that enhanced interference cancellation and mitigation techniques can be practically supported. For example, the newly developed Coordinated Multipoint Transmission (CoMP) feature introduced in LTE Release 11 is able to coordinate neighbor cells or sectors to enhance network performance at cell edges [47]. The higher latencies in a backhaul scenario make coordination methods unpractical for cells or sectors not sharing the same BBU. By contrast, a fronthaul can exchange and process real-time data among BBUs in a centralized manner, and minimized the delay and overhead.

The RRH can be linked to the BBU by an optical single mode fiber using a standard interface with a digital radio signal such as Common Public Radio Interface (CPRI) for the baseband transmit and receive signals [48]. CPRI encapsulates radio samples in a low-latency timeslot-like manner, offering a near zero jitter and bit error rate (BER). However, due to the sampling and quantization of the complex baseband orthogonal frequency-division multiplexing (OFDM) signals, CPRI is not bandwidth-efficient, e. g., requiring a fronthaul data rate of as high as 9.83 Gb/s for a 20-MHz wireless channel with 8×8 MIMO. Detailed line bit rate options are included in Table 1. Although compression techniques have been studied, they introduce additional delay and computation complexity while the resulting data rates are still relatively high [49], [50]. The problem will be more severe in the case of 4G LTE-A. To address the demand to further increase mobile data rates, LTE Release 10 publishes several major techniques to develop LTE towards LTE-A for the 4G mobile telecommunications [6], [47]. In Release 10, 8×8 MIMO, as a key enabler for achieving high spectral efficiency, is supported for DL. Parallel to the effort of increasing mobile communication capacity by technologies such as higher modulation format and

MIMO, more spectrum resources are also explored. In order to be backward compatible with previous standards, aggregation of LTE carriers are introduced in Release 10 as a mean to increase bandwidth. The component carrier (CC) can have a bandwidth up to 20 MHz and a maximum of 5 CCs can be aggregated [51]. For the deployment of such cell site with 3 RRHs (for 3 sectors), 5 aggregated 20-MHz carriers (100-MHz bandwidth), and 8×8 MIMO, there are 120 20-MHz signals to/from a radio unit in total. Accordingly, the aggregated one-way traffic per cell would be approximately 150 Gb/s if CPRI would be used.

Table 1. CPRI line bit rate option list

CPRI line bit rate option	Line bit rate
1	614.4 Mbit/s
2	1228.8 Mbit/s (2 x 614.4 Mbit/s)
3	2457.6 Mbit/s (4 x 614.4 Mbit/s)
4	3072.0 Mbit/s (5 x 614.4 Mbit/s)
5	4915.2 Mbit/s (8 x 614.4 Mbit/s)
6	6144.0 Mbit/s (10 x 614.4 Mbit/s)
7	9830.4 Mbit/s (16 x 614.4 Mbit/s)

To avoid the excessive fronthaul rate, SCM has recently been studied, where multiple wireless radio signals are multiplexed at different intermediate frequencies (IFs) and transmitted by a single wavelength [52], [53]. Frequency conversion between IFs and RFs are implemented in the RRH air interface. SCM offers advantages such as efficient

wavelength utilization and reduced requirements on PDs, modulators, and microwave devices at RRHs. Cost comparison of SCM RoF link and digital link to transmit four IF signals has been given, and experimental verification of only one IF carrier has been shown in [52]. Simulation results on the transmission of 35×20MHz 16-QAM-OFDM signals have been included in [53]. Additionally, polarization multiplexing (Pol-Mux) is used for a 2×2 MIMO transmission with five 10-MHz CCs [54]. However, system design and experimental evaluation of a MFH that fully satisfies aforementioned 4^{+}G requirements have not been reported. Moreover, RF processing such as frequency downconversion and upconversion in an SCM MFH has not been evaluated. In Chapter 4, the use of DWDM-SCM-PON for high-capacity MFH is systematically investigated. Due to high spectral efficiency of the proposed approach, the total occupied bandwidth can be less than 2 GHz, with a guard band between adjacent subcarriers of tens of MHz. Compared to existing solutions, it significantly reduces the requirements on both the number of wavelengths per cell site and the optical bandwidth of the optical transceivers, and thus greatly saves the cost for future high-density small-cell deployment.

In general, the UL is less restrictive than the DL. In most cases, the user equipment (UE) will transmit upstream signal to the cell site with less layers of MIMO and fewer CCs due to its limited battery life. As a result, the UL in the fronthaul requires less bandwidth than the DL. This opens opportunities to share the wavelength resource for an even better spectrum utilization. For example, instead of consuming one upstream DWDM wavelength channel per RRH, a groups of RRHs can share one wavelength by taking different IFs in a way similar to the SCM in the DL. However, UL signals are optically aggregated in the remote node (RN) rather than electrically combined. The reception of signals being optical

aggregated with small spacing is yet to be investigated. In this dissertation, two novel schemes for high spectrally-efficient and low-complexity upstream transmissions are introduced. The first method adopts SCM technique for the UL as well, where a group of RRHs has the same central wavelength but different IFs. Given that such UL signals are optically coupled in the RN, direct detection cannot be used since the combined central carrier loses coherency with the subcarriers. Coherent reception is thus needed [55], [56]. Since the symbol rate of current LTE signal is 15 ksps, much smaller than laser linewidth, conventional pilot subcarriers that are across OFDM spectrum cannot be used, a novel external RF pilot tone is thus proposed to be paired with UL signal from each RRH for frequency offset estimation and phase noise recovery. This scheme enables low-cost RRH transceivers with small bandwidth of $\leq$ 2 GHz, as well as significantly small channel spacing. The second proposed MFH UL architecture is an UDWDM over DWDM-PON with intensity modulation and novel phase-noise-insensitive heterodyne detection. By modulating the real-valued baseband OOK or OFDM signal in RRHs, the mobile data can be heterodyne detected in the CO, selected by electrical filters, and retrieved by off-the-shelf envelope detectors (EDs) without any DSP compensation for the laser phase noise. Compared with the traditional coherent UDWDM-PON, the proposed scheme reaches a significant milestone by attaining 1-GHz wavelength grid, while saving the cost of narrow linewidth lasers or complex DSP compensation in the MFH, and achieving considerably high receiver sensitivity.

1.3 Outline

The rest of the dissertation is organized as follows. In Chapter 2, two RoF architectures for future broadband optical-wireless access network – all-band RoF and band-mapped 60-

GHz RoF – are introduced with a focus on the integration of legacy wireless services and multi-gigabit mm-wave applications. In Chapter 3, a DWDM-OFDMA-based optical MBH with cost-effective IMDD links is developed along with a low-complexity and low-latency clock distribution and recovery scheme. A coherent UDWDM-OFDMA-based MBH is also presented with a novel clock distribution and DSP-free recovery scheme. In Chapter 4, high-capacity SCM-based MFH, which significantly reduces the requirements on both the number of wavelengths per cell site and the optical bandwidth of the optical transceivers, is systematically investigated. Moreover, tailored for the UL, two upstream schemes are introduced to maintain low complexity, and more importantly, to achieve high spectral efficiency by wavelength sharing. Chapter 5 provides the conclusions of this dissertation along with potential future research directions.

CHAPTER 2

MULTI-BAND MULTI-SERVICE ROF SYSTEMS

2.1 Introduction

Wireless link speeds are expected to grow towards gigabit/second and beyond. These already can be seen in wireless standards using microwave band, such as 802.11ac [57] and LTE-A [6]. To accommodate sharp data rate increase, deployment of the mm-wave spectrum range (30-300 GHz), especially the huge 7-GHz license-free spectrum located in 60 GHz has been explored. The 60-GHz band is also suitable for small cells due to the high attenuation from free-space path loss (88dB for 10m) and atmospheric absorption (about 15dB/km), which can minimize co-channel interference in small cell systems. It is essential that the access network should support a wide range of data rates, formats, protocols, and requirements. The consumers will benefit from a universal user interface that provides wireless access anywhere at anytime with minimal delay and data processing. RoF is an attractive technology for such multi-service broadband access networks. By allocating and controlling multiple wireless services in the CO, RoF systems deliver ready-to-use analog signals to RAUs or BSs with no differentiation in protocols or interfaces, and thus greatly reduce the cell site complexity and cost. In particular, since mm-wave signals can be generated optically in the CO by several photonic techniques, RAUs are able to receive such services with simply PDs and electrical amplifier. This cost-effective solution is undoubtedly beneficial for large-scale deployment. Besides analog RoF systems, digitized RoF systems, in the light of recent open BS specifications such as the CPRI [48] and the

Open Base Station Architecture Initiative (OBSAI) [58], also attract research interests for their interoperability among different vendors and flexible product differentiation. However, the digital RoF links are at least an order of magnitude more expensive than analog RoF links, as a result of the high line rates required for wideband radio channels [52]. Moreover, the digitization of mm-wave signals is impractical. This chapter, with an emphasis on the uniformity of the RoF platform that accommodates both legacy wireless services and advanced mm-wave services, proposes two practical and efficient schemes - analog all-band RoF and band-mapped 60-GHz RoF - to cover distinct application scenarios. In the all-band RoF access architecture, lower RF signals and 60-GHz signal are transmitted at their original carrier frequencies, guaranteeing backward compatibility and wide coverage. On the other hand, the band-mapped mm-wave RoF scheme, fully utilizing the wide 7-GHz bandwidth at 60 GHz, delivers multiple converged high-speed services only through 60-GHz wireless link, which is especially suited to in-building broadband wireless access. Detailed system architectures for the all-band and band-mapped RoF access networks are discussed first from the topological to the component level perspective, with a focus on the technical challenges. The experimental verification of an all-band RoF system featuring relaxed component requirement is introduced, followed by a real-time multi-service demonstration in the proposed band-mapped 60-GHz RoF system.

2.2 All-Band and Band-Mapped Mm-Wave RoF System Overview

Figure 9 illustrates the two RoF architectures for next-generation multi-service broadband wireless access networks. These two schemes deliver both multi-gigabit mm-wave wireless services and legacy BWA services in their own strength and applicable region, yet conform to one key design rule – unified optical-wireless interface is shared.

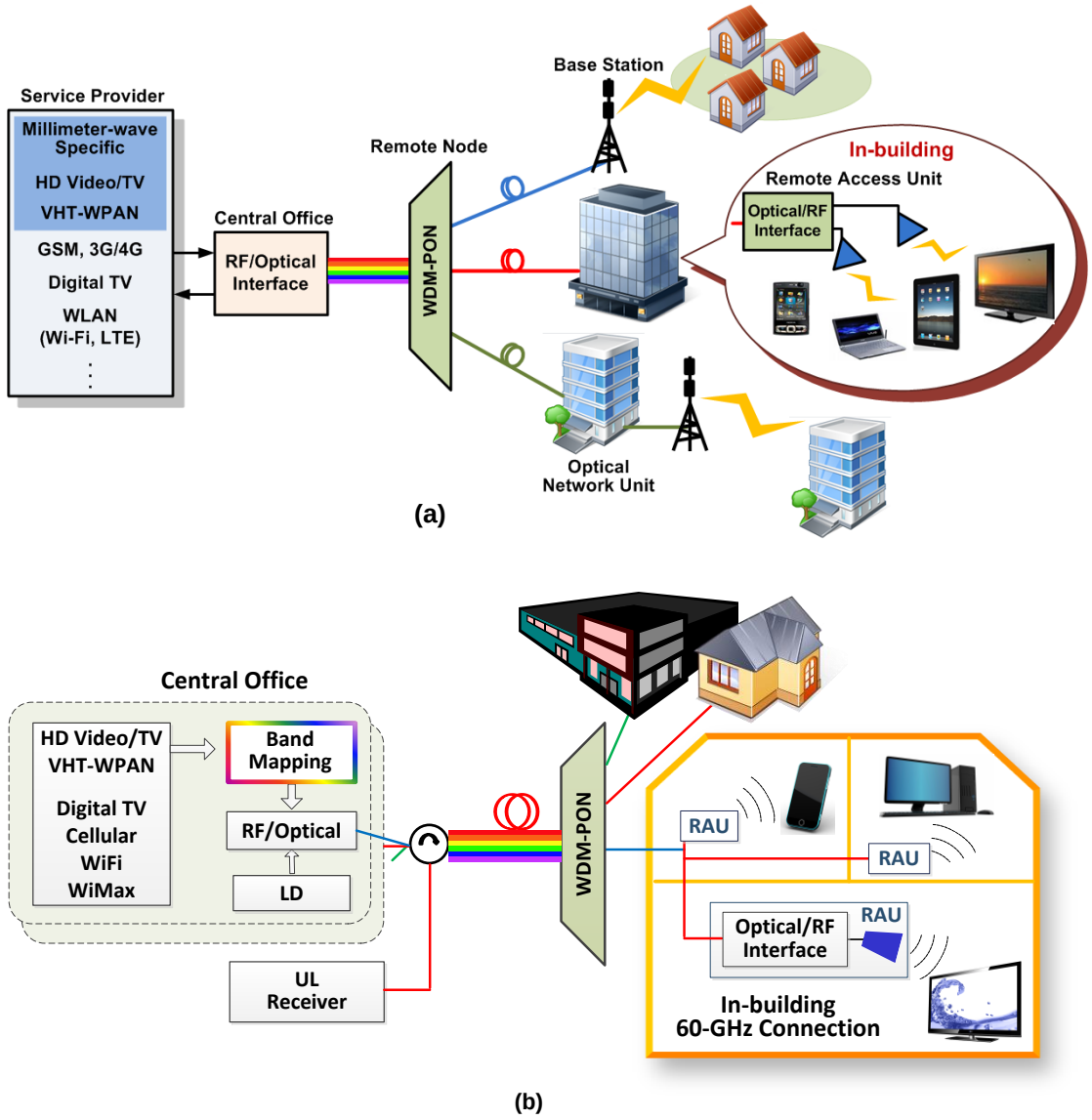

Figure 9. System architectures of (a) all-band RoF and (b) band-mapped 60-GHz RoF for unified multi-service optical-wireless access networks.

All-band RoF refers to a system that maintains each service at its original carrier frequency before E/O conversion in CO (except for mm-wave services) and after O/E conversion in RAUs or BSs. It is a promising architecture for fiber-connected massively distributed antennas in HetNets. However, limited by the modulation bandwidth of the

laser and modulator (40 GHz commercially available), signals with carrier frequencies higher than 40 GHz require special optical mm-wave upconversion techniques for downstream, including nonlinear effects, external modulation, and remote heterodyning [33]. As a result, the key technical innovation of the proposed all-band RoF system lies in the design of simple and efficient CO and RAU to simultaneously integrate lower RF wireless services and mm-wave channels. Wavelength reuse methods have been proposed for the cost-effective mm-wave RoF upstream transmission [29], [31], [32]. However, in most cases, they require complicated optical filtering, large spectrum occupation, and fixed data formats. Laser source in RAU is preferred in some situations for better flexibility and integration [33].

The all-band RoF access network architecture is shown in Figure 9(a). As a straightforward way to carry multiple wireless services simultaneously, the all-band RoF system directly adds electrical signals together (mm-wave signals may differ) and modulates them onto the lightwave through an RF-to-optical interface in the CO. Different services, naturally separated by frequencies as shown in Figure 10(a), are grouped and multiplexed in the WDM-PON. Signals at a single wavelength are demultiplexed and retrieved by a simple optical-to-RF interface at their own carrier frequencies, and finally transmitted by designated antennas to targeted mobile devices. The same infrastructure can also be shared by mobile backhaul with a much simplified base station design. Meanwhile, W-band (75-110 GHz) and beyond high-speed wireless communications that replace fiber-optic links in difficult-to-reach terrains or fiber cut emergencies can greatly benefit from the RoF architecture as well.

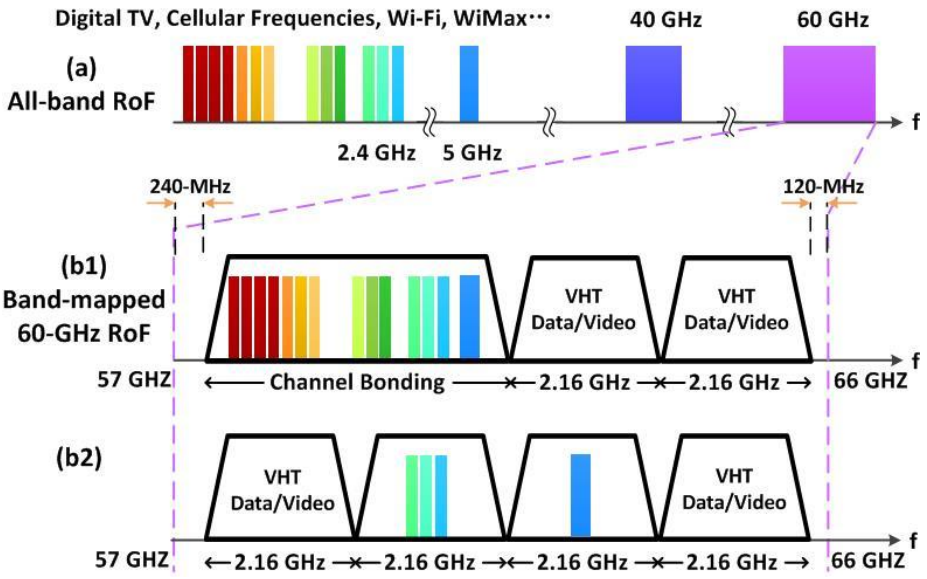

Figure 10. Spectrum allocations in (a) all-band RoF and (b) band-mapped 60-GHz RoF.

All-band RoF is able to cover wireless services from few GHz to more than 100 GHz, and transmission coverage from few meters to kilometers. However, in most cases, wireless access is done in indoor environment, such as in the office, home, convention center, and stadium. To further exploit this application scenario, Figure 9(b) illustrates a fully-converged 60-GHz RoF network based on the band-mapping concept. Existing wireless services and multi-gigabit mm-wave services can be first mapped compactly to four sub-bands (e.g., from 0.24 GHz to 8.88 GHz), and optically upconverted to 60-GHz sub-bands (e.g., from 57.24 GHz to 65.88 GHz) according to the ECMA 387 [14], as shown in Figure 10(b). Therefore, various services are delivered with the same 60-GHz RoF components, introducing little or no system-level complexity. Distinct from all-band RoF system, only one pair of electrical amplifiers and antennas at the 60-GHz band are needed, which greatly reduces the power consumption and component complexity, yet keeps the backward compatibility. By integrating wireless services from different frequency bands

into the wide unlicensed 60-GHz band, better usage of available spectrum is thus achieved. Furthermore, the spectrum allocation can be flexible upon request from mobile users and adjustment from CO as shown in Figure 10(b1) and (b2). For example, the 5.8-GHz WiMAX signal can be mapped to the first two sub-bands in a highly integrated allocation (Figure 10(b1)), or directly fit in the third sub-band without further adjustment (Figure 10(b2)). In addition to frequency distribution, power allocation among the signals also requires careful investigation. For example, an OFDM signal has smaller dynamic range due to high peak-to-average power ratio (PAPR) and subcarrier intermodulation, so does certain analog signal which is sensitive to nonlinearities and noise. Therefore, an optimal electrical power distribution [59] can be necessary in both all-band and band-mapped RoF system by setting desired performance for each service. Homodyne downconversion is realized in most off-the-shelf wireless receivers, with a tunable electrical local oscillator for different services. For certain mapping schemes, for example, the case shown in Figure 10(b2), it is preferable to firstly downconvert the mm-wave signal to the original four sub-bands in the heterodyne downconversion. ED and self-homodyne receiver are also alternatives for amplitude modulated mm-wave signals [33].

In summary, while the all-band RoF access network supports services from microwave BWA to W-band signals for both indoor and large-area links through one shared infrastructure, the band-mapped RoF serves as a highly practical and efficient future in-building optical-wireless access architecture, with multiple services simultaneously delivered under a unified optical and wireless 60-GHz interface.

2.3 Wi-Fi, WiMAX, and 60-GHz Mm-Wave in an All-Band DWDM-RoF-PON

As described previously, the main challenge of the all-band RoF architecture design is the integration of lower RF signals and 60-GHz signals. In the previous work of the simultaneous generation and transmission of 2.4-GHz (Wi-Fi), 5.8-GHz (WiMAX), and 60-GHz signals in the RoF system [29], sophisticated combination of optical IL were used in both intelligent gateway router and BS, which are not practical for industrial deployment. Furthermore, this setup occupied 120-GHz spectrum and could hardly be integrated in the spectrally-efficient DWDM-PON. In order to eliminate complicated filtering components and high-bandwidth modulators, and greatly increase the optical spectral efficiency, a novel all-band DWDM-RoF-PON system is proposed, where the Wi-Fi and WiMAX services are delivered using SCM technology and the 60-GHz mm-wave signal is achieved by dual-wavelength heterodyne beating method.

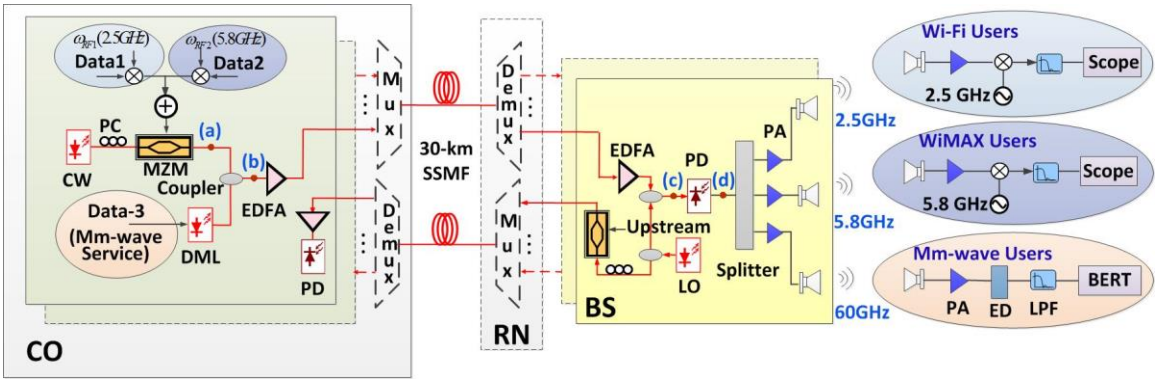

Figure 11. Experimental setup of the all-band DWDM-RoF-PON system delivering legacy Wi-Fi, WiMAX, and advanced 60-GHz services.

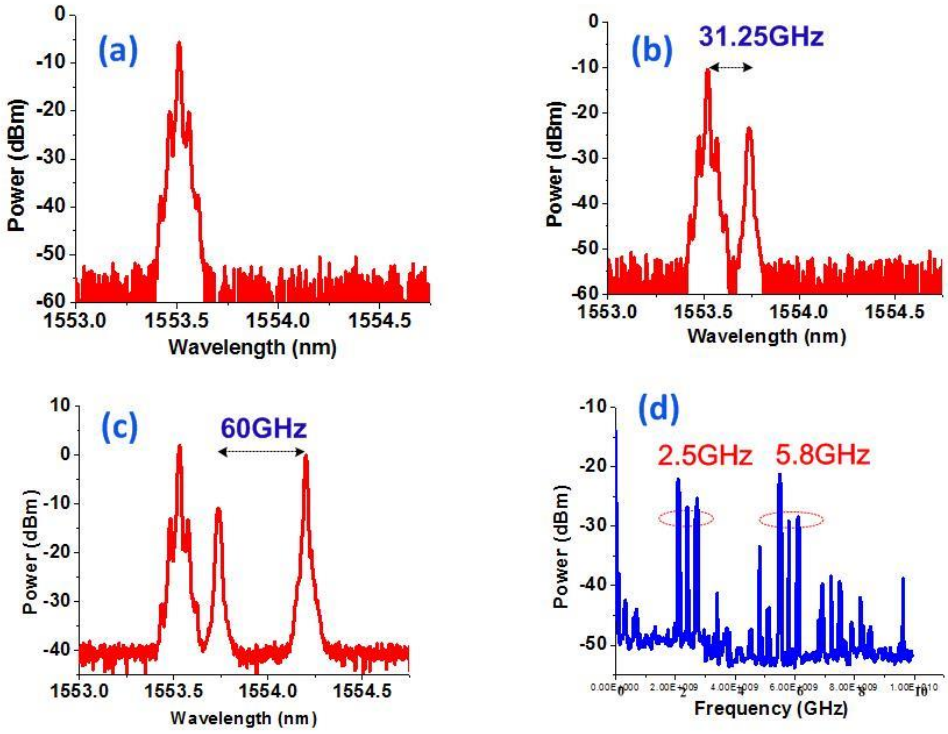

Figure 12. (a)-(c) Optical spectra measured at locations from a to c in Figure 11. (d) Electrical spectrum for the Wi-Fi and WiMAX signals after the PD.

Figure 11 illustrates the experimental setup of the proposed architecture. In the CO, a CW light (10-MHz linewidth) at 1553.50 nm is fed into a MZM. Data1 and Data2, generated by an arbitrary waveform generator (AWG) at 2.5-GSa/s sampling rate, are 16-QAM-OFDM data with a central frequency at 0.3 GHz and a bit rate of 400 Mb/s. Data1 and Data2 are mixed with 2.5-GHz and 5.8-GHz IF clocks to emulate Wi-Fi and WiMAX signals, respectively, and combined to drive the MZM with a modulation index of 0.15. An optical multiband SCM signal is obtained at the output of the MZM, whose optical spectrum is shown in Figure 12(a). A DML (10-MHz linewidth) at 1553.75 nm is driven by Data3, a 1-Gb/s pseudo random binary sequence (PRBS) signal generated by a pattern generator, with an optical modulation index ~1 for the mm-wave service. The optical

outputs are coupled (Figure 12(b)) and amplified by an EDFA. The two wavelengths with 31.25-GHz spacing can be multiplexed with other groups of wavelengths through an arrayed waveguide grating (AWG) with 50-GHz channel spacing. After the 30-km standard single mode fiber (SSMF) transmission, another AWG in the RN can demultiplex each channel to the designated BS. In the experiment, multiplexer (MUX) and demultiplexer (DEMUX) are not implemented due to device limitation. At the BS, the downstream signal is pre-amplified, coupled with an optical local oscillator (LO) (20-MHz linewidth, 3-dBm optical output power) at 1554.23 nm (Figure 12(c)), and sent to the PD, where self-beating and heterodyne mixing are realized. Specifically, the 2.5-GHz and 5.8-GHz signals can be generated after self-beating of the multi-band SCM signal, while the 60-GHz signal can be achieved by heterodyne mixing of the optical OOK signal and LO light. The beating between the first wavelength and LO exceeds the bandwidth of the PD, and thus introduces no interference to the mm-wave signal. Note that the spacing between the two lasers in the CO can be further reduced to fit in a 25-GHz spaced DWDM system, or even 12.5-GHz UDWDM-PON. The only concern is to choose proper PD and 60-GHz amplifier and antenna that can filter out unwanted beating terms from the first wavelength and the LO. The electrical spectrum after the PD is shown in Figure 12(d), consisting of 2.5-GHz and 5.8-GHz components. Due to bandwidth limitation of the electrical spectrum analyzer (ESA), the spectrum at 60 GHz is not provided. Each of the three services is amplified and transmitted over 3-ft wireless link at its own band. The received Wi-Fi-like and WiMAX-like signals are downconverted and sampled by a real-time oscilloscope at 25 GSa/s. The 60-GHz signal is downconverted by an ED and sent to a bit error rate tester (BERT). For the upstream, same LO light is split as the upstream optical carrier and

modulated by a 1-Gb/s PRBS data. Upstream channels can be transmitted with another MUX and DEMUX as shown in Figure 11, with the same channel spacing but shifted passbands compared to the pair for downstream.

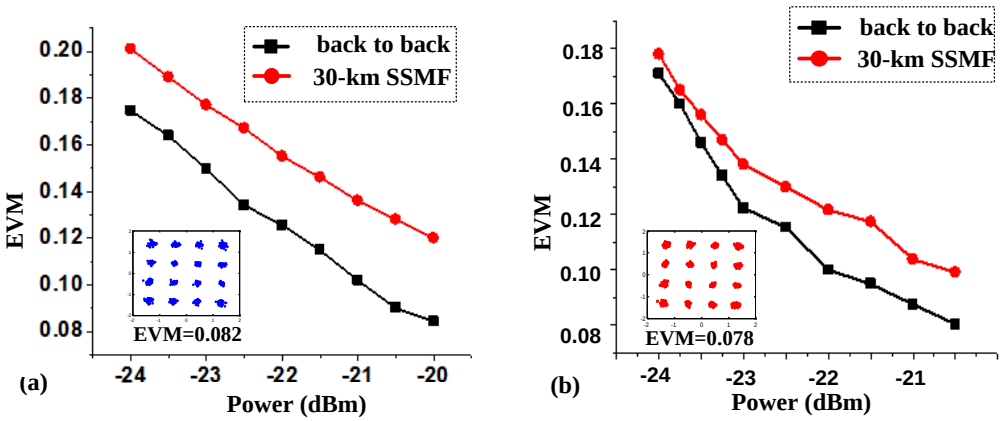

Figure 13. EVM of the (a) 2.5-GHz Wi-Fi-like signal with a constellation at EVM = 0.082, and (b) 5.8-GHz WiMAX-like signal with a constellation at EVM = 0.078.

The error vector magnitude (EVM) performances of the 2.5-GHz Wi-Fi-like signal is shown in Figure 13(a) along with clear constellation plots. A 1.8-dB power penalty is observed after 30-km SSMF transmission (received optical power measured before the EDFA at the BS) due to the fiber chromatic dispersion (CD) and intermodulation from other signals. The EVM of the 5.8-GHz WiMAX-like signal is shown in Figure 13(b). The receiver sensitivity to achieve an EVM of 0.125 after 30-km fiber transmission is -20.5 dBm for the 2.5-GHz signal and -22 dBm for the 5.8-GHz signal. The performance of the 2.5-GHz signal is slightly worse than that of the 5.8-GHz signal due to the different antenna responds and the interference from other commercial 2.4-GHz band Wi-Fi services. It can

be observed from Figure 12(d) that the noise floor around 2.5 GHz is higher than the one near 5.8 GHz.

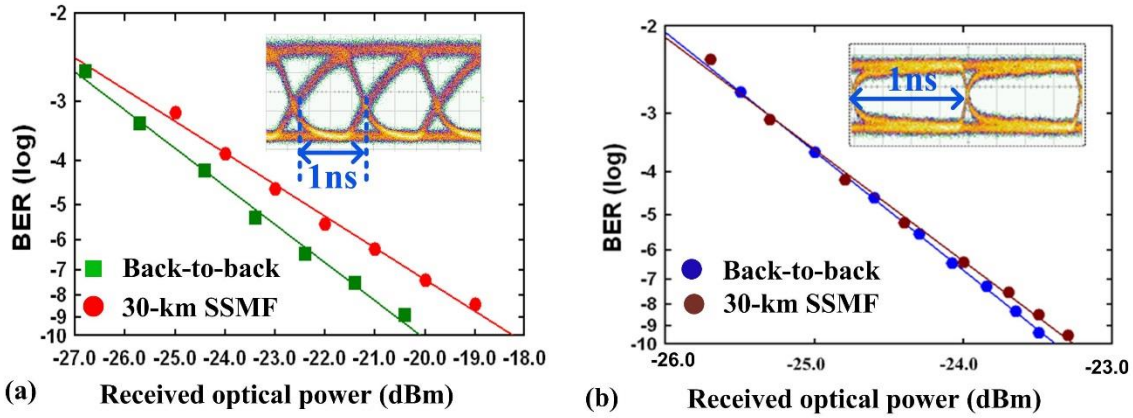

Figure 14. BER performances and eye diagrams for the (a) downconverted downstream mm-wave signal and (b) the upstream signal.

The BER performance and eye diagram of the downconverted 60-GHz signal for 5-ft wireless transmission case are illustrated in Figure 14(a). Power penalty of 1.5 dB is observed after 30-km SSMF transmission compared with back-to-back (BTB) case at BER = 10^{-9}, again due to the CD and nonlinearity from the intermodulation. For the same BER level, receiver sensitivity of -18.8 dBm with 30-km fiber propagation is achieved. As for the UL, the BER performance and clear electrical eye diagram of the upstream signal are shown in Figure 14(b). Small power penalty is induced after the 30-km SSMF transmission, since only single channel is transmitted over the fiber. The receiver sensitivity for the UL is about -23.4 dBm.

2.4 Real-Time TV, Wi-Fi, and Gigabit Data in a Band-Mapped 60-GHz RoF System

Based on the band-mapping concept introduced previously, legacy wireless services can be frequency-shifted to the 60-GHz sub-bands and delivered simultaneously with the gigabit mm-wave services such as HDTV in Wireless HD standard [12]. This new multi-service delivery using the unified wireless interface is a promising candidate for next-generation indoor service bundle models. To verify the feasibility of the band-mapping scheme, an experimental demonstration is implemented with three services representing distinct signal types, i.e., broadcast TV signal in analog form, Wi-Fi as a highly modulated vector signal and digital baseband data for 60-GHz very high data rate application. Note that the TV and Wi-Fi signal receptions are both non-offline and through commercially available products.

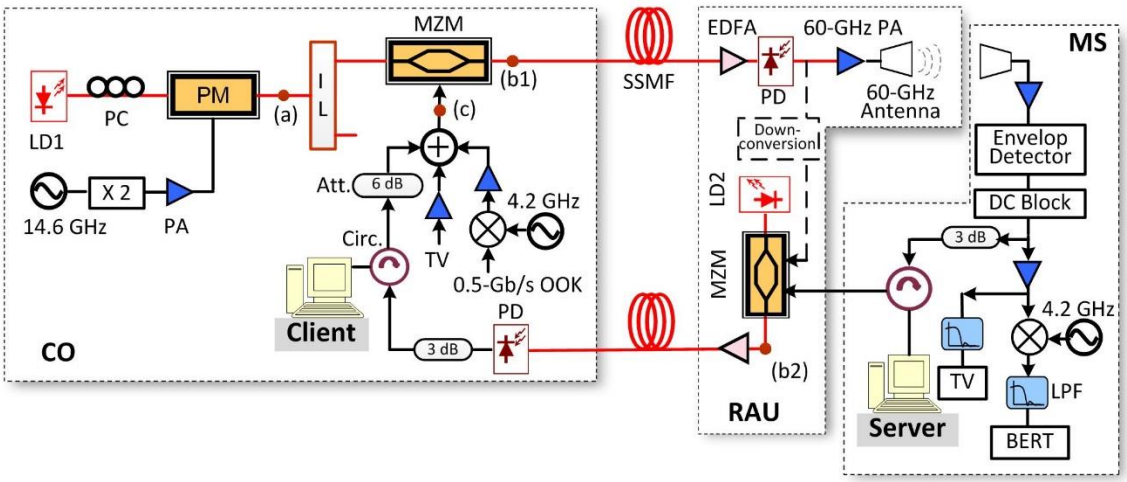

Figure 15. Experimental setup of the band-mapped 60-GHz RoF system for TV, Wi-Fi, and OOK data.

Figure 15 shows the experimental setup of the real-time band-mapped 60-GHz RoF

demonstration with fully converged services inside 60-GHz sub-bands (within the 57-64 GHz license-free spectrum in North America). At the CO, a PM is driven by a 29.2-GHz sinusoidal wave to generate multiple optical sub-carriers, shown in Figure 16(a). A 33/66 GHz IL is used to separate the 1st-order sidebands from other sub-carriers. An HWVG1 Wireless-G Adapter in the client computer is used to transmit and receive 802.11g Wi-Fi signal of 22-MHz channel width at 2.4 GHz. The transmit power is 17 dBm ± 2 dB, comparatively larger than the other two services. Therefore, it requires attenuators before it is combined with other signals. The TV signal is directly obtained from the wall outlet and then connected to the setup. A 0.5-GHz OOK is firstly upconverted to an IF at 4.2 GHz, and combined with Wi-Fi and TV signals (Vpp = 0.8V, 0.8V, and 1.2V, respectively). The electrical spectrum of the combined signal is shown in Figure 16(c). The aggregated signal drives the MZM biased at the quadrature point. The downstream spectrum is shown as the solid black line in Figure 16(b).

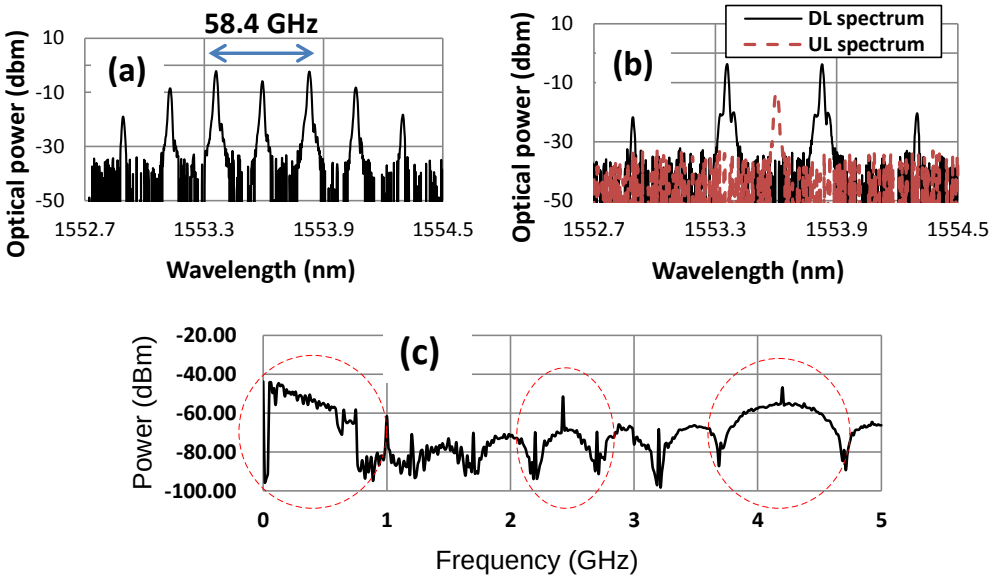

Figure 16. (a) and (b) Optical spectra measured at locations a, b1, and b2 in Figure 15. (c) Electrical spectrum measured at location c in Figure 15.

After fiber propagation, the lightwave is pre-amplified by an EDFA in the RAU and detected by a 60-GHz bandwidth PD to optically upconvert the three services to 60-GHz sub-bands. A pair of 60-GHz horn antenna (15dBi gain) with 3-ft separation is used for wireless propagation. At the mobile station (MS), an ED downconverts the received 60-GHz band-mapped signal to their original carrier frequencies. The DL Wi-Fi signal is received by an EZ Connect G Wireless PCI Adapter (SMCWPCI-G2) in the server computer. Since Wi-Fi connections need to be established with round-trip communication, bi-directional Wi-Fi signal transmission is additionally implemented in the optical RoF system in this experiment. A circulator and 3-dB attenuator are used to isolate the UL and DL signals since the generated UL Wi-Fi has much larger power (18 dBm maximum) than the DL Wi-Fi signal. Ideally, the upstream wireless signals should also be mapped to 60-GHz sub-bands and transmitted back to the RAU. They can be downconverted by an ED or a mixer before the E/O conversion. However, the 60-GHz UL, indicated by the dashed flow in Figure 15, is not implemented here on account of insufficient 60-GHz power amplifiers (PA) and mixers. Instead, the 2.4-GHz Wi-Fi UL is directly modulated without mm-wave conversion and wireless propagation. Note that the central wavelength of the DL can be reused for upstream transmission in avoidance of any laser source for a simpler RAU. Another laser diode (LD) is deployed for Wi-Fi UL, limited by the available devices, as illustrated in the red dotted line in Figure 16(b). The DL 0.5-Gb/s OOK signal is downconverted and filtered by a 1-GHz low-pass filter (LPF) before being sent to a BERT. Meanwhile, after a 1-GHz LPF, the TV signal is displayed by a HDTV.

Wi-Fi signal throughput is tested by Iperf [60] in three cases: BTB, DL and UL 0.5-km SSMF, and DL 5-km SSMF, UL BTB, as illustrated in Figure 17. The fiber length is

limited by the $ACK_{timeout}$ defined in Wi-Fi media access control (MAC) layer [61]. The one-way delay is 20 μs, corresponding to an approximate 6-km SSMF propagation. It is possible to adjust the $ACK_{timeout}$ value to allow longer waiting time, but the throughput will drop as the idle period increases. Reductions of throughput occur around -21 dBm. Negligible power penalty is induced by the 0.5-km SSMF, and about 1-dB power penalty after 5-km fiber transmission is observed. The penalty is primarily due to the effect of the extra propagation delay as described in [61] and partially due to the cross-modulation among the three signals [62]. As shown in Figure 18, the throughput vs. time is also measured with and without RoF system to further study the stability over time. The Wi-Fi throughputs in the RoF system with different setups are measured with a fixed received optical power at -14 dBm. In addition, a result obtained via conventional wireless propagation using a pair of Wi-Fi antennas is included in Figure 18 (marked in blue dots) for comparison. The average Wi-Fi throughput in the three-band 60-GHz RoF system without fiber transmission is 19.3 Mb/s, slightly higher than 19.1 Mb/s in the conventional Wi-Fi wireless transmission. The main reason is that the latter encounters interference from other Wi-Fi radio signals and wireless propagation impairments. Moreover, real-time Internet access is realized, where the client computer in Figure 15 is set as a hotpot and the server computer is thus connected to the Internet. YouTube HD video streaming is demonstrated in Figure 20(a).

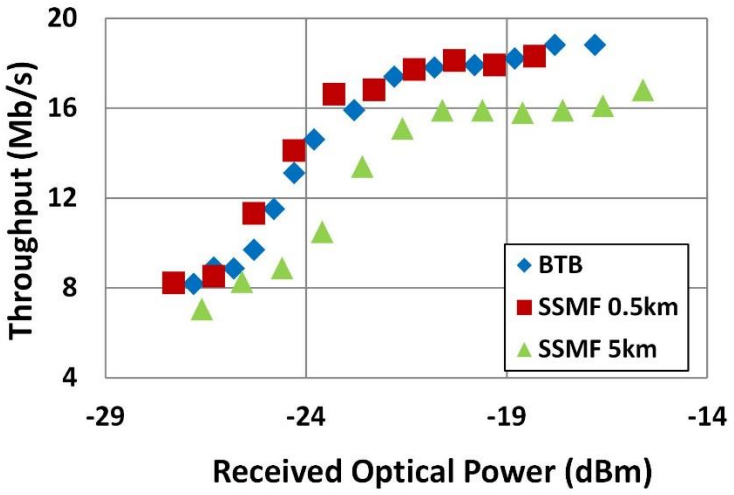

Figure 17. Wi-Fi throughput vs. received optical power for different fiber lengths.

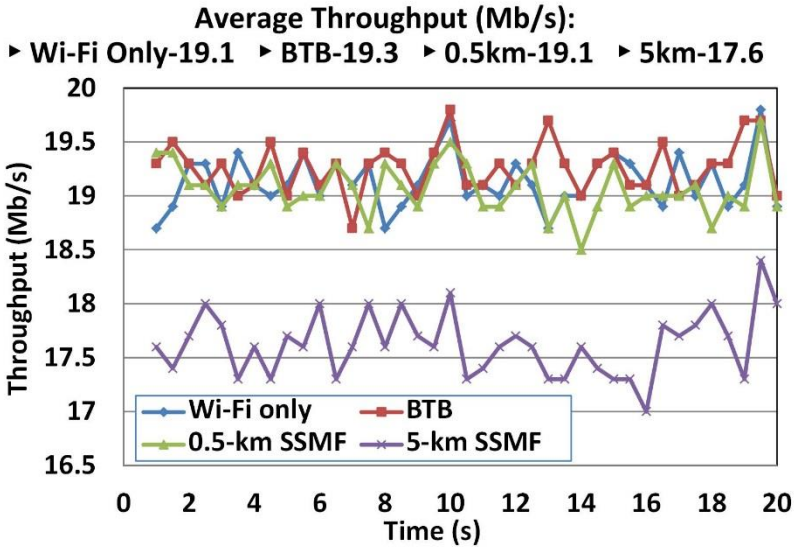

Figure 18. Wi-Fi throughput in 20-sec interval for conventional Wi-Fi wireless link and multi-service 60-GHz RoF system.

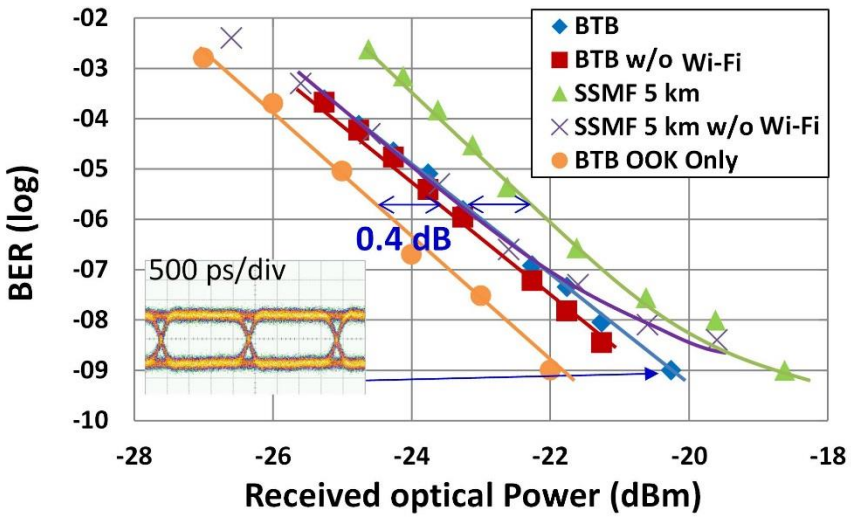

Figure 19. BER vs. received optical power of the OOK data, with and without Wi-Fi.

Figure 19 illustrates the BER performance of the 0.5-Gb/s OOK data. The power penalty induced from Wi-Fi to OOK signal is negligible in the BTB case, as seen from the blue diamonds and red squares. The penalty is about 0.4 dB in the 5-km fiber transmission case, indicated by the green triangles and purple crosses. As the fiber length increase, Wi-Fi performance drops (Figure 17) due to longer waiting time as well as fiber chromatic dispersion. As a result, Wi-Fi adapters will automatically increase the output power, which will introduce more cross-modulation to other channels. A power penalty due to TV signal is about 0.4 dB, observed between the orange-dot line and the red-square line.

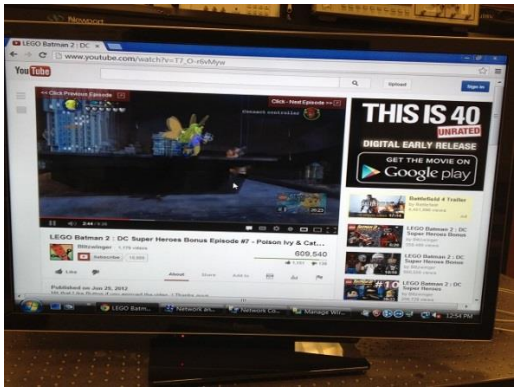

(a)

(b)

(c)

Figure 20. (a) Internet access via band-mapped Wi-Fi in 60-GHz RoF. (b) TV signal alone in 60-GHz RoF. (c) TV signal in the multi-service 60-GHz RoF.

Figure 20(b) shows a clear screenshot of the TV signal received from the 60-GHz RoF system, without Wi-Fi and OOK channels, while Figure 20(c) shows the noisier TV signal from the 60-GHz RoF system with the presence of other channels. Since TV signal is analog, any interference or distortion imposed on it will be observable. In order to avoid the intrinsic cross-modulation from the nonlinear transfer function of the optical modulator in the multi-band 60-GHz RoF system, separated modulators can be used for services that are highly susceptible to distortion such as analog TV signals.

2.5 Summary

In this chapter, two optical-wireless access architectures based on RoF technology that provide simultaneous legacy wireless services and high-speed mm-wave services have been proposed. With shared optical infrastructure and centralized management, all-band RoF system is capable of covering a wide range of wireless services carried by frequencies ranging from a few GHz to more than 100 GHz, at various transmission distances, and in both indoor and outdoor environments. Band-mapped RoF system, on the other hand, delivers multiple services at 60-GHz band with one unified optical and wireless interface and features less power consumption and very high spectral efficiency. Both are favorable for high-density small cell systems due to the newly proposed BSs with greatly reduced complexity. With remote heterodyning technique, it is possible to integrate RoF systems into DWDM-PON, or even UDWDM-PON to reach massive amount of users. The delivery of independent Wi-Fi, WiMAX and 60-GHz mm-wave signals over 30-km SSMF in the all-band RoF system has been experimentally evaluated. Finally, a real-time demonstration of converged TV, Wi-Fi and OOK data in the band-mapped 60-GHz RoF system has been reported. Fiber length limitation, comparison with conventional Wi-Fi link, and cross-modulation among channels have been investigated. By combining low cost, high speed, and high flexibility, the multi-band multi-service RoF access architectures appear promising for future broadband wireless heterogeneous networks.

CHAPTER 3

OFDMA-BASED MOBILE BACKHAUL AND LOW-LATENCY SYNCHRONOUS CLOCK DISTRIBUTION AND RECOVERY

3.1 Introduction

Boosted by emerging smart mobile devices and applications, the mobile data traffic is growing exponentially. To accommodate the targeted data rate requirements, such as 1-Gb/s requirement included in the LTE-A standard, a large number of small cells that reuses available spectrum will be needed to provide economical high-speed mobile traffic delivery. As a result, the ability to cost-efficiently support high data rates with low latency is among the essential requirements for 4^{+}G MBH systems. Optical MBH systems based on IMDD OFDMA techniques are recently studied for high-capacity optical MBH that can support hundreds of cells per fiber, each at > 100-Mb/s speed [41], [63]. However, synchronization techniques are needed in order to practically implement OFDMA-based optical MBH. In this chapter, a DWDM-OFDMA-based optical MBH architecture is proposed along with a simple and low-latency clock distribution and recovery scheme with flexible clock rates and DSP-free electrical filtering. The synchronous clock distribution is achieved jointly with high-speed OFDMA data signal transmission through a simple IMDD optical backhaul architecture that also guarantees clock time and frequency stability. Moreover, the OFDMA backhaul is further integrated with a UDWDM system which is intensively studied for the future optical access network. A novel spectrally-efficient, low-complexity

clock distribution and recovery scheme for UDWDM-OFDMA-based MBH based on optical SSB modulation and DSP-free envelope detection is also demonstrated.

3.2 Synchronous Clock Distribution and Recovery for DWDM-OFDMA-Based Optical MBH

3.2.1 Architecture and Synchronization Requirements

Figure 21 illustrates the proposed architecture of the DWDM-OFDMA-based next-generation optical MBH. The MBH can be merged to the edge of the optical metro network via metro Ethernet switches, for example. As shown in Figure 21, in the OFDMA transmitter (Tx) at the optical line terminal (OLT), the OFDMA signal is generated by assigning orthogonal subcarriers to different cell sites through DSP in digital logic such as field programmable gate array (FPGA) or application specific integrated circuit (ASIC), and then intensity-modulating the resulting electrical OFDMA signal. The aggregate OFDMA signals on multiple wavelengths, λ_i, $i = 1, 2, \ldots, N$ are optically multiplexed with tight DWDM λ-spacing, f_s. At the RN, each wavelength is distributed by a DEMUX, either to a designated general small cell area where conventional BSs are connected by optical splitters or to a centralized BBU pool location followed by the emerging MFH. At each MBH optical network unit (ONU), the received OFDMA signal is directly photodetected and digitized. The downstream information for each cell is then digitally extracted and prepared for wireless radio transmission over the air interface. In the case of MFH, the OFDMA signal is processed in the BBU pool and distributed to the connected cell sites via fronthaul links. This way, the optical access network infrastructure is able to cover large mobile user service areas by grouping high-density small cells, while efficient statistical

multiplexing of traffic between cells is achieved via OFDMA-based dynamic bandwidth allocation.

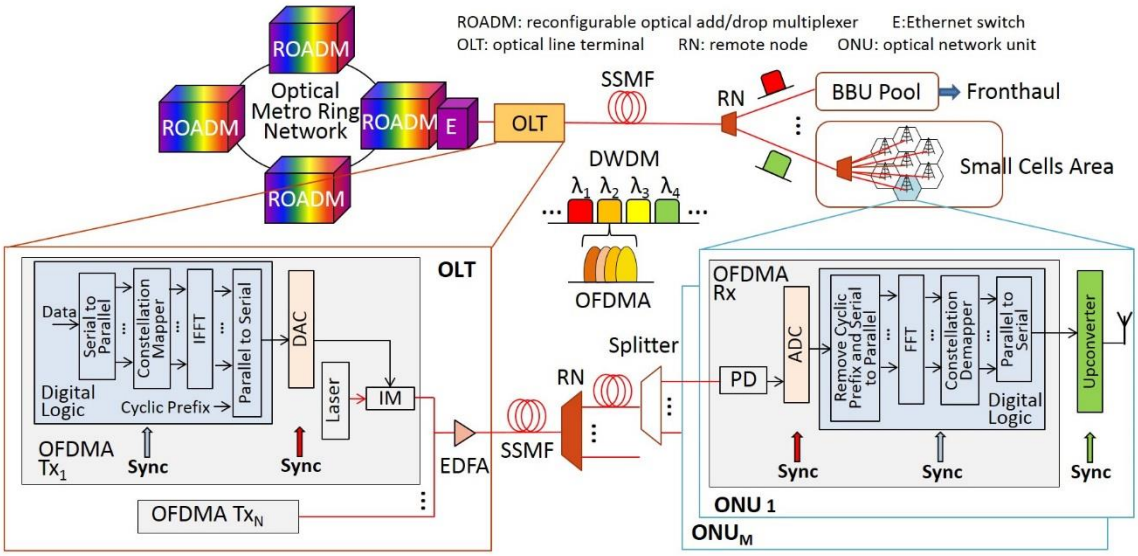

Figure 21. System architecture of DWDM-OFDMA-based MBH and synchronization requirements.

Table 2 summarizes the mobile backhaul frequency accuracy requirements in terms of parts per billion (ppb) and time-of-day accuracy requirements in microseconds for synchronization in the common air interface specifications. As wireless technology evolves to both higher data rates and higher quality-of-service, synchronization requirements must become more stringent. The frequency accuracy a MBH needs to achieve is 16 ppb, and the timing accuracy is required to be less than 1 μs, as listed in the LTE-A standard. Therefore, clock distribution and recovery for 4^{+}G MBH should both meet and preferably exceed the requirements of LTE-A shown in Table 2. Since higher frequency accuracy is required for the MBH network compared to the air interface (Table 2), the focus of this

work is on synchronous clock distribution and recovery that meets the MBH network requirements for the fiber-optic MBH transmission segment.

Table 2. Mobile backhaul synchronization requirements

Technology	Frequency Network/Air	Time
GSM, UMTS, WCDMA, LTE - FDD	16 ppb/50 ppb	None
CDMA 2000	16 ppb/50 ppb	3-10 μs
LTE - TDD	16 ppb/50 ppb	1.5 μs <3 km cell radius 5 μs >3 km cell radius
LTE-Advanced	16 ppb/50 ppb	<1 μs

Moreover, as shown in Figure 21, additional OFDMA-related synchronization functions are needed in addition to the requirements in Table 2, to support practical real-time operation of DWDM-OFDMA-based MBH systems. In terms of real-time OFDMA transmission, FPGAs and/or ASICs that perform real-time DSP functions including the fast Fourier transform (FFT) and inverse FFT (IFFT) [42], require a square wave clock input for synchronization. On the other hand, DAC/ADC at the analog electrical front end mandate sinusoidal clock inputs. Two clock signals are thus required for real-time OFDMA transmission – a square wave clock that feeds the digital logic and a high-frequency (multi-GHz) sine wave clock serving as the sampling clock reference for the DAC/ADC. Symbol-level synchronization accuracy between the square and sine is also necessary for correct OFDMA signal generation and reception. The clocks used in end-to-end OFDMA transmission should all be synchronized on the system level as well, should be recoverable without intensive DSP to minimize latency, and should support an overall clocked OFDMA system that is not prohibitively impaired by sampling clock offset (SCO) and symbol timing offset (STO). While transmitting a single clock and obtaining the second by

frequency multiplication or division of the first is feasible [43], in this chapter, a fully-parallel DSP-free clock distribution scheme is proposed, wherein a band-pass filter (BPF) and a LPF simultaneously recover sine and square wave clocks without DSP.

The proposed DWDM-OFDMA approach thus enables synchronous clock distribution without the need to involve with packet-based synchronization approaches that may require hop-by-hop hardware/protocol specificity and network engineering to manage jitter. Although the global positioning system (GPS) could also be employed at cell sites for air interface synchronization, its line-of-sight nature and security issues nonetheless urge the development of new synchronization schemes. Moreover, in the proposed approach, clocks are centrally controlled and distributed to the BS, offering attractive scalability potential and a natural compatibility with centralized SDN-based management.

A novel clock distribution and recovery scheme that fully takes advantage of the low-latency DWDM-OFDMA-based MBH architecture and satisfies (and exceeds) the above-mentioned synchronization requirements is proposed and discussed next.

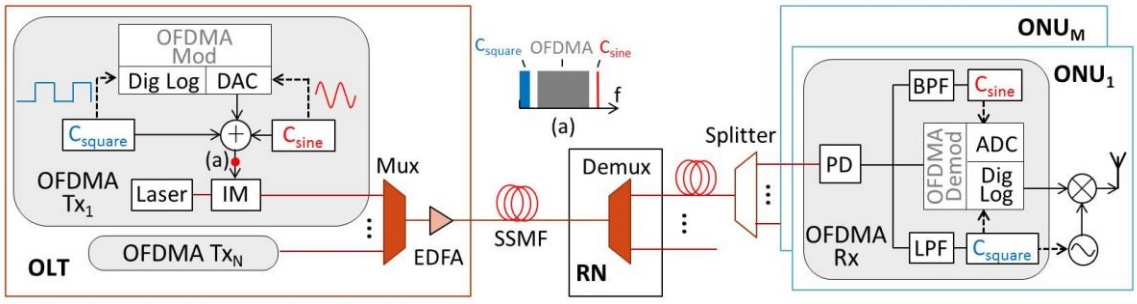

Figure 22. Schematic diagram of low-latency clock distribution and recovery principles for DWDM-OFDMA-based 4^{+}G optical MBH. (a) Electrical spectrum of the combined signal.

3.2.2 Operational Principles

As described previously, all of the square and sine clocks needed for real-time OFDMA data signal transmission are able to serve as highly accurate time and frequency reference simultaneously for BSs in DWDM-OFDMA-based optical MBH featuring scalable and efficient centralized management.

The detailed operational principle of the proposed DWDM-OFDMA-based technique for optical MBH is shown in Figure 22. As illustrated in Figure 22, the OFDMA modulator (Mod) in the OLT generates an electrical OFDMA signal using two clocks: a baseband square wave clock, C_{square}, that controls Tx-side digital logic (Dig Log) and a sine wave clock C_{sine} that controls the DAC. The two clocks are generated from a common reference clock in order to be synchronous. At the DAC output, the OFDMA signal is electrically combined with the two clock signals, and the aggregate electrical signal is applied as input to an optical IM. As shown in Figure 22(a), the OFDMA data and clock signals are separated in frequency domain with moderate guard bands. Link rate and clock rates can be thus flexibly changed without significant changes to the remote nodes, which is preferable for cost-efficiency. The combined optical data/clock signals from each OFDMA Tx are multiplexed using a DWDM multiplexer (Mux), and wavelength-demultiplexed in the RN to serve designated ONUs. At each ONU, the joint data/clock signal is directly detected by a PD and electrically split into three parts. A BPF and a LPF with matching passbands are deployed to filter out C_{sine} and C_{square}, respectively, for DSP-free clock recovery. Both clocks are thus retrieved without computational complexity or delay. The clocks are moreover time and frequency synchronized with the OFDMA data signal due to the optical locking that occurs during intensity modulation of the combined

Tx-side data/clock signal. Following Rx-side OFDMA data processing, the DS traffic is extracted and re-modulated into the target wireless format by the RF module, for which C_{square} can be multiplied using a phase locked loop (PLL) to achieve the desired carrier frequency. It is also noted that C_{sine} can likewise be divided and used as a frequency reference. Therefore, frequency and phase of the clock signals are precisely maintained after direct photodetection, guaranteeing high synchronization accuracy.

3.2.3 Experimental Setup and Results

Figure 23 shows the experimental setup of the proposed DWDM-OFDMA-based optical MBH approach featuring a flexible, low-latency synchronization scheme. A 50-MHz square wave clock, C_{square} with a 50% duty cycle is generated by a Pulse Pattern Generator using a 100Mb/s OOK signal, while C_{sine} is produced by an Analog Signal Generator at frequencies of 4 GHz or 5 GHz, denoted as C_{sine1} and C_{sine2}, respectively. A 520MHz LPF and a 3.4-9.9GHz BPF are imposed before C_{square} and C_{sine} are combined by an electrical power combiner (non-directional), in order to reduce reflections from other ports. Clocks are then electrically amplified and added with the generated OFDMA signal from a 12Gs/s AWG. The first OFDMA signal set featured 16-QAM, FFT size of 512 and consisted of two sub-bands at IFs of 1.5 GHz and 2.8 GHz, a raw data rate of 5.87 Gb/s, and is denoted as $OFDMA_1$ in Figure 23. To demonstrate system flexibility in selecting different clock and data rates, a second 7.33-Gb/s OFDMA signal with two sub-bands centered at 1.7 GHz and 3.3 GHz, denoted by $OFDMA_2$ in Figure 23, is also studied. For transmission, $OFDMA_1$ is combined with C_{square} and C_{sine1} as shown in Figure 24(a1), while $OFDMA_2$ is paired with C_{square} and C_{sine2}, as shown in Figure 24(a2). Seven distributed feedback (DFB) lasers with 25-GHz spacing are coupled and used to modulate optical IM driven by the

combined OFDMA data and clock signals. The generated DWDM channels are optically boosted using an EDFA (Figure 24(b)) before being launched over the 40-km SSMF link (Figure 24(c)). To emulate a wavelength DEMUX, a Finisar WaveShaper with 13-GHz bandwidth is used to filter the center channel (4^{th} wavelength, as per Figure 24(d)), selected because it would experience the most severe nonlinearity effects during transmission.

Two types of optical receivers, including a linear PIN photodiode + transimpedance amplifier (TIA) and an avalanche photodiode (APD) + TIA, are tested in the experiment and compared. The clock signals C_{square} and C_{sine} are retrieved after matching electrical filters, while a 40-GSa/s real-time oscilloscope is used to perform ADC, with OFDMA signal processing performed in off-line DSP. Figure 24(e1) and (e2) illustrate the two received sets of electrical OFDMA data + clock signals. Compared with Figure 24(a), it may be observed that the noise floor increases from -60 dBm to -50dBm, and that the higher frequency OFDMA sub-bands exhibit attenuation due to component frequency response limitations at higher frequencies, causing a slightly larger penalty to sub-band 2 compared to sub-band 1. In terms of potential Raman crosstalk effects on the clock signals, it is note that since Raman crosstalk is significant in the 50-100MHz frequency range, the 5GHz sinusoidal clock will not be affected by this phenomenon, while Raman effects on the 50-MHz square-wave clock could readily be managed through simple RF-domain notch filtering of any parallel WDM-OOK channels [64]. Moreover, since the parallel WDM-OFDM channels in this experiment have no signal content in the 50-100MHz frequency range, they will not induce any Raman effects on the 50-MHz clock signal.

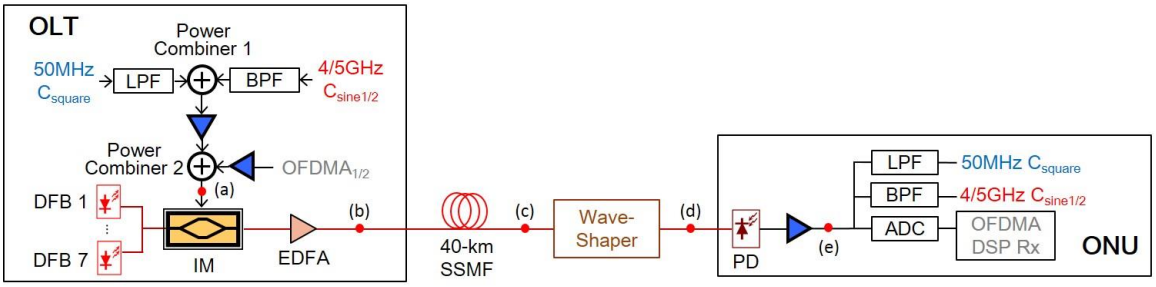

Figure 23. Experimental setup of the DWDM-OFDMA-based MBH with the proposed low-latency synchronization scheme.

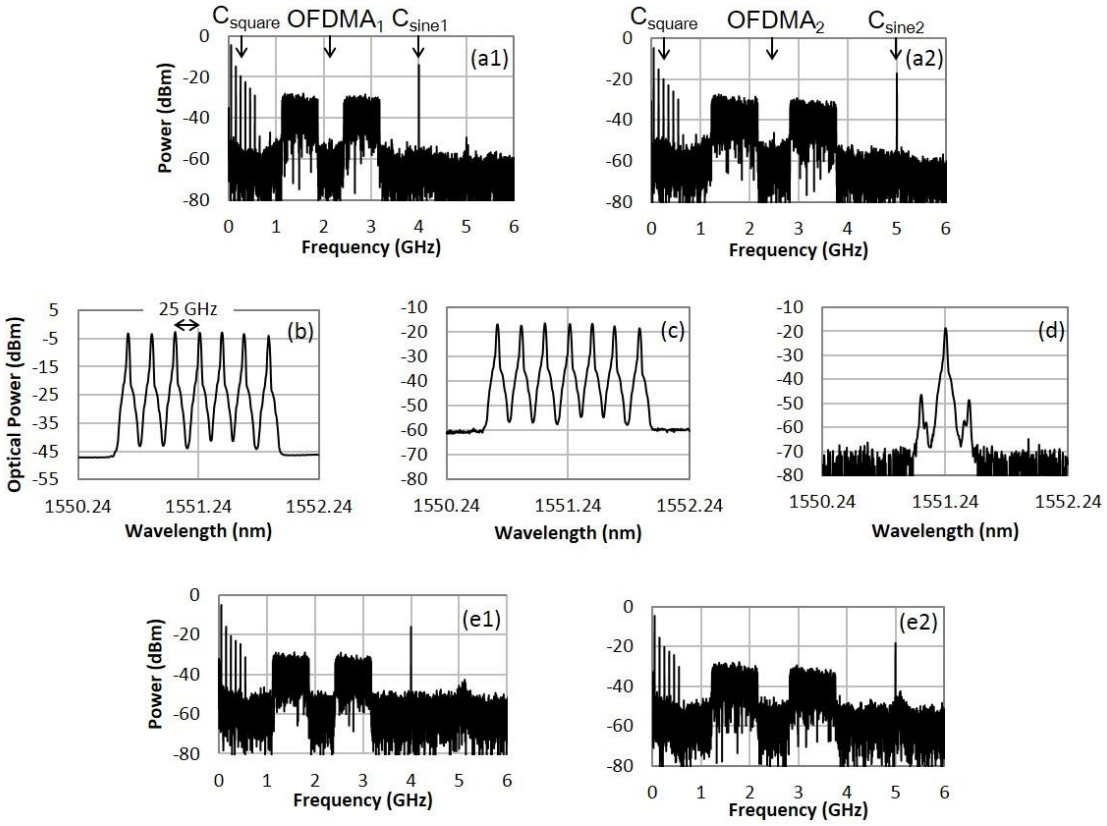

Figure 24. (a) and (e) are electrical spectra measured at point a and e in Figure 23. (b)-(d) are optical spectra at 0.02 nm resolution measured at point b to d in Figure 23.

Figure 25 plots the measured BER for the OFDMA data signals using the 10-GHz PIN+TIA PD. At BER = 3.8×10^{-3} (forward error correction (FEC) limit using 7% overhead with hard decision decoding), receiver sensitivity near -13.3 dBm using the linear PIN+TIA

PD is achieved for $OFDMA_1$, and -11.3 dBm for $OFDMA_2$. The power penalty between $OFDMA_1$ and $OFDMA_2$ signals is 2 dB at BER = 3.8×10^{-3} for both the optical BTB and 40-km SSMF cases. Clock insertion introduces a 1.3-dB power penalty, mostly due to reflection of electrical power at the OLT-side combiner and output power saturation of the ONU-side electrical power. Negligible optical BTB penalty is observed for adding 7 DWDM channels. However, after 40-km SSMF, a 1-dB received optical power penalty is noted, which can be mainly attributed to nonlinear effects in the narrowly spaced DWDM system. The experiment is repeated for the 10-GHz APD+TIA optical receiver, with BER results shown in Figure 26. The receiver sensitivity at the FEC limit is -18 dBm for $OFDMA_1$, and about -13 dBm for $OFDMA_2$. Compared with the $OFDMA_1$ BER performance using a PIN PD (Figure 25), a significant improvement is obtained using an APD (Figure 26), due to better receiver sensitivity that lowers the optical power requirements at the FEC limit, reducing nonlinearity effects and signal-signal beating interference after 40km SSMF. Due to its higher-frequency content, the $OFDMA_2$ signal requires relatively larger received power, however, resulting in BER curve saturation. This also explains the difference in the total power penalty values induced by the clocks, fiber and multiple wavelengths, which are 3.5 dB and 6 dB for $OFDMA_1$ and $OFDMA_2$ signals, respectively, as per Figure 26.

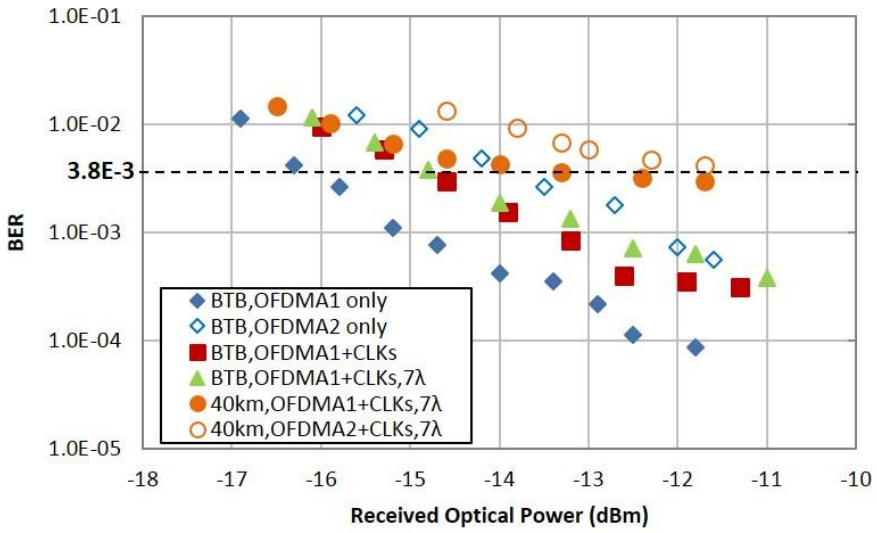

Figure 25. BER for OFDMA signals using 10-GHz linear PIN + TIA optical receiver.

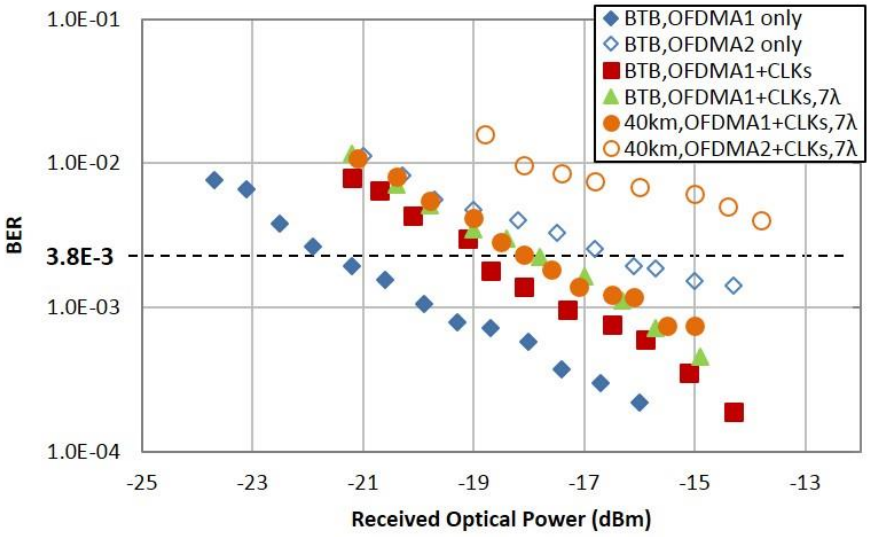

Figure 26. BER of OFDMA signals using 10-GHz APD + TIA optical receiver.

To assess square wave clock performance, the 50-MHz square wave clock recovered after the 580-MHz LPF is first sent to a BERT. Figure 27 depicts measured BER for the 50-MHz C_{square} using a 10-GHz PIN PD. The penalty between optical BTB and 7-

channel 40-km fiber transmission in the $OFDMA_1$ signal parameter set is 0.8 dB. A receiver sensitivity of -16.5 dBm is achieved at BER = $1x10^{-9}$. The receiver sensitivity is -16 dBm for the $OFDMA_2$ parameter set, where the additional 0.5-dB penalty is mainly caused by larger in-band interference from square-law photodetection. The BER performance using a 10-GHz APD receiver is shown in Figure 28. Receiver sensitivities of -22.8 dBm and -22.3 dBm are achieved for C_{square} in $OFDMA_1$ and $OFDMA_2$ sets, respectively. Figure 28(a) also shows the electrical eye diagram of the C_{square} clock signal (recorded after 100s, corresponding to the long term maximum time interval error (MTIE)), after the Tx-side electrical power combiner 2 (Figure 23). The impairment on high and low clock states originates from the bi-directional electrical power combiners used in this experiment and can be mitigated by using directional components. Figure 28(b) and (c) show the transmitted C_{square} without and with $OFDMA_2$ + C_{sine2} signals, correspondingly.

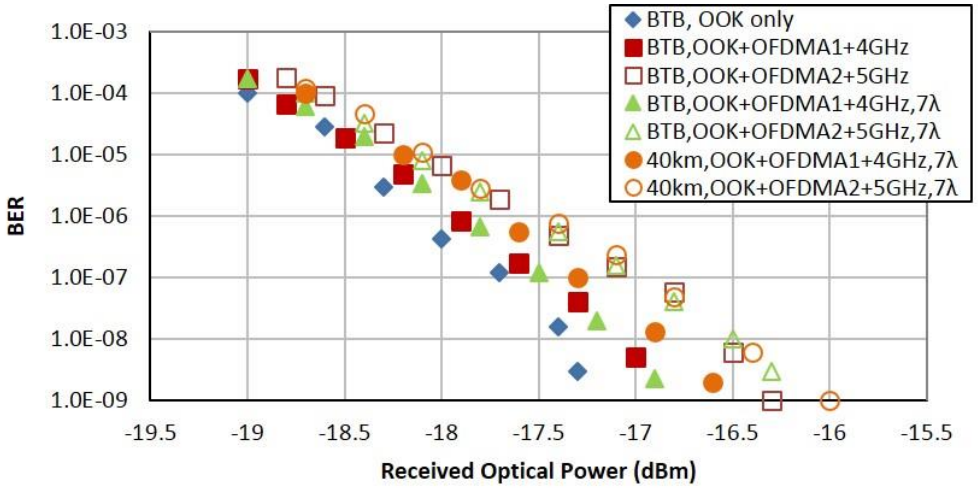

Figure 27. BER for C_{square} using 10-GHz linear PIN + TIA optical receiver.

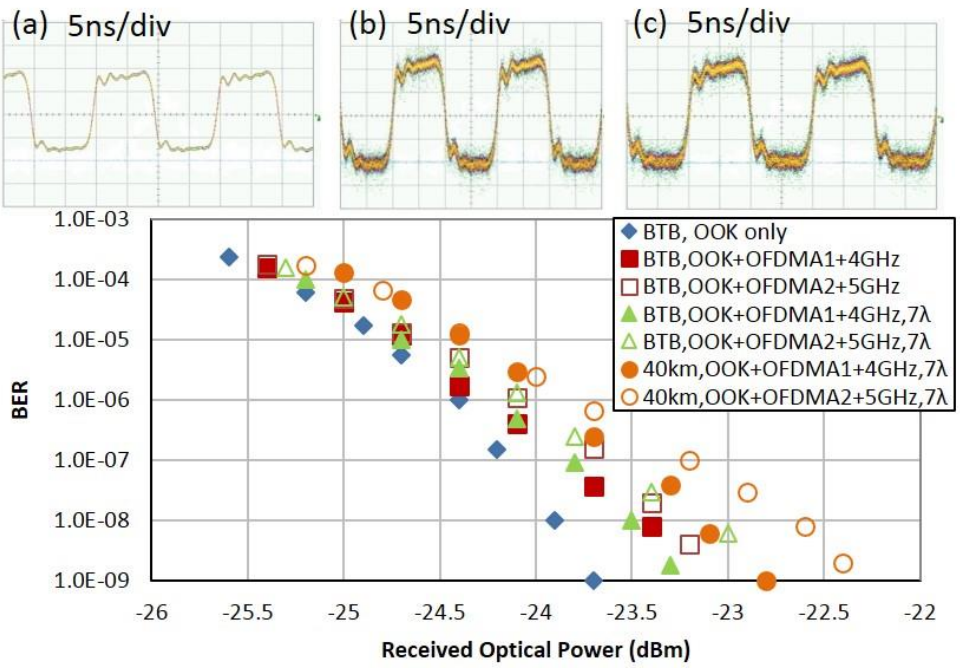

Figure 28. BER for C_{square} using 10-GHz APD + TIA optical receiver. Electrical eye diagrams for (a) C_{square} after power combiner 2, (b) C_{square} with 7 channels and 40-km fiber, and (c) C_{square} with $OFDMA_2$, C_{sine2}, 7 channels, and 40-km fiber at received power of -23.3 dBm.

In order to characterize the frequency and time synchronization accuracy of the proposed clock distribution and recover scheme, the time interval error (TIE) of two clocks is measured under various operating conditions and the MTIE as the key clock stability metric is calculated [65], [66], with the results shown in Figure 29 for the square clock and in Figure 30 for the sine clock. For both Figure 29 and Figure 30, the short term MTIE is computed off-line in MATLAB based on experimental measurements using both PIN and APD receivers, while the long term MTIE with the APD is measured directly from the real-time oscilloscope. The short term MTIE for C_{square} in Figure 29(a) indicates a minor difference between $OFDMA_1$ and $OFDMA_2$ signal parameters, confirming clock stability resilience for flexible data rates and sine clock frequencies. Moreover, MTIE performance

is typically better when an APD receiver is used due to higher receiver sensitivity. Figure 29(b) plots the long term MTIE for several received powers and $OFDMA_1$ and C_{sine1} transmission parameters using the APD receiver. As shown in Figure 29(b), a 0.113-ns MTIE increase from electrical BTB (purple crosses) to the 7-λ 40-km SSMF transmission with -16 dBm received power (small blue dots) shows weak nonlinearity effect caused by DWDM channels. Clock time accuracy within 1 ns is achieved with the proposed approach, dramatically exceeding the 1μs requirement for LTE-A in Table 2. In terms of frequency accuracy, in Figure 29(b), frequency accuracy is expressed as the slope from the origin to each MTIE point, with the 16ppb frequency accuracy slope indicated by the black solid line. As shown in Figure 29(b), the frequency accuracy of C_{square} under the proposed method exceeds LTE-A requirements by an order of magnitude, with fiber transmission and OFDMA/clock signal coupling exerting minimal MTIE degradation.

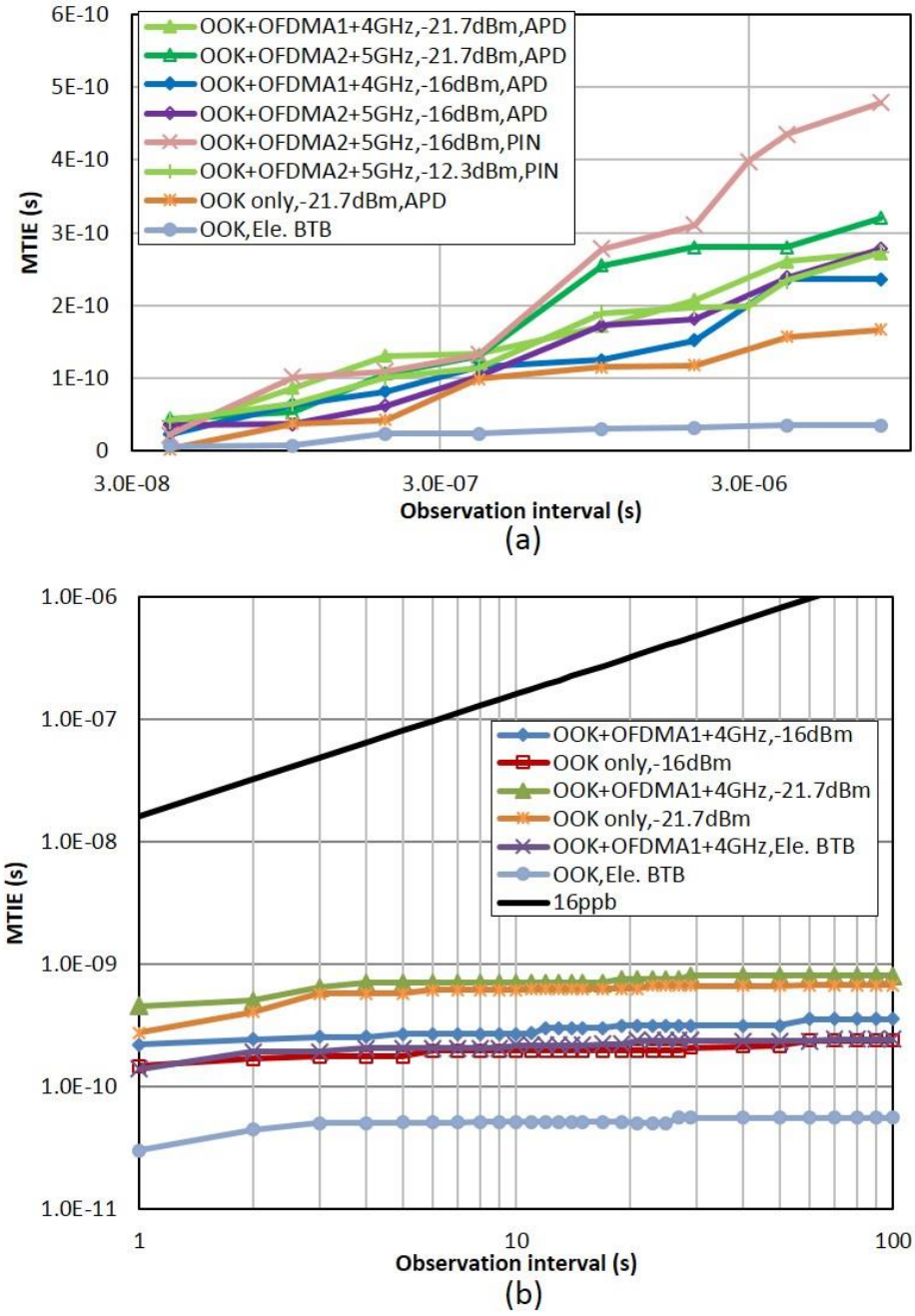

Figure 29. (a) Short term MTIE and (b) long term MIE vs. observation time interval for C_{square} after 40-km SSMF in the 7-λ DWDM-OFDMA system. C_{square} electrical BTB is also shown for reference.

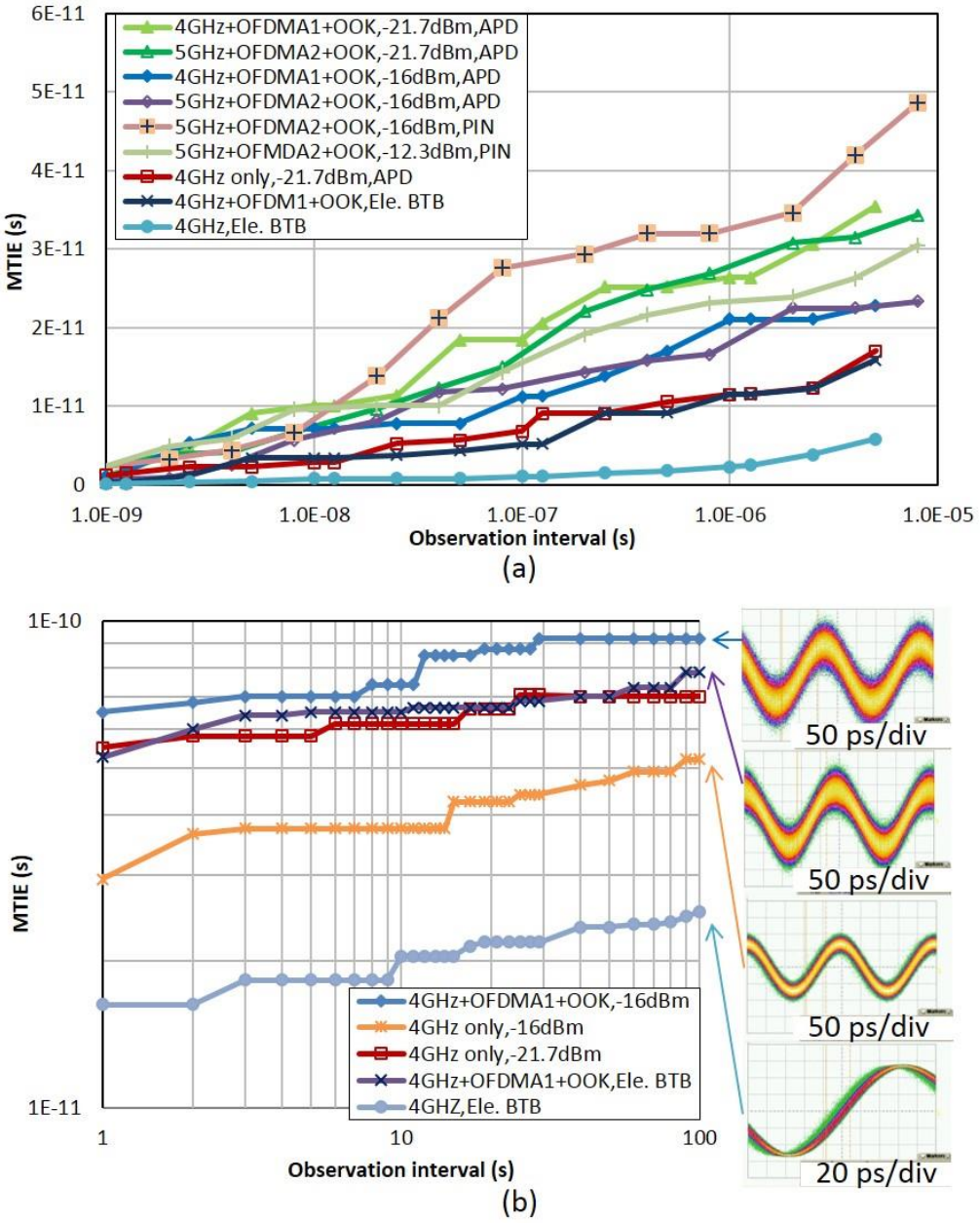

Figure 30. (a) Short term MTIE and (b) long term MIE vs. observation time interval for C_{sine} after 40-km fiber transmission in the 7-λ system. C_{sine} electrical BTB is also shown.

Figure 30 plots short and long term MTIE for the sinusoidal clock signal, C_{sine}. As shown in Figure 30(a), the MTIE penalty between 4-GHz and 5-GHz sine wave clocks is negligible, confirming the capability of flexible clock rate selection under the proposed

approach. As in Figure 29(a), in Figure 30(a), better MTIE results are achieved with the APD receiver due to higher receiver sensitivity. Comparison with electrical BTB results in Figure 30(b) shows that C_{sine} is more subject to jitter induced by electrical combining with other signals. The main interference to C_{sine} is caused by the OFDMA signal itself. However, this can be alleviated if a narrower BPF is used for C_{sine} recovery. Nonetheless, as shown in Figure 30(b), the worst-case C_{sine1} curve, received together with $OFDMA_1$ + C_{square} at -16 dBm received optical power produces a long-term MTIE of 9.2×10^{-11} s observed within a 100-s interval (the signal waveform superposed after 100 consecutive seconds is shown in the top inset in Figure 30(b)), which is far below the 16ppb mask drawn in Figure 29(b). Therefore, the experimental results for both the square and sine clocks achieve highly precise time and frequency accuracy, far exceeding LTE-A requirements of Table 2, and verifying the applicability of the proposed scheme to 4G and beyond optical MBH.

3.3 Synchronous Clock Distribution and Recovery for Coherent UDWDM-OFDMA-Based Optical MBH

UDWDM-PON, as a significant step forward for access system development, features channel spacing smaller than 12.5 GHz, high sensitivity, and complex data formats. However, different from direct detection, coherent detection produces random frequency offset and phase noise generated from the beating between the incoming signal and the optical LO. DSP is generally used to digitally filter the target channel from closely spaced neighboring channels and compensate the two aforementioned detection-generated products as well as propagation-related distortion. It introduces computational delays that can be too high for low-latency synchronization purposes. Therefore, a new

synchronization scheme is specially proposed for the UDWDM-OFDMA-based MBH, where clock distribution is similar to the previously introduced distribution method in the DWDM-OFDMA-based MBH, but clock recovery is based on DSP-free envelope detection.

3.3.1 Architecture and Operational Principles

Figure 31 illustrates the proposed coherent UDWDM-OFDMA-based MBH architecture with low-complexity synchronous clock distribution and recovery. At the central office optical Transmitter Tx_i, a square wave clock is first up-converted to a carrier frequency, f_c, modulated to produce an optical SSB signal and then optically combined with the intensity modulated OFDMA signal. The aggregate OFDMA+SSB clock signals on multiple wavelengths, λ_i, $i = 1, 2, \ldots, N$ are then optically coupled with tight UDWDM λ-spacing, f_s, producing the optical spectrum of Figure 31(a). To observe the DSP-free synchronous clock recovery capability of this spectrally-efficient approach, it is noted that the electric field of the aggregate OFDMA + clock signal on each λ_i, is given by

$$E_i(t) = a_i(t)\exp\{j[\omega_{ci}t + \varphi_{ci}(t)]\} + c_i(t)\exp\{j[(\omega_{ci} + 2\pi f_c)t + \varphi_{ci}(t)]\} \quad (1)$$

where $a_i(t)$ and $c_i(t)$ denote the OFDMA and square clock signals, respectively, and ω_{ci} and $\varphi_{ci}(t)$ are the optical source carrier frequency and phase. The output electric field of the wavelength-multiplexed signal is $E_{out}(t) = \sum_i E_i(t)$. Following SSMF transmission and coherent detection at the MBH Rx, the electrical current at the ED input is given by $I_i(t) = R \times \mathrm{Re}\left\{\overrightarrow{E_{out}}(t) \cdot \overrightarrow{E_{LOi}}^{*}(t)\right\}$, where R denotes photodiode responsivity and E_{LOi} is the LO electric field. Expanding $I_i(t)$ for the optical SSB clock modulation case yields

$$I_i(t) = Ra_i(t)\cos[\varphi_{ci}(t) - \varphi_{LOi}(t)] + Rc_i(t)\cos[2\pi f_c t + \varphi_{ci}(t) - \varphi_{LOi}(t)] + n_i(t) \quad (2)$$

where $\varphi_{LOi}(t)$ is the phase of the LO and $n_i(t)$ includes higher frequency terms that arise from beating with adjacent channels, as illustrated in Figure 31(b). An envelope detector (Figure 31) that operates at f_c with properly narrow bandwidth acts as a BPF as well as a low-frequency amplitude demodulator that recovers only the linearly-scaled clock signal, $Rc_i(t)$, as per Figure 31 (c), while removing all unwanted high-frequency *cos( )* terms in (2). Note that with optical DSB, however, after the ED, the remaining clock signal term in (2) would be $Rc_i(t) \times \cos[\varphi_{ci}(t) - \varphi_{LO}(t)]$, which would be degraded by phase noise and would require DSP-based compensation. With the proposed SSB approach and UDWDM, DSP-based compensation is not needed, high spectral efficiency is enabled, and both f_c and f_s can still be tuned to support spectral flexibility.

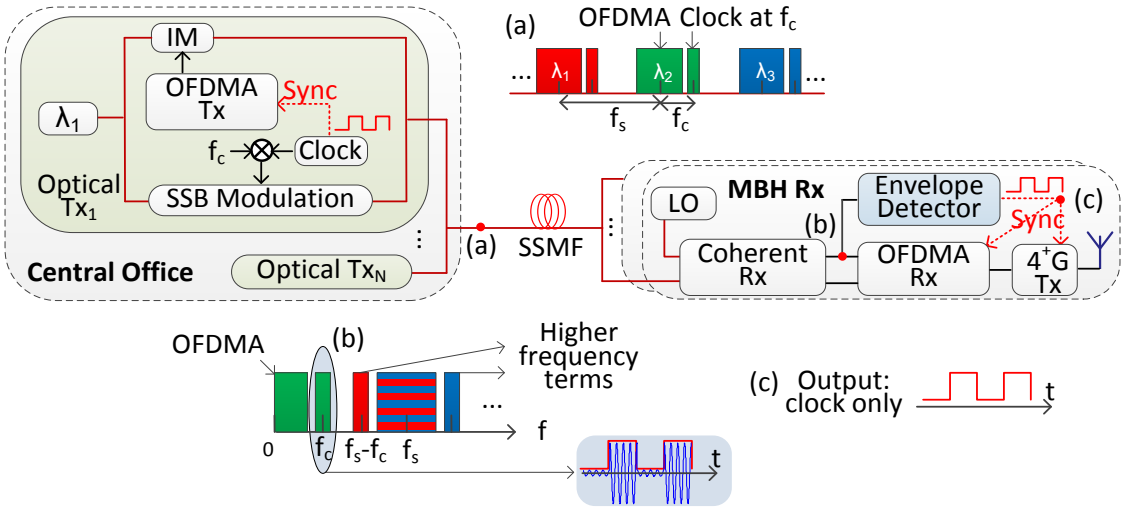

Figure 31. Schematic diagram of the coherent UDWDM-OFDMA-based MBH with synchronous clock distribution and recovery. (a) Optical spectrum of the launched signal. (b) Electrical spectrum of the signal after coherent detection (top), and waveform of the clock carried at f_c (bottom). (c) Electrical waveform of the envelope detector output, i.e., clock signal only.

3.3.2 Experimental Setup and Results

The experimental setup is depicted in Figure 32. CW optical signals from three external cavity lasers (ECLs) noted as ECL_1 to ECL_3 in Figure 32 with λ_1 = 1549.815nm, λ_2 = 1549.915nm, λ_3 = 1550.015nm are optically coupled with f_s = 12.5GHz channel spacing and applied to a 10GHz IM (IM_1 in Figure 32), which is driven by a 12-Gb/s OFDMA signal to first create three optical DSB-modulated wavelength channel outputs (Figure 33 (a)). The 12-Gb/s OFDMA signal is generated and continuously output by a 12GSa/s AWG, and featured FFT size of 256, with 16-QAM symbol mapping, 64 data-bearing subcarriers, 13% training sequence and cyclic prefix overhead, and 7% FEC overhead such that the net OFDMA data rate is 10 Gb/s/λ. The optical carrier from ECL_2 on λ_2 and a second 10GHz IM (IM_2 in Figure 32) are used for optical modulation of an electrical 50-MHz square wave clock signal which is up-converted to an intermediate RF frequency f_c = 6.25 GHz (Figure 33 (b)). Next, the optical clock and OFDMA signals are optically combined, boosted by an EDFA, and launched over the 40-km SSMF link (Figure 33(c)).

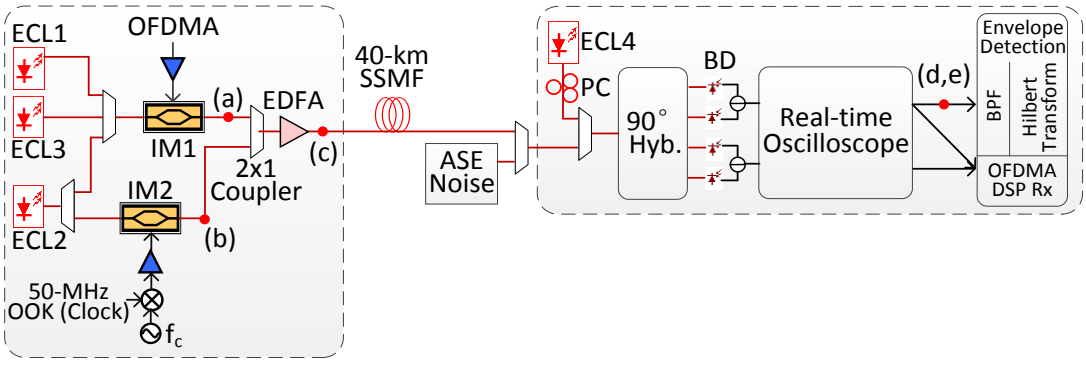

Figure 32. Experimental setup of the proposed clock distribution and recovery scheme for coherent UDWDM-OFDMA-based MBH.

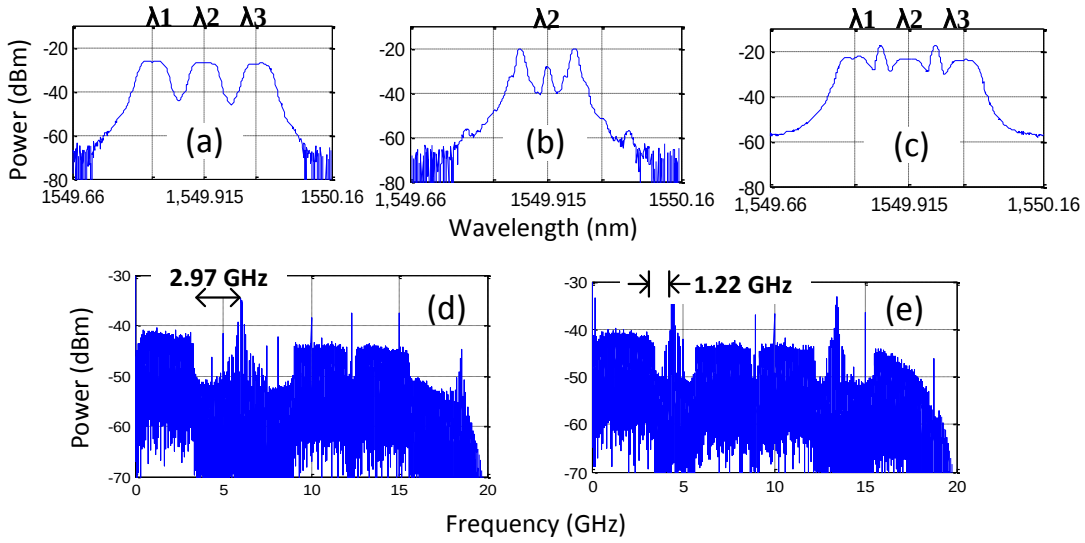

Figure 33. (a)-(c) The optical spectra (0.01nm resolution) measured at points a-c in Figure 32. (d) and (e) Electrical spectra measured at points d and e in Figure 32. Shown spectra (a)-(d) are for f_s = 12.5 GHz and f_c = 6.25 GHz. Spectrum (e) corresponds to the case f_s = 9 GHz and f_c = 4.5 GHz.

Following fiber transmission, the joint signal is coherently received using an LO laser ECL$_4$. The LO is tuned to all three channels (λ_1 to λ_3) for OFDMA demodulation, and centered at λ_1 and λ_3 to emulate optical SSB clock reception. An amplified spontaneous emission (ASE) source with an adjustable attenuator is also a coupled to the joint OFDMA/clock signal prior to the coherent receiver input in order to control and vary the optical signal-to-noise ratio (OSNR) of the link. Following coherent detection, a 40-GSa/s real-time oscilloscope is used to digitize both the OFDMA and clock signals, with the OFDMA signal BER obtained via off-line processing in MATLAB based on 0.5M bits. Due to hardware limitations, the envelope detection based clock recovery is also implemented via offline processing, wherein the ED consisted of a digital BPF with 1GHz bandwidth and a Hilbert transform, as shown in Figure 32. The experiment is then repeated for an even lower wavelength channel Hilbert transform, as shown in Figure 32. The

experiment is then repeated for an even lower wavelength channel spacing f_s = 9 GHz and clock up-conversion frequency f_c = 4.5 GHz to study the spectral efficiency limits of the proposed architecture. As shown in Figure 33(d) and (e), with the two choices of f_s and f_c, the frequency spacing between f_c and the nearest OFDMA signal edge is 2.97 GHz and 1.22 GHz, respectively.

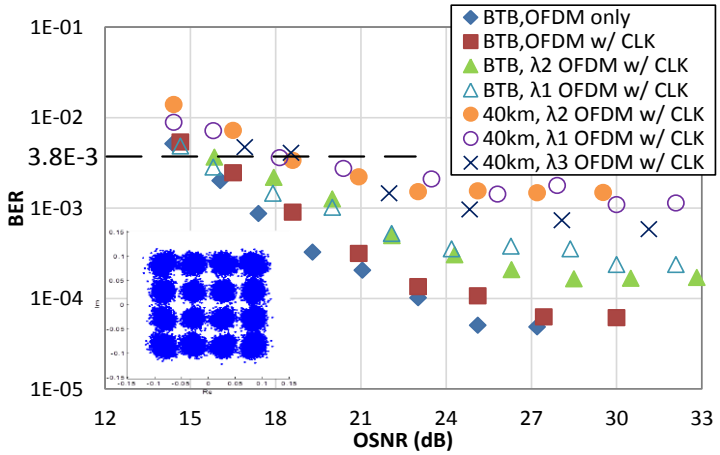

Figure 34. BER and constellation for the OFDMA signal with f_s = 12.5 GHz and f_c = 6.25 GHz. OFDMA constellation on λ_2 at BER = 3.3×10^{-3} with joint clock signal transmission over 40-km SSMF is also shown.

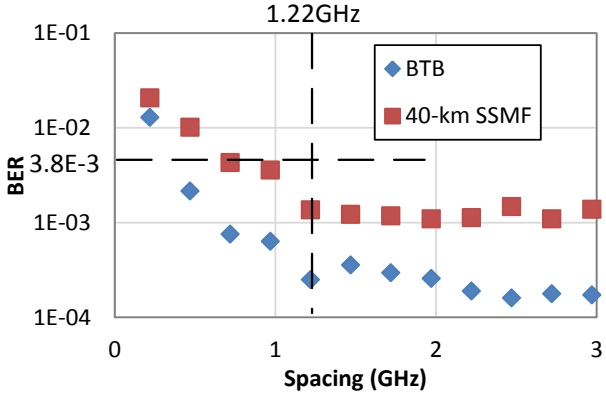

Figure 35. BER for the OFDMA signal on λ_1 vs. spectral spacing between f_c and OFDMA band edge.

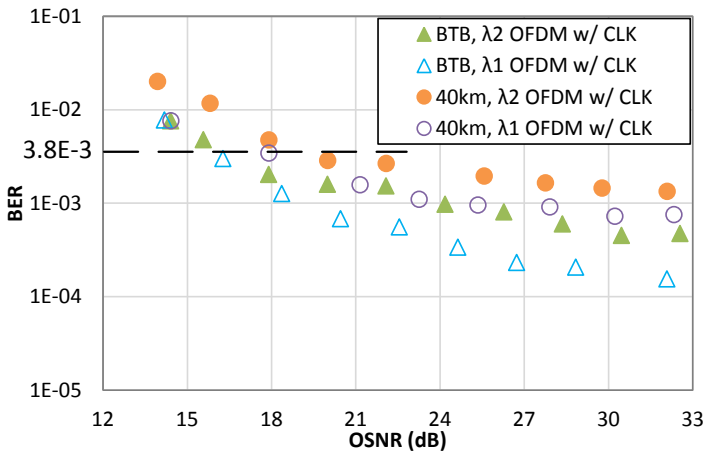

Figure 36. BER for the OFDMA signal with f_s = 9 GHz and f_c = 4.5 GHz.

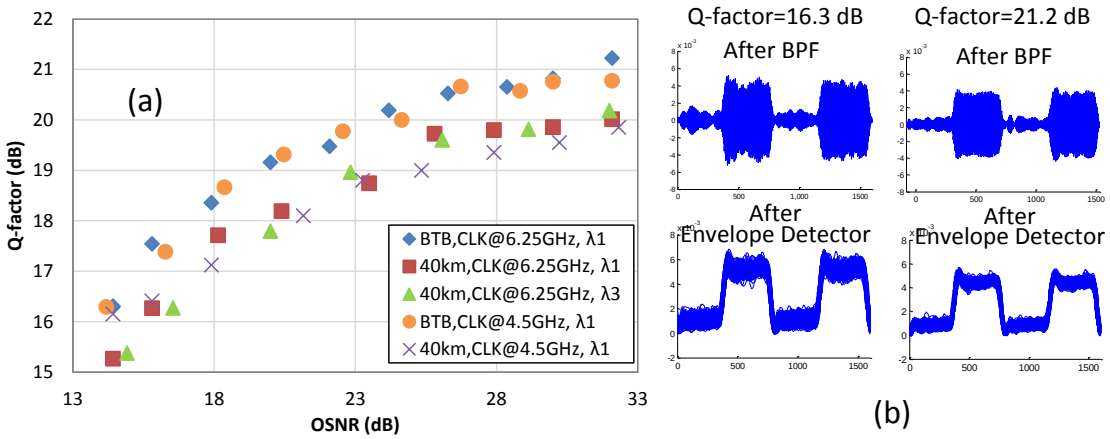

Figure 37. (a) Q-factor for the 50MHz OOK square clock. (b) Time-domain clock amplitude waveforms after the BPF (two clock cycles) and after the ED (repetitive clock cycles).

The experimental BER measurements for the OFDMA signal are illustrated in Figure 34-37. As shown in Figure 34, with f_c = 6.25 GHz, f_s = 12.5 GHz and 40-km SSMF transmission, the OSNR requirement for satisfying the 7% FEC limit (BER = 3.8×10^{-3}) for all wavelengths is approximately 18 dB, which amounts to a 3-dB OSNR penalty compared to optical BTB. As shown in Figure 34, the OSNR penalty induced by the clock signal

insertion is 0.5 dB, such that the additional 2.5-dB OSNR penalty is attributed to fiber nonlinearity effects during transmission, which arise due to tight frequency spacing between the OFDMA and clock signals. To study this spectral spacing limit, Figure 35 plots OFDMA BER as the spacing between the clock carrier frequency and the edge of the OFDM signal is reduced from 2.97 GHz to 0.22 GHz. As shown in Figure 35, BER degradation occurs when the spectral spacing is <1.22 GHz, which corresponds to f_c = 4.5 GHz. To maximize spectral efficiency, Figure 36 shows the OFDMA BER with f_s = 9 GHz and f_c = 4.5 GHz. Compared to Figure 34, similar OSNR requirements are observed, such that spectral efficiency is successfully enhanced without additional BER penalties. Experimental quality factor (Q-factor) [44] results versus OSNR for the 50-MHz square clock and sample waveforms are depicted in Figure 37(a) and (b), respectively. At OSNR = 18 dB, clock signal Q-factor of 17-18 dB is achieved after 40-km SSMF, corresponding to BER < 10^{-12} [44] and indicating virtually error-free clock operation and high clock quality.

3.4 Summary

In this chapter, a low-latency synchronous clock distribution and recovery scheme for DWDM-OFDMA-based optical MBH based on IMDD and DSP-free electrical filtering has been firstly proposed and demonstrated. A 50-MHz square clock and a 4/5-GHz sinusoidal clock have been experimentally distributed and recovered with an aggregate 41.09/51.31-Gb/s DWDM-OFDMA data transmission over 40-km SSMF and 25-GHz channel spacing. Signal and clock performance has been evaluated using both 10-GHz PIN and APD receivers, with no ONU-side optical amplification. Experimental results confirmed highly precise time and frequency accuracy, exceeding LTE-A requirements by

an order of magnitude. Secondly, a low-complexity synchronous clock distribution and recovery method for coherent UDWDM-OFDMA-based mobile backhaul based on optical SSB modulation and envelope detection has been introduced. Experimental verification of 30-Gb/s aggregate data rates with 50-MHz clock distribution in 24.56-GHz total spectrum over 40-km SSMF has been demonstrated with simple envelope-detection-based clock recovery. These works have achieved high data rates, high spectral efficiency, and simple low-latency synchronization, and can be a suitable candidate for future high-capacity optical MBH systems.

CHAPTER 4

SPECTRALLY-EFFICIENT OPTICAL FIBER SOLUTIONS FOR MOBILE FRONTHAUL

4.1 Introduction

BS architecture has been evolved together with the wireless generations. In the 1G and 2G era, most BSs used the so-called all-in-one architecture and were placed in cabinets with large refrigerators. Later, a distributed BS architecture was introduced for 3G deployment where the RRHs are separated from the BBUs using fiber links with digital baseband interfaces, such as CPRI. The concept of fronthaul was thus formed. As introduced in Chapter 1, C-RAN, an architecture that evolved the distributed BS architecture to BBU pooling and virtualization, is considered as a popular near-term MFH solution. Nonetheless, the excessive link rate of CPRI has drawn research attention and put the search for compression under scrutiny [49], [50].

LTE Release 10 introduces several key techniques to increase wireless data rate, including 8×8 MIMO for the DL [67] and carrier aggregation of up to 5 20-MHz CCs [51]. For the deployment of 4^{+}G cell sites with 3 RRHs (3-sectors), 5 aggregated 20-MHz carriers (100-MHz bandwidth), and 8×8 MIMO, there is a total of 120 20-MHz signals per direction. Consequently, the aggregated one-way traffic per cell would be around 150 Gb/s using CPRI interface. In this chapter, a DWDM-SCM-PON architecture is proposed for the future MFH to support high-capacity 4^{+}G cells while avoiding the excessive fronthaul rate. Due to the superior spectrum utilization of the SCM technique, the total occupied

bandwidth per wavelength can be reduced to less than 2 GHz. Significant reduction in the requirement on the number of wavelengths per cell site is also achieved. Moreover, complete analog frequency conversion is experimentally implemented, with real-time video streaming additionally delivered through the MFH testbed. Experimental results confirm high signal performances well exceeding the LTE-A requirements.

Spectrally-efficient UL solutions are also presented. The first method is based on IF-modulation in RRHs and coherent detection in BBUs, achieving channel spacing of as small as 100MHz. Successful coherent reception of LTE signal, whose symbol rate (15 ksps) is smaller than the laser linewidth, is achieved by pairing a RF pilot tone from each RRH. The second proposed UL scheme offers a low-complexity UDWDM over DWDM allocation with 1-GHz wavelength spacing and novel phase-noise-insensitive heterodyne detection using MHz-linewidth lasers and an off-the-shelf ED.

4.2 MFH Supporting LTE-Advanced Carrier Aggregation and 8×8 MIMO

4.2.1 Architectures and Performance Requirements

For a 4^{+}G cell site with three RRHs (commonly used for 3 sectors), five aggregated CCs, and 8×8 MIMO, a total of 120 20-MHz signals per direction is required. The CPRI line data rate for an RRH with 20-MHz bandwidth and 8×8 MIMO is 9.83 Gb/s. The CPRI document recommends the re-use of optical transceivers from the 10 Gigabit Ethernet standards, including Standard IEEE 802.3-2005 [68] clause 53 (10GBASE-LX4) and Standard IEEE 802.3-2008 [69], clause 52(10GBASE-S/L/E). Therefore, one cell site requires 15 wavelengths for the DL. For the UL, up to 4×4 MIMO and 5 aggregated carriers can be supported, also requiring 15 wavelengths each at 4.915 Gb/s. Figure 38 illustrates

an example of a 4+G DWDM-based MFH with CPRI interface using conventional 40-channel arrayed waveguide grating (AWG). The transmitters (Txs) and receivers (Rxs) of CO and RRHs can be 10GBASE-ER modules. The RF front end consists of principle radio components such as mixer, LO, and amplifier. It is noted that a typical DWDM-PON system with a pair of 40-channel C-band AWGs could only support one cell site using the CPRI approach.

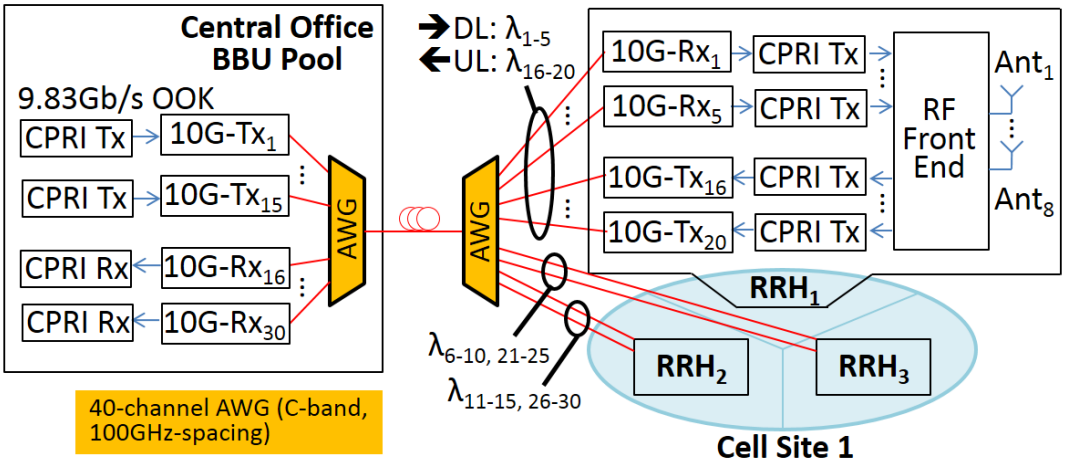

Figure 38. DWDM-PON for MFH using the conventional CPRI interface.

Figures 39 and 40 illustrate the proposed architectures of the DWDM-SCM-PON next-generation optical MFH featuring simple and low-cost RRHs and better wavelength utilization. As shown in Figure 39, the first proposed architecture also deploys a pair of 40-channel AWGs. At the CO OFDM Tx, a multi-IF OFDM signal, which maps 60 20-MHz CCs onto f_{IF1} to f_{IF60} with moderate guard bands, are generated by an OFDM Tx. In the case of contiguous carrier aggregation, the five aggregated bands can be viewed as a 100-MHz signal with a number of unused subcarriers placed between carriers. The multi-IF

OFDM signals are modulated on a total of 20 DL wavelengths λ_i, $i = 1, 2, \ldots, 20$ by optical transmitters (noted as OTxs in Figure 39) and multiplexed with DWDM λ-spacing (e.g., 100 MHz). The OTx can be a DML or a laser with external MZM. A 20-km SSMF link loss (LL) is estimated to be 10 dB, consisting of two 3-dB insertion losses from AWGs and 4dB propagation loss. The LL for the 40-km fiber case would thus be 14 dB. At a cell site, two DL wavelengths are detected by optical receivers (noted as ORxs), i.e., PDs. The electrical signals are then sent to an IF-RF front end, where each band is individually converted from its IF to the designated emitting RF f_{RFj}, $j = 1, 2, \ldots, 5$, using RF filters and mixers. As shown in Figure 39(a), 2×60 bands are frequency converted to 24 5-carrier-aggregated signals for transmission at three RRHs, each having eight antennas for 8×8 MIMO. The reverse RF processing takes place in the UL direction. Each cell site are assigned for two wavelengths from the 20 UL wavelengths λ_i, $i = 21, 22, \ldots, 40$. Due to high bandwidth efficiency of the proposed approach, the total occupied bandwidth can be less than 2 GHz, greatly reducing the optical bandwidth requirement of the optical transceivers. A 40-channel DWDM system can now support 10 cell sites because of the significant enhancement in wavelength utilization. Moreover, complicated computation and processing are performed in CO while simple and well-established RF processing is done at RRHs. This furthermore reduces round trip latency by removing extra processing introduced by CPRI interface, and paves the way for meeting 0.1 – 1 ms latency targeted for 4^{+}G system.

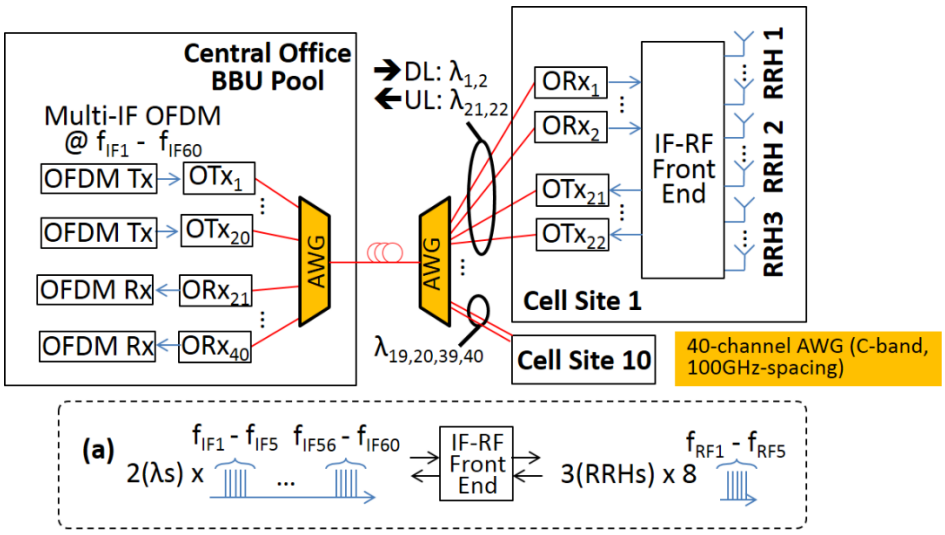

Figure 39. Proposed MFH architecture 1: DWDM-SCM-PON using conventional AWGs. The frequency conversion plan is inserted as inset (a).

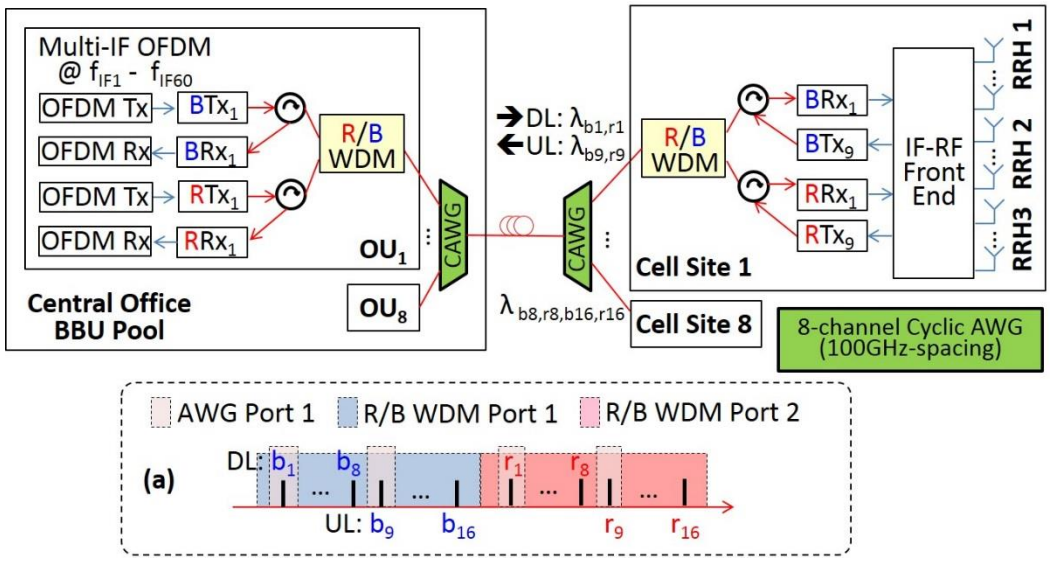

Figure 40. Proposed MFH architecture 2: DWDM-SCM-PON using cyclic AWGs (CAWGs) and red-blue wavelength-division multiplexers (R/B WDMs). The wavelength plane is inserted as inset (a).

The first proposed architecture offers a SCM-based MFH solution in a widely-recognized DWDM-PON system configuration. Recently, cyclic AWG (CAWG), considered as a key element that can enable incremental bandwidth upgrade, load balancing,

and power saving, is used in the time and wavelength division multiplexed PON (TWDM-PON) prototype [70]-[72]. Figure 40 illustrates another novel DWDM-SCM-PON architecture for the next-generation MFH deploying CAWGs and red-blue wavelength-division multiplexers (R/B WDMs). At the CO optical unit for cell site *m* (labelled as OU_m in Figure 40), where *m* = 1, 2, ..., 8, 120 20-MHz OFDM signals are generated by two OFDM Txs, each mapping 60 signals onto f_{IF1} to f_{IF60}, which has the same frequency allocation as Figure 39(a) presents. The two DL transmitters, BTx_m and RTx_m, produce wavelength λ_{bm} and λ_{rm} that are in the blue band (1529-1542 nm) and the red band (1547-1560 nm), respectively, and both are in the passband of the cyclic AWG port *m* (Figure 40(a)). The R/B WDM is preferred over splitter + filter to achieve low insertion loss (~0.6 dB) and low cost. The LL for a 20-km link in this case is estimated to be 16.4 dB, additionally from 0.6 dB per circulator, 5 dB per CAWG and 4 dB fiber attenuation. The 40-km LL is 20.4 dB correspondingly. At cell site *m*, the two DL wavelengths are separated by another R/B WDM and converted to electrical domain by two PDs. Same IF-RF conversion introduced previously in the proposed architecture 1 is followed. With the 8-skip-0 channel configurations of the CAWG, the UL wavelengths can be the next 8 channels (9 - 16) in both blue and red bands. The composite signals received in OU_m are then processed jointly by OFDM Rxs. The use of cyclic AWG and R/B WDM not only enables low starting cost and overall cost, but also greatly lowers the link loss. Additionally, power saving and flexible load control can be realized by turning CO transceivers on/off and dynamically changing the subcarrier number according to expected traffic load.

The DL EVM requirements are specified in the 3GPP standard: 17.5%, 12.5 %, and 8% for quadrature phase-shift keying (QPSK), 16-QAM, and 64-QAM, respectively [73].

The possible EVM degradation in the proposed SCM-based MFH can be the combined result of the optical and electrical impairments. Especially, the nonlinear effect would be carefully considered for such multi-subcarrier system. For example, due to the nonlinearity of the DML, harmonics and intermodulation products will be generated, which may consume power and overlap with original frequencies to cause interference-induced penalty [74]. As a result, a series of generic studies of the SCM transmission based on the proposed architectures is conducted and discussed next.

4.2.2 SCM Transmission in the Optical MFH

As described previously, by compactly mapping 60 CCs to pre-defined f_{IF1} to f_{IF60}, significant reduction in the requirements on both the number of wavelengths per cell site and the optical bandwidth of the optical transceivers can be achieved. Next, investigations on the intrinsic characteristics of SCM transmission in the proposed MFH using direct modulation and external modulation techniques are presented. Moreover, evaluation of the end-to-end system performance is completed with the experimental implementation of the RF processing primarily in the IF-RF front end.

4.2.2.1 Direct Modulation

The detailed experimental setup for the generic study of the SCM transmission is shown in Figure 41. First, direct modulation method is evaluated. A 1550-nm direct modulated DFB laser with 2-GHz bandwidth is deployed. In the experiment, it is chosen to evaluate the case of contiguous carrier aggregation, where five 20-MHz OFDM signals are carrier-aggregated (CA) as one 100-MHz signal. The 100-MHz contiguous band, which is the maximum bandwidth specified in the standards [51], imposes the most challenge on optical

and electrical components as well. Therefore, the 60×20-MHz CCs are grouped to 12 × 100M-Hz LTE-A-like CA-signals. An arbitrary waveform generator (AWG) at 5 GSa/s is used to produce the aggregated signal, in which each 100-MHz OFDM signal is generated in Matlab with an IFFT size of 2048 and a sampling rate of 150 MGa/s, consistent with the oversampling rate in LTE [75]. Training symbols are inserted in the OFDM symbol stream to aid channel estimation. The twelve CA-signals are located at $f_{IFn} = n \times 150\text{MHz}$, where $n = 1, 2, \ldots, 12$, so each signal is provisioned with a 50-MHz guard band. The peak to peak voltage (V_{pp}) of the AWG output is denoted as V_A. The signal is boosted by a PA with 20-dB power gain before driving the DML. After an EDFA, the SCM signal is launched to a L-km SSMF transmission link at 9 dBm (Figure 41(a)). At the cell site, the SCM signal is retrieved by an APD and sent to a real-time oscilloscope at 10 GSa/s for digitization and offline processing. Figure 41(b) depicts the electrical spectrum of the received signals before frequency conversion (yellow line) and their images (at negative frequencies), and one 100-MHz CA-signal after frequency downconversion (pink line).

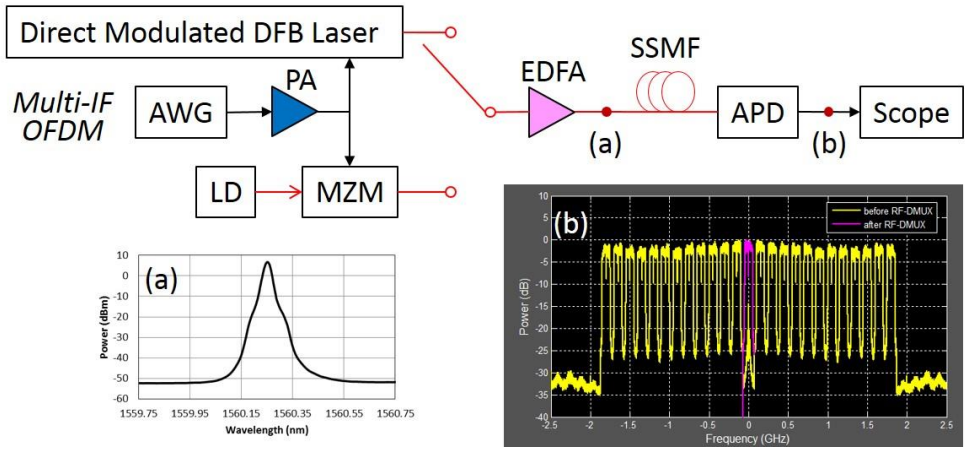

Figure 41. Experimental setup of the generic SCM transmission in the MFH. (a) Optical spectrum of the launched signal. (b) Electrical spectrum of the received 12 × 100-MHz LTE-A-like CA-signals and their images.

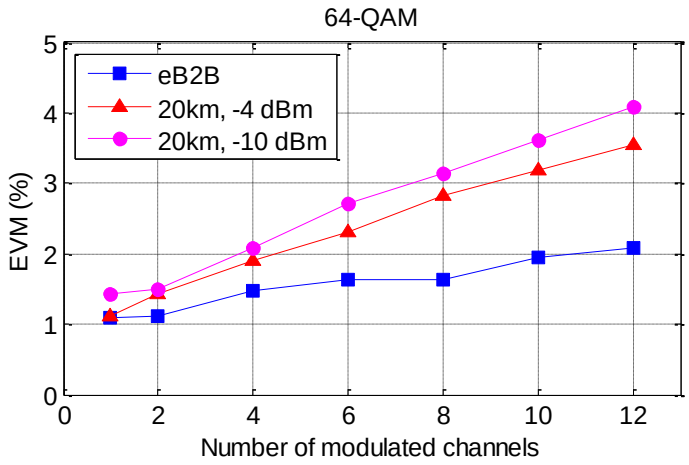

Figure 42. EVM vs. the number of IFs in the eBTB case and after 20-km transmission with a DML-based optical transmitter.

The EVM performance in the electrical BTB (noted as eBTB in Figure 42) case is firstly examined by connecting AWG directly to the oscilloscope. In Figure 42, blue square marks show the average EVM of all 64-QAM-OFDM CA-signals as a function of the number of IFs. The aggregation of the signals from one to twelve causes an EVM increase of ~1% due to the reduction of the effective number of bits (ENOB) of the DAC and ADC used. The optical BTB performance of the twelve CA-signals with respect to received optical power is shown in Figure 43(a). V_A is initially set to the maximum output value, i.e. 700 mV, corresponding to an optical modulation index (OMI) of ~80%. At -4 dBm received power, an average EVM of ~2.8% is obtained, indicating an EVM increase of 0.7% induced by the optical link. Figure 43(b) plots the EVM after the 20-km fiber transmission. It is clearly noted that the strong electrical driving voltage results in a monotonic EVM degradation with the increase of signal IF frequency. The DML-based coexisting transmission is mainly impaired by the intermodulation among subcarriers due to the interplay between dispersion and DML chirp [74]. The uniform performances among

twelve subcarriers in Figure 43(a) allow concluding that electrical to optical conversion in the DML and optical to electrical conversion in the APD are not the primary cause to the intermodulation distortion, while observations from Figure 43(b) indicate that the main origin of intermodulation is the SSMF dispersion-induced distortion. The impairment of the nonlinear effect can be reduced by lowering the electrical driving voltage so as to reduce the OMI of the DML, albeit with the tradeoff of reduced signal strength. As shown in Figure 43(c), enhanced uniformity among the twelve channels is obtained by reducing the AWG output amplitude to 350 mV, corresponding to an OMI of ~40%. An EVM increase of 0.7% is observed at -4-dBm received power compared with Figure 43(a) due to the 20-km fiber propagation and weakened signal strength, leading to about 3.5% overall EVM. The target of 8% EVM is met with -16.5-dBm received optical power. For practical operations, 4% EVM achieved at -10-dBm received power is favorable, leaving 6 dB EVM margin for other impairments, e.g., the PA distortion prior to the antenna. With the transmitted power of 9 dBm and the received power of -10 dBm, the power budget is 19 dB, leaving 9-dB power margin in the proposed architecture 1 using conventional AWGs and 2.4-dB margin in the second architecture using CAWGs. In application scenarios where full 12 × 100-MHz configuration is not needed, for example, 4×4 MIMO or less carrier aggregation, the proposed scheme is able to flexible adjust the number of subcarriers according to the traffic need. The measured EVM value as a function of the subcarrier number after 20-km fiber transmission is plotted in the red triangles and pink dots in Figure 42, which are measured at the received optical power of -4 dBm and -10 dBm, respectively. It is observed that nonlinearity-induced penalty is evidently reduced when less subcarrier channels (with smaller overall signal bandwidth) are transmitted. Moreover, additional

intermodulation mitigation techniques can be applied to further improve signal quality for DML-based fronthaul transmission [76].

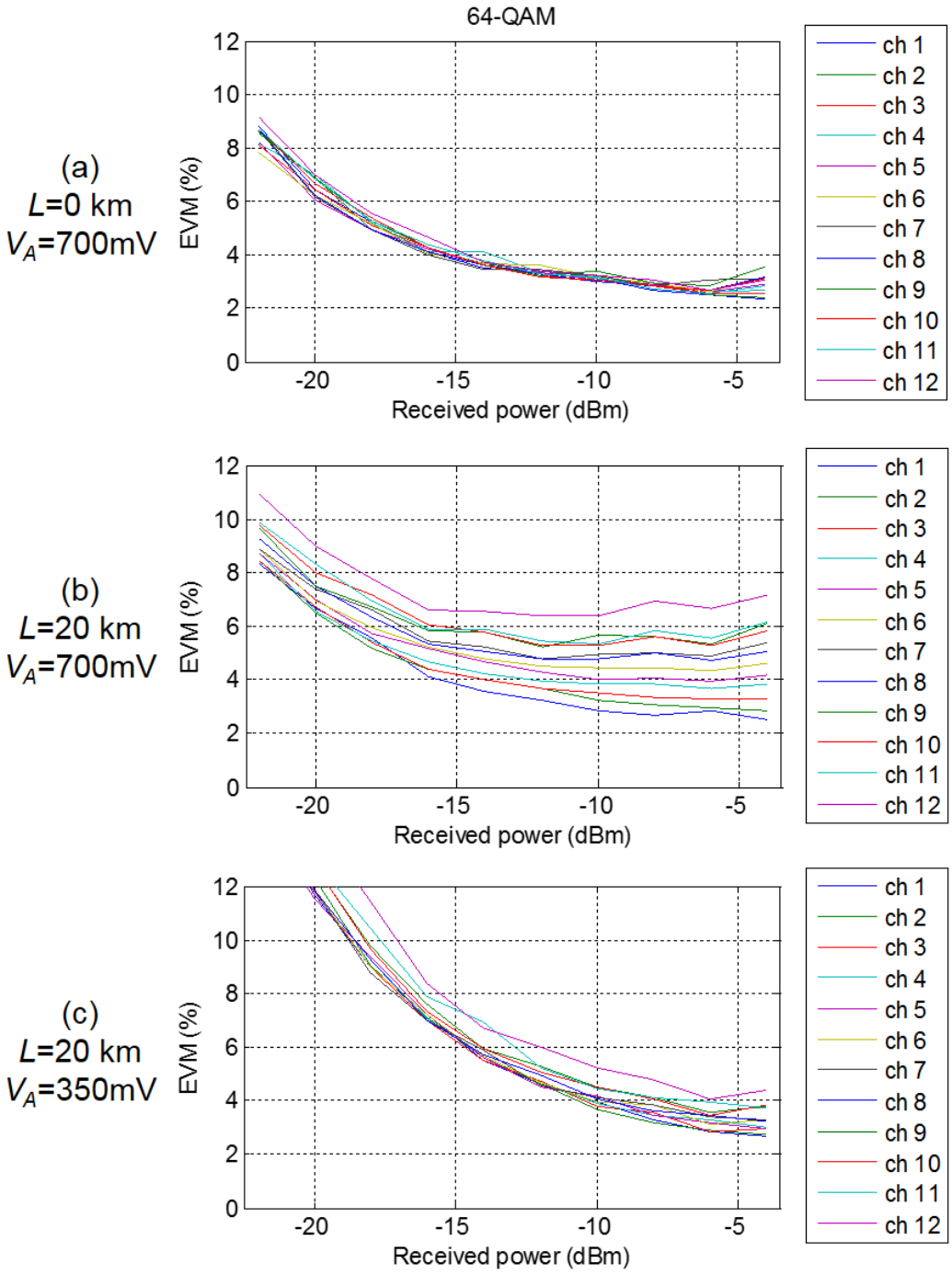

Figure 43. EVM vs. received optical power in three configurations: (a) L = 0 km, V_A = 700 mV; (b) L = 20 km, V_A = 700 mV; (c) L = 20 km, V_A = 350 mV.

4.2.2.2 External Modulation

The second optical modulation method analyzed in this paper is the MZM-based external modulation. The optical output from a DFB LD is intensity modulated with the above-mentioned 12×100MHz LTE-A-like CA-signals by a 3-GHz MZM, as shown in Figure 41. The rest of the experimental configurations are the same as the direct modulation experiment. Figure 44(a) and (b) show the EVM measurements of the 12 100-MHz 64-QAM-OFDM signals with respect to received optical power in optical BTB and 40-km SSMF transmission cases, respectively. It can be observed that negligible penalty is induced after 40-km fiber transmission, indicating the immunity of the system to fiber CD and nonlinearities. This can be attributed to the chirp-free modulation of MZM. Measurements are compared with the EVM requirements specified in the 3GPP standard: 17.5%, 12.5 %, and 8% for QPSK, 16-QAM, and 64-QAM, respectively [73]. As shown in Figure 44(b), the target of 8% EVM is achieved at -19-dBm received optical power. The desired 4% EVM is met with -10-dBm received optical power after 40-km transmission, indicating 19-dB power budget, same as the DML result obtained with 20-km propagation. Figure 44(c) and (d) show the EVM results of the received 16-QAM and QPSK signals after 40-km fiber link, correspondingly, achieving similar EVM performance as the 64-QAM case. This means that more power margin can be obtained by reducing the constellation size. In summary, with MZM-based external modulation, high-quality uniform performance of the twelve CA-signals is attained over 40-km fiber transmission with negligible penalty. Direct modulation, on the other hand, is also able to have EVM of $\leqslant$4% over a 20-km SSMF fronthaul link with proper power management.

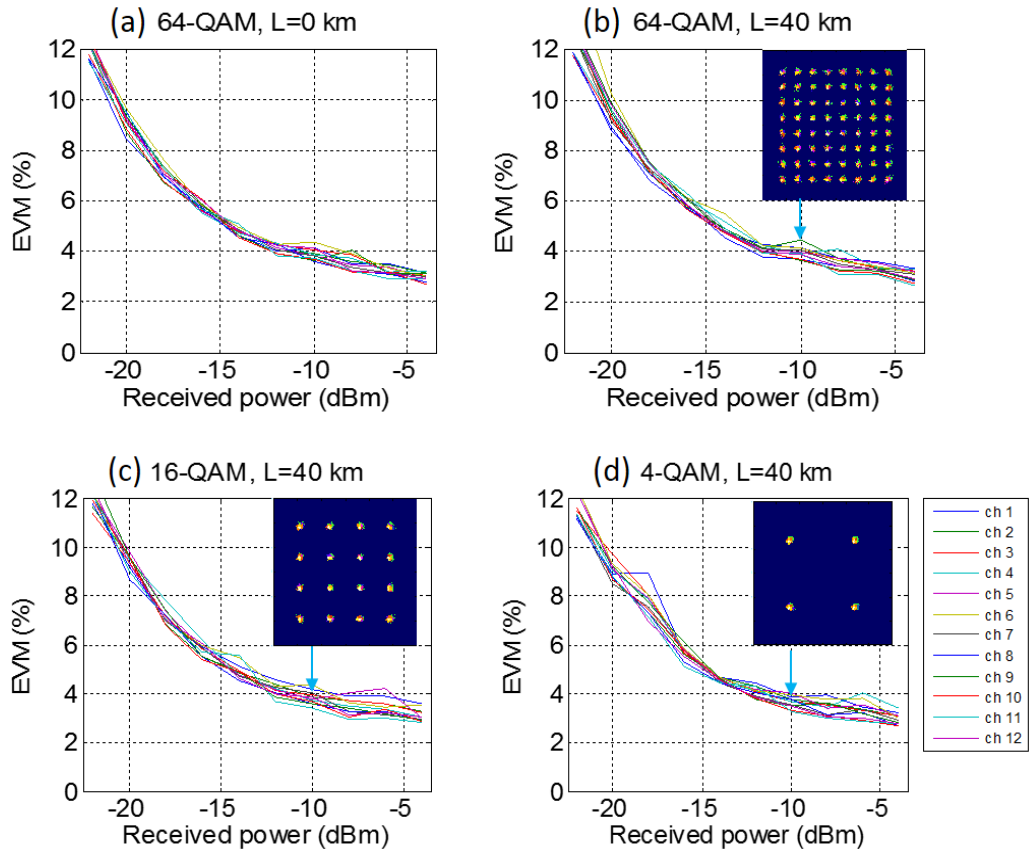

Figure 44. EVM vs. received optical power with different modulation schemes and fiber length *L*: (a) 64-QAM, *L*=0; (b) 64-QAM, *L*=40 km; (c) 16-QAM, *L*=40 km; (d) QPSK, *L*=40 km.

4.2.2.3 Complete RF Processing

The implementation of analog RF processing, including frequency combination and conversion in the SCM-based mobile fronthaul system is additionally demonstrated to emulate a complete fronthaul link that is compatible with current BBU and RRU equipment, as shown in Figure 45. It is noted that the DL twelve CA-signals can be digitally generated together by an OFDM Tx in the CO indicated in Figure 39 and 40. However, the RF-to-IF frequency conversion and coupling are necessary in the IF-RF front end at the RRH for the UL. Therefore, in order to cover complete RF processing occurring in the

fronthaul system, integration of frequency downconversion, upconversion, coupling, splitting, and filtering are included in the testbed. The output 1 of the AWG (labelled as AWG_1 in Figure 45) generates a 100-MHz 64-QAM-OFDM CA-signal centered at f_{RF1} = 2.46 GHz, to emulate a LTE-A signal to be transmitted. It is downconverted to f_{IF1} =150 MHz by an image-reject mixer with a 2.31-GHz LO signal (Figure 45(a)). The output 2 the AWG (labelled as AWG_2 in Figure 45) generates the 2^{nd} – 12^{th} CA-signals carried at f_{IF2} – f_{IF12} (Figure 45(b)). The two outputs are passively combined (Figure 45(c)) to drive the MZM. After optical transmission, the electrical signal is retrieved by an APD (Figure 45(d)). A 190-MHz LPF is used to filter the 1^{st} CA-signal in this setup. Finally, the selected CA-signal is upconverted to the intended RF frequency by a single-sideband RF modulator for wireless transmission. Figure 45(e) and (f) shows the upconverted signal with and without the LPF. Ideally, a BPF operating at the f_{RF} is used to clean up the adjacent signals before the radio signal is emitted to the air. In the experiment, the RF BPF is implemented in the offline processing.

Figure 46 illustrated the EVM for the targeted band with various RF processing. Remarkably, based on the first three curves (blue diamonds, red squares, and green triangles), both frequency downconversion and upconversion introduce no EVM penalty. Combining the 1^{st} CA-signal with the other 11 CA-signals, as purple crosses indicate, causes an EVM increase of ~2%, mainly due to less effective modulation power per band after the combination. From the last two curves in Figure 46, it is observed that the LPF can be removed without introducing noticeable penalty. Removing the RF filter before the frequency upconversion greatly increases the flexibility in IF assignment. The experiment is then repeated for f_{RF2} = 2.6 GHz with the LO tuned to 2.45 GHz. As shown in Figure 47,

4% EVM is again achieved at -10-dBm received power after 40-km fiber propagation, indicating robustness in operating frequency.

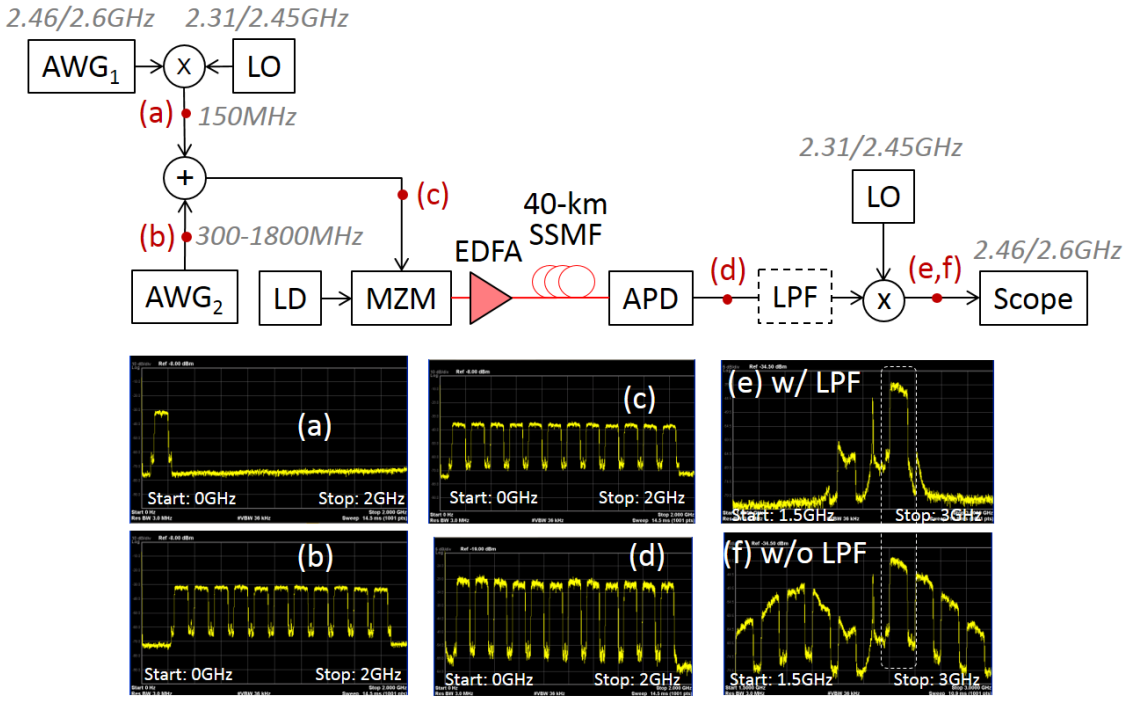

Figure 45. Complete single-wavelength configuration with RF processing in the proposed SCM-based MFH. Inset (a)-(f): electrical spectra at selected locations.

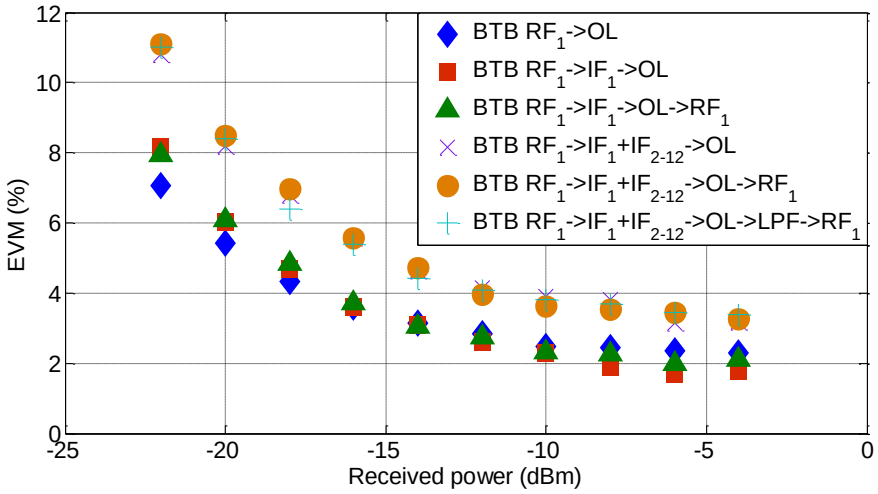

Figure 46. EVM measurements with f_{RF1} = 2.46 GHz. OL: optical link.

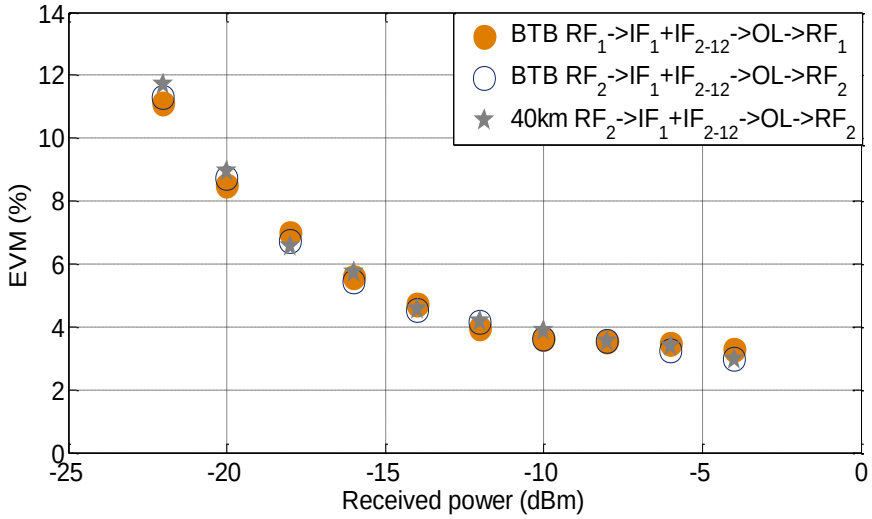

Figure 47. EVM measurements with f_{RF2} = 2.6 GHz.

4.2.3 Real-Time MFH Testbed with Video Streaming

To further validate the low-latency feature and practicability of the proposed scheme, Figure 48 shows the experimental setup of the real-time SCM-based optical MFH demonstration. Wi-Fi connection is established through the fully converged multi-IF system setup to emulate the 4G LTE-A deployment. A pair of REALTEK 11n USB Wi-Fi adapters are connected to two personal computers (PCs) (Figure 48(a)). Wi-Fi DL and UL are separated by electrical circulators. More specifically, the downstream Wi-Fi signal carrying video stream is generated by the adapter in the transmitter and delivered via the optical testbed to the receiver adapter for real-time video display. The UL carrying feedback information passes two attenuators and a unidirectional PA which can further increase the isolation of the two links and avoid downstream signal leaking through the UL. As illustrated in Figure 48(b), the generated Wi-Fi signal is a 20-MHz channel at 2.412 GHz. An LO at 2.262 GHz is used to downconvert the Wi-Fi signal to f_{IF1} = 150 MHz. It is then combined with the 2nd – 12th 100-MHz CA-signals carried at f_{IF2} – f_{IF12} (Figure 48

(c)) to form the new converged multi-IF signal (Figure 48(d)). The aggregated signal is externally modulated by the 3-GHz MZM and launched to a 1-km fiber link. As mentioned in Chapter 2, the fiber length is currently limited by the $ACK_{timeout}$ defined in Wi-Fi MAC layer [61]. The first IF signal is again selected by the 190-MHz LPF and upconverted back to the original Wi-Fi frequency (Figure 48(e)). It is then filtered by the build-in matching filter in the receiver adapter before data demodulation for instant video display. Clear and continuous pictures are successfully played. Besides the video streaming in the proposed SCM-based MFH system, real-time Internet access of the receiver PC, by setting the transmitter PC as a hotpot, is also demonstrated.

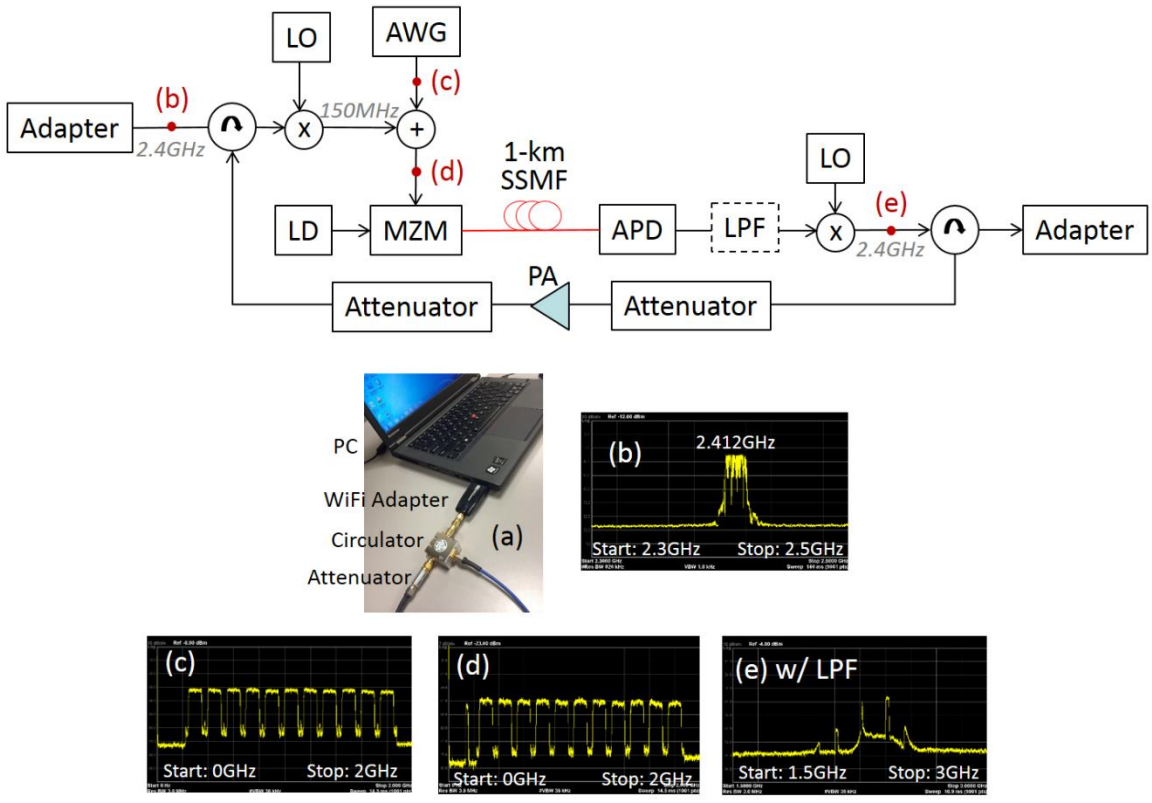

Figure 48. MFH testbed with real-time Wi-Fi video streaming integrated in the SCM system. (a) Picture of the Wi-Fi adapter connection. (b)-(e) Electrical spectra at selected locations.

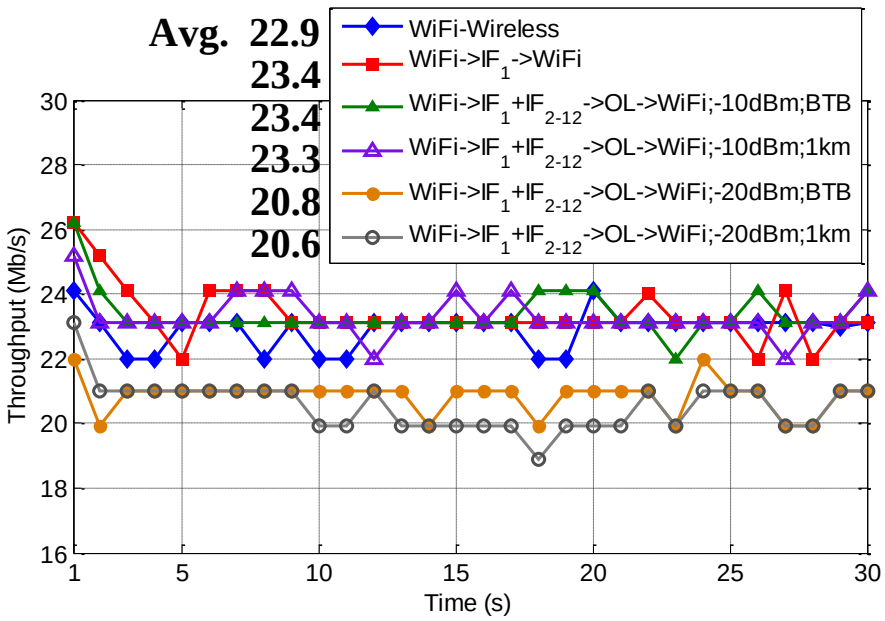

Figure 49. Wi-Fi throughput in a 30-s interval for conventional Wi-Fi wireless link and the SCM-based MFH system.

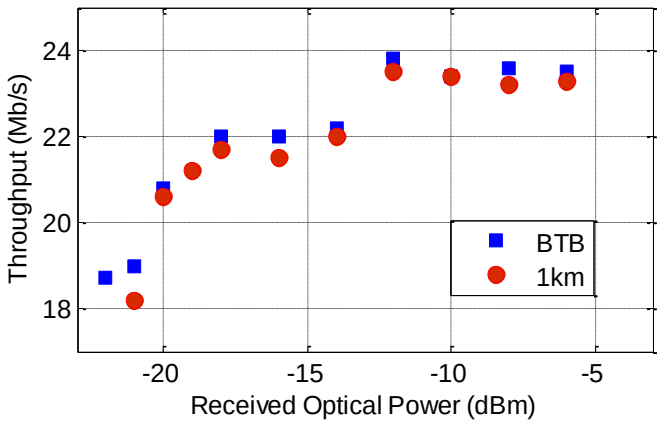

Figure 50. Wi-Fi throughput vs. received optical power in the SCM-based MFH.

To further quantify the transmission performance, Wi-Fi throughout is measured by Iperf [60]. As shown in Figure 49, Wi-Fi throughput is recorded in a 30-s interval in different setup: wireless antenna to antenna; frequency conversion; complete RF processing + optical link (OL). Remarkably, the average Wi-Fi throughput obtained in the

optical testbed with -10-dBm received optical power is higher than the conventional wireless transmission, mainly because the latter encounters interference from other Wi-Fi radio signals and wireless propagation impairments. High stability is also achieved. Figure 50 illustrates the average throughput in 30 s vs. received optical power in the SCM system. As the received power decreases, Wi-Fi adapters will automatically adjust the modulation schemes, resulting in the drop of throughput. Negligible power penalty is induced by the 1-km fiber transmission, consistent with the theoretical analysis in [61]. The average EVM of the 2nd - 12th 64-QAM-OFDM CA-signals is measured in coexistence with the 100-MHz CA-signal and the mapped Wi-Fi signal, as shown in Figure 51. The two EVM results shows negligible difference, confirming the stability and flexibility in data format selection under the proposed approach. Therefore, the experimental results based on both direct modulation and external modulation achieve low EVM of ~4%, far exceeding 3GPP EVM requirements. With the implementation of analog frequency conversion and real-time video demonstration, the proposed scheme is verified for the applicability of to 4G and beyond optical MFH.

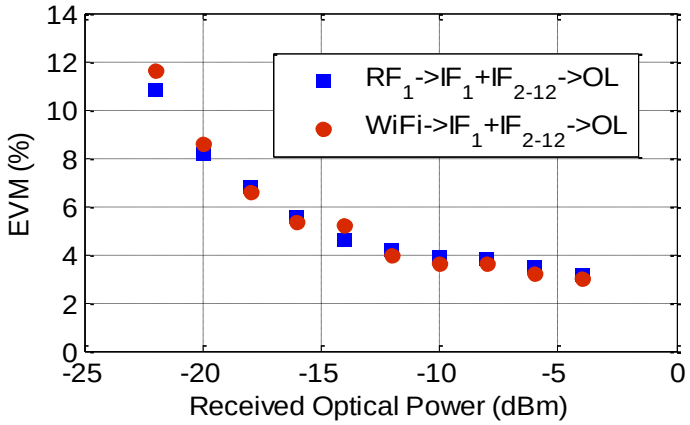

Figure 51. Average EVM of the 2nd-12th 64-QAM-OFDM CA-signals.

4.3 Spectrally-efficient Structures for MFH UL

4.3.1 Motivation and Technical Challenges

In the previous section, SCM-based MFH structures are presented deploying 2-GHz optical transceivers in both CO and cell sites and 4 DWDM wavelength channels per cell site to support 3 sectors, 8×8 MIMO, and 5 aggregated carriers. This section explores architectures and supporting techniques that can enable additional wavelength resource sharing. The concept of flexible and dynamic wavelength resource allocation and optimization has drawn researchers' attention in recent years. Previously proposed Flex-PON [77] and SDN [78] for optical access networks laid solid foundations for elastic spectrum allocation with customized provisioning metrics on-demand. MFH upstream transmissions, which are generally in lighter deployment scenarios with fewer number of sectors, antennas, and frequency bands, can benefit the most from the spectrally-efficient wavelength sharing. For example, within a DWDM grid, spectrum can be locally assigned to a group of cell sites based on UL traffic demands. As a result, multiple cell sites may share one DWDM channel instead of occupying a number of separated DWDM channels.

It is worth noting that SCM is naturally suitable and expandable for one-to-many DL in the PON configuration. However, different modulation and detection methods may be needed for the many-to-one UL. Specifically, optically aggregated signals from multiple cell sites that have the same central carrier wavelength but different IFs cannot be directly detected since the combined central carrier loses coherency with the subcarriers. Coherent reception is usually needed in the CO for such transmission [55], [56]. However, coherent detection of LTE signals is difficult, since the symbol rate of current LTE signal is 15 ksps, smaller than laser linewidth (typically ranges from tens of KHz to tens of MHz), and

conventional pilot subcarriers that are across OFDM spectrum cannot be used. An external RF pilot tone is proposed to be paired with UL signal from each cell site for frequency offset estimation and phase noise recovery. Moreover, another UL approach is introduced to provide an alternative to coherent SCM-PON. This scheme multiplexes preprocessed upstream signals with closely located wavelengths in each DWDM channel and allows DSP-free heterodyne detection, thus achieving high spectral efficiency and low complexity.

4.3.2 Architectures and Operational Principles

Two MFH systems with spectrally-efficient wavelength sharing are described next. Architecture-wise, scheme (1) keeps DWDM-SCM-PON for both directions, while scheme (2) has DWDM-SCM-PON for DL and UDWDM over DWDM-PON for UL. From the modulation and detection perspectives, both scheme (1) and (2) are based on IM-DD for DL, but the former has coherent detection for UL and the latter has phase-noise-insensitive heterodyne detection.

4.3.2.1 MFH System (1) with SCM-Based UL and Coherent Detection

The MFH deployment of one RRH per cell site without MIMO and carrier aggregation is used purely as an example to demonstrate the fundamental principles of wavelength sharing among cells. Taken such simplification into account, Figure 52 illustrates the bi-directional DWDM-SCM-PON architecture. At the CO optical transmitter Tx_m, m = 1, 2, …, M, the OFDM signal for RRH_{m_n}, n = 1, 2, …, N, is first upconverted to IF_{m_n}, which can be written as $V_{SD_{m\_n}}(t) = \mathrm{Re}\{A_{D_{m\_n}}(t)e^{j\omega_{IF_{m\_n}}t}\}$, where $A_{D_{m\_n}}(t)$ is the baseband complex-valued signal for wireless users and $\omega_{IF_{m\_n}}$ is the angular frequency of the

assigned IF carrier. It is then electrically combined with signals at different IFs and modulated by an IM. The electrical field at the output of each Tx_m can be written as

$$E_{Tx_m}(t) = \left[\sum_n V_{SD_{m\_n}}(t)\right] \cdot e^{j[\omega_m t + \varphi_{Dm}(t)]} \tag{3}$$

where ω_m and $\varphi_{Dm}(t)$ denote the Tx_m optical source carrier frequency and phase. The aggregated multi-IF signals at different wavelengths, λ_m, are multiplexed by a DWDM arrayed-waveguide grating (AWG), as shown in Figure 52(a). The electric field after the AWG is given by $E_{DL}(t) = \sum_m E_{Tx_m}(t)$. At the RN, each wavelength is demultiplexed by another AWG and split to a group of RRHs. At RRH_{m_n}, The IF-RF front end filters the OFDM signal carried at IF_{m_n} and frequency-converts it to the emitting RF.

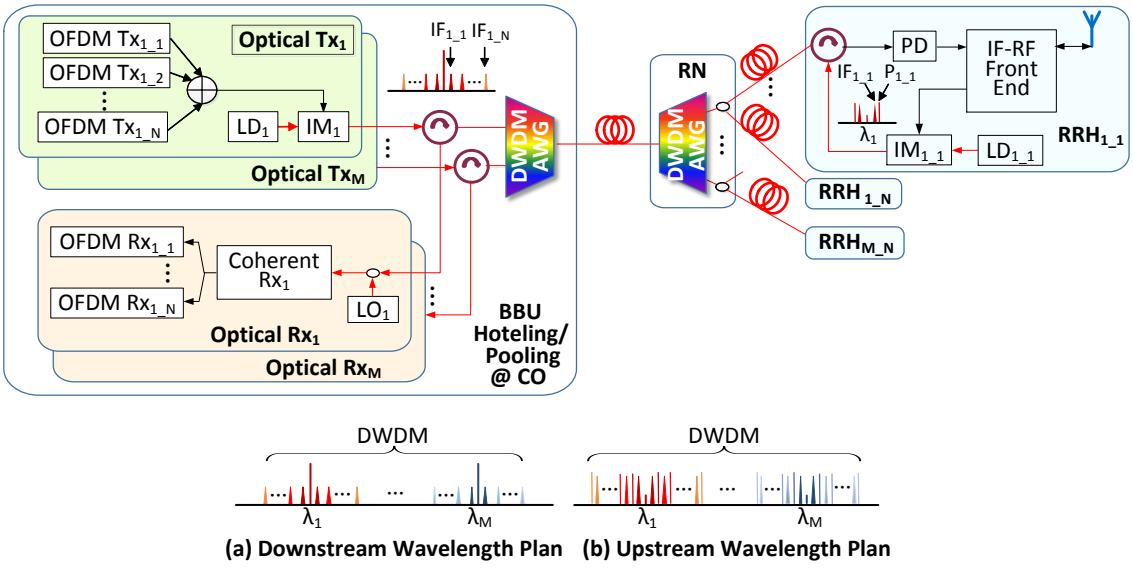

Figure 52. Proposed MFH architecture (1). DL and UL: DWDM-SCM-PON. (a) and (b) Downstream and upstream wavelength plan, respectively.

Similarly, the upstream RF signal received by RRH_{m_n} is converted to IF_{m_n}, which can be written as $V_{SU_{m\_n}}(t) = \text{Re}\{A_{U_{m\_n}}(t)e^{j\omega_{IF_{m\_n}}t}\}$, where $A_{U_{m\_n}}(t)$ denotes the UL

baseband complex-valued signal. Due to the small symbol rate and subcarrier spacing of the wireless signal compared with optical laser linewidth, conventional pilot subcarriers across OFDM spectrum cannot be used. An external pilot tone is added with the converted OFDM signal. The pilot signal is represented by $V_{P_{m\_n}}(t) = A_{P_{m\_n}}\cos(\omega_{P_{m\_n}}t)$, where $A_{P_{m\_n}}$ and $\omega_{P_{m\_n}}$ are its amplitude and angular frequency. The paired signal is then modulated onto a lightwave at λ_m by an IM biased at the null point, since the central carrier needs to be suppressed and replaced by a LO lightwave in the CO. The upstream electrical field at the output of each RRH_{m_n} can be written as

$$E_{A_{m\_n}}(t) = [V_{SU_{m\_n}}(t) + V_{P_{m\_n}}(t)] \cdot e^{j[\omega_{U_{m\_n}}t + \varphi_{U_{m\_n}}(t)]} \quad (4)$$

where $\omega_{U_{m\_n}}$ and $\varphi_{U_{m\_n}}(t)$ denote the frequency and phase of the laser diode LD_{m_n}. At the RN, the outputs of the m^{th} group of RRHs, carried at the same center wavelength λ_m (with moderate frequency offset) yet separated by different IFs, are first optically coupled. The electric field at the output of the coupler is given by $E_{A_m}(t) = \sum_n E_{A_{m\_n}}(t)$. The electrical field of the UL signal after multiplexing all wavelength channels is given by $E_{AU}(t) = \sum_m E_{A_m}(t)$, as per Figure 52(b). The received optical signal at the CO optical receiver Rx_m is sent to the coherent detector with the LO lightwave $E_{LO_m}(t) = e^{j(\omega_{LO_m}t + \varphi_{LO_m}(t))}$, where ω_{LO_m} and φ_{LO_m} are the LO carrier frequency and phase. The electrical currents of the I and Q channels are given by $I_{A_m}(t) = R \cdot Re\left\{\overrightarrow{E_{A_m}}(t) \cdot \overrightarrow{E_{LO_m}}^{*}(t)\right\}$ and $Q_{A_m}(t) = R \cdot \mathrm{Im}\left\{\overrightarrow{E_{A_m}}(t) \cdot \overrightarrow{E_{LO_m}}^{*}(t)\right\}$, respectively, where R denotes photodiode responsivity. Expanding $I_m(t)$ and $Q_m(t)$ yields

$$I_{A_m}(t) = R\sum_n\{\left[V_{SU_{m\_n}}(t) + V_{P_{m\_n}}(t)\right]\cos\left[\omega_{O_{m\_n}}t - \varphi_{m\_n}(t)\right]\} \quad (5)$$

$$Q_{A_m}(t) = R\sum_n\{\left[V_{SU_{m\_n}}(t) + V_{P_{m\_n}}(t)\right]\sin\left[\omega_{O_{m\_n}}t - \varphi_{m\_n}(t)\right]\} \quad (6)$$

where $\omega_{O_{m\_n}} = \omega_{U_{m\_n}} - \omega_{LO_m}$ and $\varphi_{m\_n}(\mathrm{t}) = \varphi_{U_{m\_n}}(t) - \varphi_{LO_m}(t)$ are the frequency offset and phase noise, correspondingly. By combining I and Q, the complex signal can be written as

$$I_{Ar}(t) = R\sum_n\{[V_{SU_{m\_n}}(t) + V_{P_{m\_n}}(t)]e^{j[\omega_{O_{m\_n}}t - \varphi_{m\_n}(t)]}\} \quad (7)$$

The OFDM + pilot pair from RRH_{m_n} is modulated by $e^{j[\omega_{O_{m\_n}}t - \varphi_{m\_n}(t)]}$, whose bandwidth is larger than the LTE subcarrier spacing (15 KHz). With the help of the paired external pilot tone, the OFDM signal on each IF can be retrieved individually after frequency offset estimation and phase noise recovery.

The number of IFs and frequency spacing have been studied for downstream performance [53]. More importantly, to insure signal integrity, the guard band between optically coupled signals needs to be chosen carefully for upstream. With the use of stable and narrow-linewidth ECLs, the proposed DWDM-SCM-PON approach can allow spacing of UL signals to be as small as 100MHz. The spectrum efficiency is significantly improved compared with the CPRI approach. To scale up to multiple antennas, CCs, and sectors in one cell site, received upstream wireless signals are processed together in the IF-RF frontend into a multi-IF composite. One RF pilot tone is paired with the composite before driving the modulator. Instead of one signal term $V_{SU_{m\_n}}(t)$ in (4), a combination of IF signals are included and recovered together by the joint pilot signal. Based on different traffic demands, carrier frequencies of signals and pilot of a cell site can be dynamically assigned in the CO. Therefore, this scheme can be easily scaled to different deployment scenarios supported by coherent detector and DSP.

4.3.2.2 MFH System (2) with UDWDM-Based UL and Phase-Noise-Insensitive Heterodyne Detection

The second MFH system proposed in this section shares the same DL architecture as system (1), i.e., the DWDM-SCM-PON, but differs in modulation and detection techniques for the UL. In order to further explore the feasibility of achieving very high spectrum efficiency while using simple non-coherent detector and cost-effective lasers, an alternative upstream scheme with phase-noise-insensitive reception enabled by heterodyne detection and envelope detection is offered.

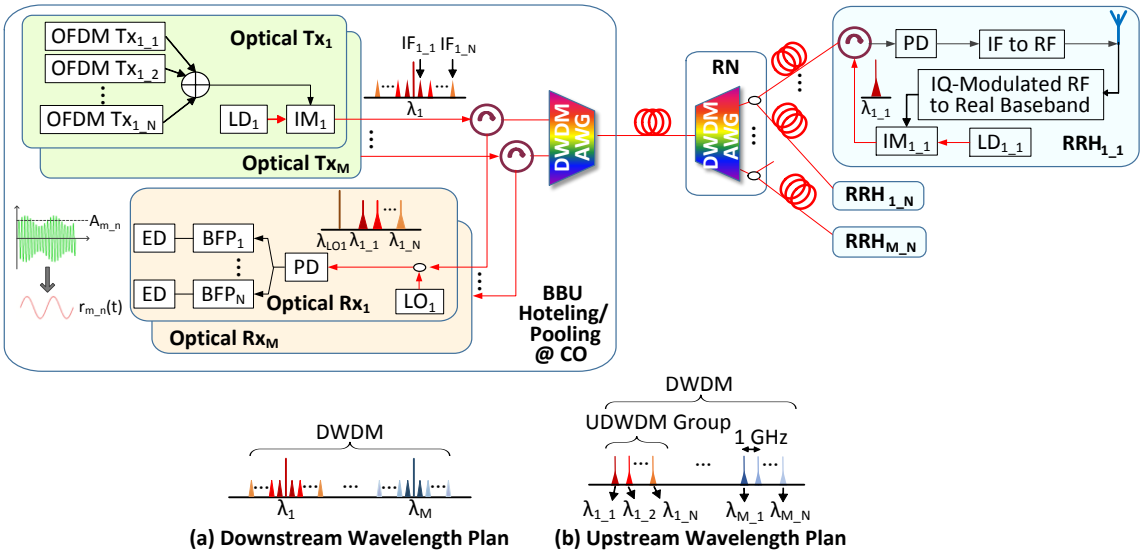

Figure 53. Proposed MFH architecture (2). DL: IFoF-DWDM-PON; UL: UDWDM over DWDM-PON with phase-noise-insensitive heterodyne detection. (a) and (b) Downstream and upstream wavelength plan, respectively.

Figure 53 shows the second MFH architecture. Again, a scenario with single sector, no MIMO or carrier aggregation is investigated first. The DL theoretical analysis is the same as that is described previously in system (1). As for the upstream, in order to enable simple phase-noise-insensitive envelope detection, the received wireless IQ-mixed OFDM

signal centered at the RF is first converted to a real-valued baseband OOK/OFDM signal, $r_{m\_n}(t)$. Figure 54 shows three methods for the conversion. The most straightforward way is to demodulate the received wireless signal to obtain the bit output, which corresponds to a raw data rate of up to 108Mb/s for a 20-MHz 64QAM-OFDM. For better spectral efficiency, the second method remodulates the bit output to a real-valued baseband multiplex based on discrete multitone (DMT), a variation of OFDM widely used in wireline systems [79], by setting the second half of the Inverse Fast-Fourier-Transform (IFFT) points to be the complex conjugate of the first half. Finally, the RF signal can also be downconverted by an image-reject (IR) mixer to an IF such that the left edge of the OFDM signal is very close to zero frequency.

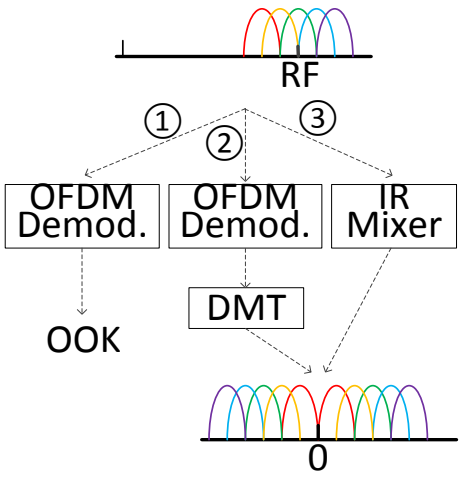

Figure 54. Three conversion methods to real-valued baseband signal.

A laser diode LD_{m_n} generates the lightwave on λ_{m_n} which is sent to an IM driven by the baseband signal. The upstream electrical field at the output of each RRH_{m_n} can be written as

$$E_{B_{m\_n}}(t) = [A_{m\_n} + r_{m\_n}(t)]e^{[j\omega_{m\_n}t+\varphi_{m\_n}(t)]} \quad (8)$$

where A_{m_n} is direct current (DC) term tunable by the bias voltage, ω_{m_n} and $\varphi_{m\_n}(t)$ are the optical source carrier frequency and phase, respectively. The UL wavelengths of the m^{th} RRH group are located closely with gigahertz spacing, all inside the m^{th} pass-band of the AWG, as shown in Figure 53(b). The electric field of the aggregate UL signal of the m^{th} group is given by $E_{B_m}(t) = \sum_n E_{B_{m\_n}}(t)$. Similarly, the electrical field of the multiplexed UL channels by the DWDM AWG in the RN is given by $E_{BU}(t) = \sum_m E_{B_m}(t)$. Following heterodyne detection of the aggregated upstream and an LO light on λ_{LOm} at the CO optical receiver Rx_m, the electrical current at the PD output is given by $I_{B_m}(t) = R \cdot \left|E_{B_m}(t) + E_{LO_m}(t)\right|^2$. Expanding $I_{B_m}(t)$ yields

$$I_{B_m}(t) = R\sum_n\{\left[A_{m\_n} + r_{m\_n}(t)\right]\cos\left[2\pi f_{m\_n}t - \varphi_{m\_n}(t)\right] + a_m(t)\} \quad (9)$$

where $f_{m\_n} = \left|2\pi\ (\omega_{m\_n} - \omega_{LO_m})\right|$ is the frequency difference, $\varphi_{m\_n}(\mathrm{t}) = \varphi_{m\_n}(t) - \varphi_{LO_m}(t)$ is the phase noise, and $a_m(t)$ includes self-beating terms of $E_{B_m}(t)$ signal. The signal at f_{m_n} is selected by a BPF, and its envelope information, i.e. $r_{m\_n}(t)$, is retrieved by an ED (Figure 53). All unwanted high-frequency *cos( )* terms in (9) containing laser phase noise are removed.

For a few sectors, MIMO, and carrier aggregation deployment, received upstream wireless signals can be converted jointly to a real-valued baseband signal. However, the first conversion method would produce relatively large OOK data rate for an advanced deployment scenario, and the third method would require multiple RF components. The second method is comparatively capable for upgrading since it digitally combines signals into a DMT signal. However, the bandwidth of the new DMT signal is subject to the

bandwidth of the ED. Consequently, this scheme is more suitable for small, low-power femtocells and picocells. Nonetheless, compared with the MFH system (1), due to the phase-noise-insensitive feature of this detection scheme, lasers in BBU and RRH can be inexpensive MHz-linewidth lasers rather than ECLs. The required frequency stability of the laser is relaxed as well, since the fluctuation only needs to be controlled within the bandwidth of the BPF. The wavelength spacing of the UDWDM group in the system (2) is in the gigahertz range, as illustrated in Figure 53. The limitation of the wavelength spacing is discussed in detail along with the experimental demonstration next. With the proposed UDWDM and simple detection scheme, high spectral efficiency is enabled, DSP-based compensation is not needed, and both BBU and RRH are cost-effective.

4.3.3 Experimental Setups and Results

Since two proposed architectures have the same SCM-based DL structure that has been elaborated in Chapter 4 Section 2, a series of experiments is conducted for the SCM-based UL, and UDWDM-based UL, respectively, to verify the feasibility of the proposed resource sharing in fronthaul upstream transmissions.

4.3.3.1 MFH System (1) Verification

Figure 55 shows the experimental setup of the first UL design based on SCM and coherent detection. Due to the lack of additional ECLs, one ECL is split to serve as the lightwave source for each RRH in this experiment, and modulated with the corresponding paired OFDM + pilot tone generated by a 1-GSa/s arbitrary waveform generator. The four IFs of the upstream OFDM signals are IF_1 = 75 MHz, IF_2 = 175 MHz, IF_3 = 275 MHz, and IF_4 = 375 MHz. The OFDM signal features bandwidth of 20 MHz, FFT size of 512 (limited by

the number of oscilloscope sampling points, the FFT size is not chosen to be 2048 as defined in the LTE standard), with 16-QAM symbol mapping, 384 data-bearing subcarriers, and 128-samplle cyclic prefix. The pilot tones at P_1 = 125 MHz, P_2 = 225 MHz, P_3 = 325 MHz, and P_4 = 425 MHz are placed in between the OFDM carriers. Figure 56 illustrates the EVM of the UL OFDM signal with respect to the pilot-to-data power ratio (PDR). In the lower PDR region, the interference signal $e^{j[\omega_{O_{m\_n}}t-\varphi_{m\_n}(t)]}$ retrieved from the pilot tone has low signal-to-noise ratio (SNR), and thus affects the recovery of the OFDM signal. On the other hand, in the high PDR region, the original OFDM has small signal power and results in high EVM as well. It is observed that PDR = 4.4 dB gives the optimum performance, and this is applied in the following measurements. Due to hardware limitation, the OFDM and pilot signals from RRH_1 and RRH_3 are generated together and modulated by the IM_1 biased at the null point, while the signals from RRH_2 and RRH_4 drive the IM_2. The outputs of both IMs, each at -8dBm power, are optical coupled at the RN. After 20-km fiber transmission (Figure 55(a)), the received signal is amplified by an EDFA (Figure 55(b)) and sent to the coherent receiver together with the same LD serving as a LO. Figure 55(c) shows the received UL signal in the BTB case where no frequency offset and slow-change phase noise are presented. For the 20-km fiber propagation case, the combined two lightwaves remain coherent with each other but incoherent with the LO, resulting in the same frequency shift and fast-change phase noise to four OFDM + pilot pairs. To further decorrelate the signals and the LO, a 20-km SSMF is added between the RN and the $RRH_{1,3}$, and an attenuator is applied to the $RRH_{2,4}$ to match the fiber loss. As shown in Figure 55(d), signals from $RRH_{1,3}$ and $RRH_{2,4}$ exhibit independent frequency offset and phase noise, and require estimation from corresponding pilot tone.

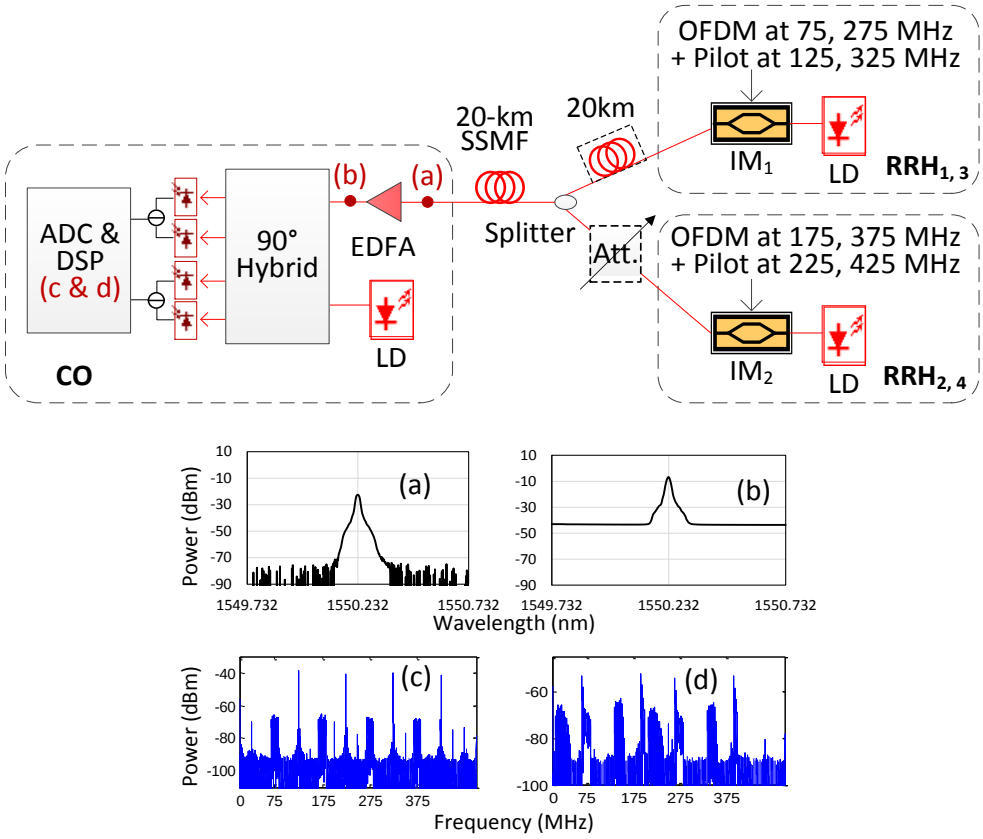

Figure 55. Experimental setup of the IFoF-based MFH UL. (a) and (b) Optical spectra (0.01nm resolution) measured at point a and b. (c) and (d) Electrical spectra obtained after the ADC and DSP for 20-km transmission and 20/40-km transmission cases.

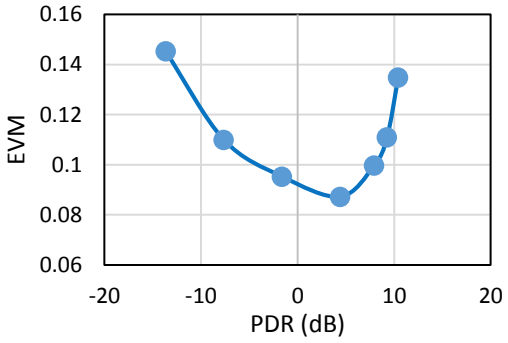

Figure 56. EVM of the UL OFDM signal with respect to PDR.

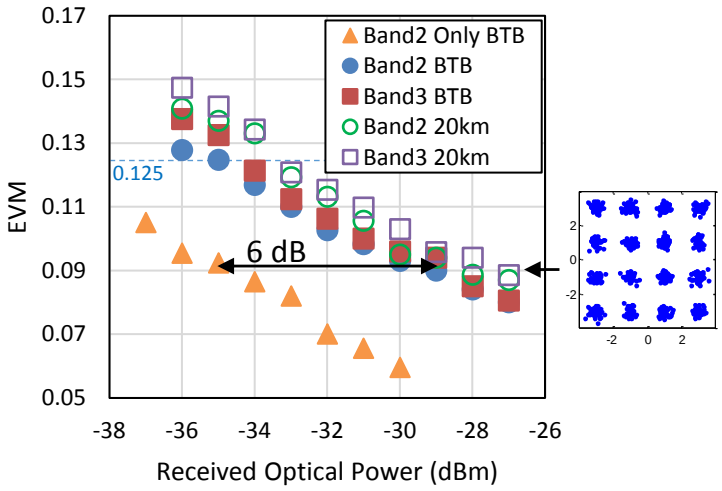

Figure 57. EVM for the UL OFDM signal in BTB and 20-km SSMF cases.

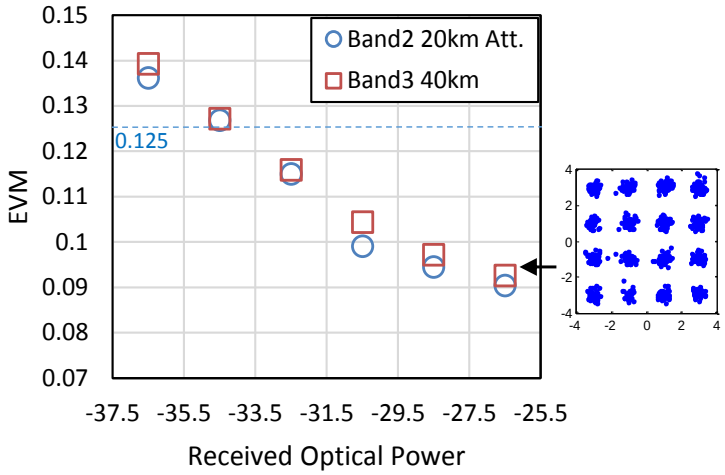

Figure 58. EVM for the received UL OFDM signal from RRH_2 after 20-km fiber and signal from RRH_3 after 40-km fiber.

Figure 57 shows the EVM for the UL OFDM signals at IF_2 and IF_3. Receiver sensitivity of -34 dBm is achieved at EVM = 0.125, corresponding to a 26-dB UL power budget. A single-band OFDM signal carried at IF_2 only is also transmitted through the system and measured as orange triangles in Figure 57 indicate. About 6-dB received optical power difference between single-IF and 4-IF cases is observed, matching the theoretical 6-

dB ($10\log_{10}4$) difference and indicating negligible power penalty due to multiple carriers. Compared to BTB case, the received signal and LO are no longer coherent in the 20-km transmission case, introducing random frequency offset and phase noise. It accounts for a 1.5-dB power penalty. The OFDM signal at IF_3 exhibits slightly worse performance than the signal at IF_2 due to the small sample rate (1 GSa/s). Figure 58 illustrates the EVM measurements for the received UL OFDM signal at IF_2 after 20-km fiber and the signal at IF_3 after 40-km fiber link, respectively. Similar performances are achieved comparing with transmission results over 20-km fiber in Figure 57, illustrating successful recovery of the frequency offset and phase noise based on pilot tones from different RRHs. Therefore, with coherent receiver, the ultra-tight spectrum allocation with channel spacing as small as 100 MHz is maintained for the upstream, while high UL power budget is achieved in this proposed MFH architecture.

4.3.3.2 MFH System (2) Verification

The experimental setup of the second UL design based on UDWDM and phase-noise-insensitive heterodyne detection is shown in Figure 59. Continuous wave optical signals are generated by two AOC ATLS7600 tunable lasers at λ_1 = 1553.739 nm and λ_2 = 1553.747 nm (1-GHz spacing). The lasers have 3-dB linewidth of 5 MHz and fine-frequency tuning resolution of 100 MHz. Two independent 100/200Mb/s OOK or 200Mb/s OFDM signals drive the two 10-GHz IMs, which are biased properly so that the DC bias voltage A_{m_n} in (9) is about half of the signal V_{pp}. The signal bandwidth is limited by the ADL5511 ED (a chip on an evaluation board) used in the experiment. The chip is typically deployed in 2G and 3G base stations and has 130-MHz envelop bandwidth. The real-valued baseband OFDM signal based on DMT is generated by a 1-GSa/s arbitrary waveform

generator, and featured FFT size of 512, with 16-QAM symbol mapping, 64 data-bearing subcarriers. Next, the two outputs are optically combined and launched over the 30-km SSMF link. Following fiber transmission, the joint signal is heterodyne detected by a 10-GHz PD with another LO laser at 6 dBm and λ_{LO} = 1553.719 nm. The optical spectra of the received signal (about -30 dBm), LO, and the combined signal + LO are illustrated in Figure 59(a). Figure 59(b) depicts the electrical spectra of the signals from the beating between λ_1 and λ_{LO} with and without modulating the data. The two RF curves centered at f_1 = 2.5 GHz show negligible difference, which indicates the broad spectrum is mainly due to the random fluctuations in the phase of two lasers. In order to study the spectral efficiency limits of the proposed architecture, λ_2 is tuned from 1553.743 nm to 1553.751 nm to produce a second neighboring RF signal centered at the following frequencies: f_2 = 3 GHz, f_3 = 3.3 GHz, f_4 = 3.5 GHz, and f_5 = 4 GHz, as shown in Figure 59(c). A real-time oscilloscope is used to digitize the two closely-located OFDM signals due to the lack of a narrow BPF. The offline processing in Matlab includes a digital BPF with 600MHz bandwidth, a Hilbert transform, and an OFDM demodulation.

Figure 60 shows the EVM for the OFDM signal at f_1 with respect to its received optical power. Compared with optical BTB case, the 30-km fiber transmission induces negligible power penalty. It is observed that 1-GHz channel spacing ($f_1 + f_4$) introduces no EVM degradation, while 0.8-GHz ($f_1 + f_3$) and 0.5-GHz ($f_1 + f_2$) spacings introduce 1% and 4% EVM increases, respectively, mainly due to the spectral overlapping which can be clearly observed in Figure 59(c).

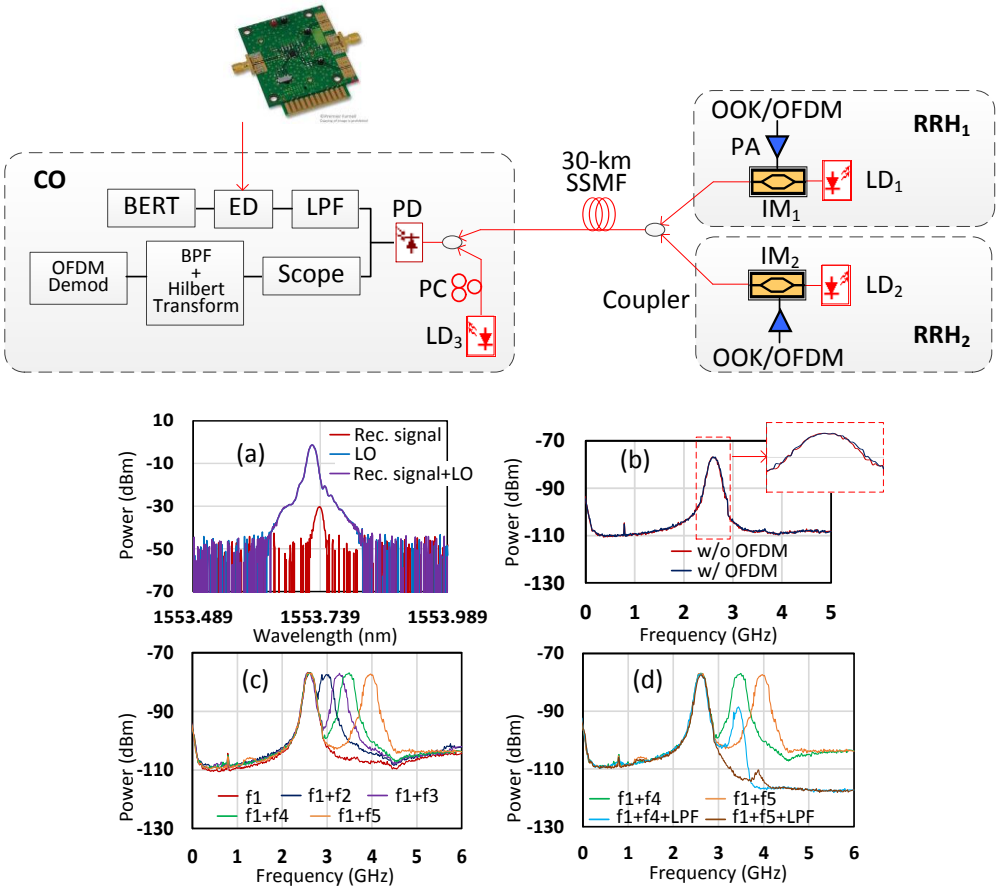

Figure 59. Experimental setup of the UDWDM-based MFH upstream. (a) Optical spectrum (0.01nm resolution) of the received signal and the LO. (b)-(d) Electrical spectra measured after the PD. f_1 = 2.5 GHz, f_2 = 3 GHz, f_3 = 3.3 GHz, f_4 = 3.5 GHz, f_5 = 4 GHz.

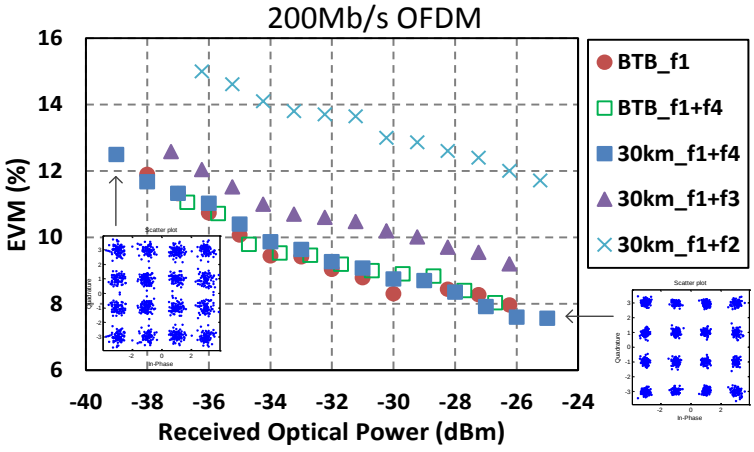

Figure 60. EVM for the OFDM signal at f_1. Constellations at EVM = 7.5% and 12.5% are inserted.

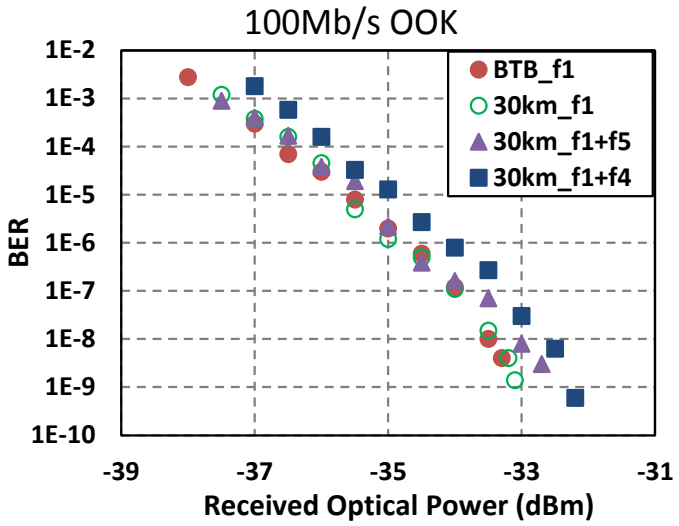

Figure 61. BER for the 100-Mb/s OOK signal.

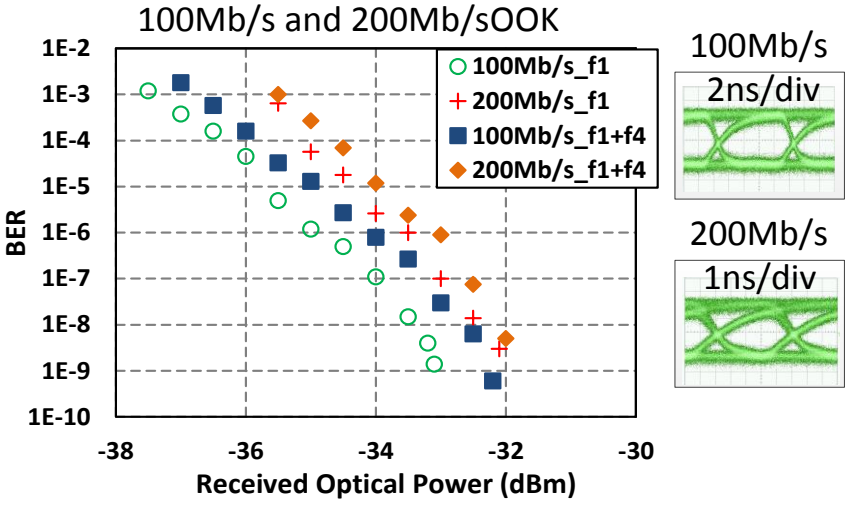

Figure 62. BER for the 200-Mb/s OOK signal at f_1 with eye diagrams inserted.

To measure the OOK performance, a 3-GHz LPF is used prior to the ADL5511 ED. As shown in Figure 59(d), the LPF, unlike the digital filter with narrow roll-off, is able to remove part of the signal at f_3 and the majority of the signal at f_4. The BER for the OOK data is measured by a BERT. Figure 61 illustrates the BER for the 100-Mb/s OOK signal

at f_1. The bandwidth of a 100Mb/s-OOK-modulated RF signal is 200 MHz, which exceeds the ED bandwidth by 70 MHz. Nonetheless, error-free transmission is achieved at about -33 dBm, indicating high-quality performance as well as high receiver sensitivity attained by the proposed phase-noise-insensitive heterodyne detection scheme. Similar to the OFDM results, the 30-km fiber propagation introduces negligible power penalty. The residual neighboring channel at f_4 after the low-pass filtering degrades the integrity of the envelope and results in around 0.8-dB power penalty. By separating the two channels further to 1.5 GHz, similar BER performance (as indicated by purple triangles in Figure 61) is again achieved compared with the single-channel case (as indicated by green circles in Figure 61). Moreover, data rate is then increased to 200 Mb/s. Figure 62 shows the BER for the 200-Mb/s OOK, where a power penalty of 1 dB is observed due to the data rate increase. Clear eye diagrams for the two data rates are inserted in Figure 62. The overall experiment results demonstrate high achievable performances of the proposed UDWDM-PON MFH upstream using MHz-linewidth lasers and commercially available envelope detector.

4.4 Summary

In this chapter, limitations of the CPRI approach, especially for 4^+G cell sites with the full deployment of 3 RRHs (3-sectors), 5 aggregated 20-MHz carriers (100-MHz bandwidth), and 8×8 MIMO, have been addressed. To improve spectral efficiency and reduce requirements on optical transceivers and wavelength resources, DWDM-SCM-PONs using conventional AWGs and CAWGs + R/B WDMs have been presented to fully support the highest standard. With 60 IFs closely multiplexed on one wavelength, significant reduction in the requirements on both the number of wavelengths per cell site and the optical

bandwidth of the optical transceivers has been achieved. Successful transmissions of 12 × 100-MHz LTE-A-like signals over 20-km fiber based on direct modulation and over 40-km fiber using external modulation with complete RF signal processing have been experimentally demonstrated. In addition, simultaneous transmission of a real-time Wi-Fi channel with 11 CA-signals in an end-to-end MFH system testbed has been demonstrated. Receiver sensitivity of -10 dBm has been consistently achieved for low EVM of ~4%, with no RRH-side optical amplification. Next, to further increase the wavelength utilization and enable flex-grid wavelength allocation, two schemes have been proposed, where multiple cell sites are able to share one DWDM-PON. DWDM-SCM-PON architecture is again adopted for the DL. The key technical innovations of the two schemes are novel upstream designs that enable ultra-small channel spacing, dynamic spectral allocation, high order modulation format, and thus high spectral efficiency. The first proposed UL approach is based on IF-modulation in RRHs and coherent detection in BBUs. It can allow IF spacing to be as small as 100 MHz and easily scale up to maximum LTE-A configuration. UL transmission of four 20-MHz 16QAM-OFDM LTE-like signals with 100-MHz spacing aggregated on one wavelength has been demonstrated. For the second proposed UL scheme, a low-complexity UDWDM over DWDM allocation with 1-GHz wavelength spacing and phase-noise-insensitive heterodyne detection has been reported. It is a cost-effective fronthaul solution for high-density femtocell and picocell deployment. Experimental demonstration of the transmission and simple detection of multi-channel 100/200Mb/s OOK or 200Mb/s 16QAM-OFDM signals with 1-GHz wavelength spacing over 30km SSMF using 5MHz-linewidth lasers and an off-the-shelf envelope detector has been presented. By enabling ultra-high spectral efficiency, high receiver sensitivity, and low-

complexity, the proposed approaches achieve a significant breakthrough for future high-capacity mobile fronthaul systems.

CHAPTER 5

CONCLUSIONS

5.1 Contributions

This dissertation makes several key contributions to the body of knowledge on integrated optical-wireless communication systems. It has been shown that the overwhelming explosion of the data traffic demand is fundamentally changing the wireless network and its wired counterpart. While wireless systems are constantly evolving to the newer generation and higher capacity, their supporting wired networks urgently require advancements in both architecture and enabling technologies. New optical systems especially tailored for the unique natures of various wireless standards are of necessity investigated. Thus, the objective of the research was to design and experimentally verify high-capacity communication systems using advanced integrated electrical and optical technologies. The main contributions of this dissertation are summarized below:

- From the service aspect, gigabit mm-wave services provided by RoF systems have been demonstrated with the co-existence of legacy microwave services. Two practical and efficient schemes - all-band RoF and band-mapped 60-GHz RoF – have been proposed to cover distinct application scenarios. The delivery of independent Wi-Fi, WiMAX and 60-GHz mm-wave signals over 30-km SSMF in the all-band RoF system has been experimentally evaluated. A real-time

demonstration of converged TV, Wi-Fi and OOK data, compactly mapped into 60-GHz sub-bands in the band-mapped RoF system, has also been reported.

- Advanced optical MBH architectures and synchronization schemes have been presented. First, synchronous clock distribution and recovery for high-capacity DWDM-OFDMA-based MBH featuring IMDD and DSP-free electrical filtering have been proposed. 50-MHz square clock and 4/5-GHz sinusoidal clocks have been experimentally distributed and recovered with aggregate 41.09/51.31-Gb/s DWDM-OFDMA data transmission over 40-km SSMF and 25-GHz channel spacing. Second, a low-complexity synchronous clock distribution and recovery method for coherent UDWDM-OFDMA-based mobile backhaul featuring optical SSB modulation and envelope detection has been introduced. Experimental verification of 30-Gb/s aggregate data rates with 50-MHz clock distribution in 24.56-GHz total spectrum over 40-km SSMF has been demonstrated with simple envelope-detection-based clock recovery.

- Limitations of current MFH solutions have been addressed, especially considering 4^{+}G cell sites with the full deployment of 3 RRHs (3-sectors), 5 aggregated 20-MHz carriers, and 8×8 MIMO. DWDM-SCM-PONs using conventional AWGs and using CAWGs + R/B WDMs have been presented to meet such requirements while improving spectral efficiency and reducing requirements on optical transceivers and wavelength resources. Successful transmissions of 12 × 100-MHz LTE-A-like signals over 20-km fiber based on direct modulation and over 40-km fiber using external modulation with complete RF signal processing have been experimentally demonstrated. Low-latency feature and feasibility of the proposed

scheme have been validated by the simultaneous transmission of a real-time Wi-Fi channel with 11 CA-signals in an end-to-end MFH system testbed. To further increase spectrum utilization and enable flex-grid wavelength allocation, two schemes with key technical innovations for ULs have been proposed with different wavelength sharing techniques. The first proposed UL approach is based on IF-modulation in RRHs and coherent detection in BBUs that allows maximum LTE-A configuration and IF spacing to be as small as 100 MHz. UL transmission of four 20-MHz 16QAM-OFDM LTE-like signals along with novel RF pilot tones aggregated on one wavelength with narrow 100-MHz spacing has been demonstrated. For the second proposed UL scheme, a low-complexity UDWDM over DWDM allocation with 1-GHz wavelength spacing and phase-noise-insensitive heterodyne detection has been proposed as a cost-effective fronthaul solution for high-density femtocell and picocell deployment. Experimental demonstration of the transmission and simple detection of multi-channel 100/200Mb/s OOK or 200Mb/s 16QAM-OFDM signals with 1-GHz wavelength spacing over 30km SSMF using 5MHz-linewidth lasers and an off-the-shelf envelope detector has been presented.

5.2 Future Research Topics

The following is a list of interesting research topics that can be pursued as an extension of this dissertation:

- The research of seamless integration of WDM-PON systems with wireless systems can be continued. One of the important topics is PON resilience. Some applications

such as wireless backhaul and fronthaul require different levels of network protection or restoration. Therefore, protection architectures can be designed for MBH and MFH systems that have been presented in this dissertation. The proper tradeoff between cost and resilience performance can be studied based on individual application requirements.

- The biggest concern in the use of RoF links in the MFH is their limited dynamic range due to nonlinear distortion, which is mainly induced by the nonlinearity in the optical transmitter and fiber. In addition, the high-power PA is also a nonlinear component that usually requires linearization. Since RoF-based MFH shifts signal processing in the BBU, the nonlinearity introduced by the RoF links and the RF amplifier must be compensated centrally. Therefore, pre-distortion schemes in the BBU to compensate the above-mentioned nonlinearities in the RoF MFH are worth investigating. Previous observation and analysis on multi-channel cross-modulation induced by the MZM can be extended to a more encompassing and systematic scope.

- The study of the co-existence of licensed and unlicensed bands, for example, LTE-A and Wi-Fi, would be an interesting topic. Specifically, issues on how the co-existing services may affect each other in terms of signal quality, coverage range, air-time fairness, and effective throughput can be investigated.

- Research on advanced modulation formats can be continuously conducted. Besides QAM and OFDM modulation formats, carrier-less amplitude and phase (CAP) modulation can be applied to the low-complexity IMDD links. It allows relatively

high data rate achieved by electrical and optical components of limited bandwidth, and thus fits in the optical-wireless access network applications.

REFERENCES

[1] D. J. Richardon, J. M. Fini, and L. E. Nelson, "Space-division multiplexing in optical fibres," *Nature Photonics*, vol. 7, pp. 354–362, Apr. 2013.

[2] CISCO VNI, Global Mobile Data Traffic Forecast Update, 2013-2018 Feb. 2014 [Online]. Available: www.cisco.com.

[3] "Wireless LAN medium access control (MAC) and physical layer (PHY) specifications," *IEEE Std 802.11-2012*, pp. 1–2793, Mar. 2012.

[4] "IEEE standard for air interface for broadband wireless access systems," *IEEE Std 802.16-2012 (Revision of IEEE Std 802.16-2009)*, pp. 1–2542, Aug. 2012.

[5] "3rd Generation Partnership Project (3GPP); Technical Specification Group Radio Access Network; Physical layer aspects for evolved Universal Terrestrial Radio Access (UTRA) (Release 7)," *3GPP TR 25.814, V7.1.0*, Sept. 2006.

[6] 3GPP Technical Report 36.912, "Feasibility study for Further Advancements for E-UTRA (LTE-Advanced)", Version 12.0.0, Sept. 2014, Available at www.3gpp.org

[7] T.S. Rappaport, J.N. Murdock, and F. Gutierrez, "State of the Art in 60-GHz Integrated Circuits and Systems for Wireless Communications," *Proceedings of the IEEE*, vol. 99, no. 8, pp. 1390 – 1436, Aug. 2011.

[8] P. Briggs, R. Chundury, and J. Olsson, "Carrier Ethernet for mobile backhaul," *IEEE Commun. Mag.*, vol. 48, no. 10, pp. 94-100, Oct. 2010.

[9] P. Chanclou et. al., "Optical fiber solution for mobile fronthaul to achieve cloud radio access network," *Future Network and Mobile Summit 2013*, pp. 1-11.

[10] Infonetics Research, "Macrocell Mobile Backhaul Equipment and Services: Biannual Market Size, Share and Forecasts," Oct. 2014.

[11] F. Giannetti, M. Luise, and R. Reggiannini, "Mobile and personal communications in 60 GHz band: A survey," *Wirelesss Pers. Comun.*, vol. 10, no. 2, pp. 207–243, 1999.

[12] "WirelessHD Specification Version 1.1 Overview," WirelessHD Std. Overview, May 2010, [Online] Available: http://www.wirelesshd.org/pdfs/WirelessHD-Specification-Overview-v1.1May2010.pdf

[13] IEEE Std 802.15.3c-2009 (Amendment to IEEE Std 802.15.3-2003), Oct. 12, 2009.

[14] ECMA International, "High Rate 60 GHz PHY, MAC and HDMI PALs," Standard ECMA-387, 2nd Edition, Dec. 2010. [Online] Available: http://www.ecma-international.org/publications/files/ECMA-ST/ECMA-387.pdf

[15] M. Sauer, A. Kobyakov, and J. George, "Radio over fiber for picocellular network architectures," *J. of Lightw. Technol.*, vol. 25, no. 11, pp. 3301–3320, Nov. 2007.

[16] C. H. Cox, III, G. E. Betts, and L. M. Johnson, "An analytic and experimental comparison of direct and external modulation in analog fiber-optic links," *IEEE Trans. Microw. Theory Tech.*, vol. 38, no. 5, pp. 501–509, May 1990.

[17] Z. Jia, J. Yu, and G.-K. Chang, "All-optical 16 ×2.5 Gb/s WDM signals simultaneous up-conversion based on XPM in an NOLM in RoF systems," *IEEE Photon. Technol. Lett*, vol. 17, no. 12, pp. 2724-2726, 2005.

[18] J. Liu, H.-C. Chien, S.-H. Fan, B. Chen, J. Yu, S. He, G.-K. Chang, "Efficient optical millimeter-wave generation using a frequency-tripling Fabry–Pérot laser with sideband injection and synchronization," *IEEE Photon. Technol. Lett*., vol. 23, no. 18, pp. 1325-1327, 2011.

[19] Z. Jia, J. Yu, G. Ellinas, and G.-K. Chang, "Key Enabling Technologies for Optical–Wireless Networks: Optical Millimeter-Wave Generation, Wavelength Reuse, and Architecture," *J. Lightw. Technol.*, vol.25, no.11, pp.3452-3471, Nov. 2007.

[20] C.-T. Lin, S.-P. Dai, J. Chen, P. T. Shih, P.-C. Peng, and S. Chi," A novel direct detection microwave photonic vector modulation scheme for radio-over-fiber system," *IEEE Photon. Technol. Lett*., vol. 20, no. 13, pp. 1106-1108, July 2008.

[21] P.-T. Shih, C.-T. Lin, H.-S. Huang, W.-J. Jiang, J. Chen, A. Ng'oma, M. Sauer, and S. Chi, "13.75-Gb/s OFDM signal generation for 60-GHz RoF system within 7-GHz license-free band via frequency sextupling," *Proc. ECOC 2009*, paper 4.5.4.

[22] G. Qi, J. Yao, J. Seregelyi, S. Paquet, and C. Bélisle, "Optical generation and distribution of continuously tunable millimeter-wave signals using an optical phase modulator," *J. Lightw. Technol.*, vol. 23, no. 9, pp. 2687–2695, Sep. 2005.

[23] AT&T U-verse, http://uverse.com

[24] Cable Television Laboratories, Inc., Data-over-cable Service Interface Specifications DOCSIS 3.1, MAC and Upper Layer Protocols Interface Specification, March, 2014.

[25] O. Omomukuyo, M.P. Thakur, and J.E. Mitchell, "Experimental performance analysis of MB-OFDM Ultra-Wideband Radio-Over-Fiber signals in the 60-GHz band using a commercially-available DFB laser," *Proc. ICTON 2012*, paper Mo.C3.4.

[26] Y.-T. Hsueh, C. Liu, S.-H. Fan, J. Yu, and G.-K. Chang, "A novel full-duplex testbed demonstration of converged all-band 60-GHz radio-over-fiber access architecture," *Proc. OFC/NFOEC 2012*, paper OTu2H.5.

[27] A. Chowdhury, H.-C. Chien, S.-H. Fan, J. Yu, and G.-K. Chang, "Multi-Band Transport Technologies for In-Building Host-Neutral Wireless Over Fiber Access Systems," *J. Lightw. Technol.*, vol.28, no.16, pp.2406-2415, Aug.15, 2010.

[28] H. Li, J. Hajipour, A. Attar, and V.C.M. Leung, "Efficient HetNet implementation using broadband wireless access with fiber-connected massively distributed antennas architecture," *IEEE Trans. Wireless Commun.*, vol.18, no.3, pp.72-78, Jun. 2011.

[29] Y.-T. Hsueh, Z. Jia, H.-C. Chien, A. Chowdhury, J. Yu, and G.-K.. Chang, "Generation and transport of independent 2.4 GHz (Wi-Fi), 5.8 GHz (WiMAX), and 60-GHz optical millimeter-wave signals on a single wavelength for converged wireless over fiber access networks," *Proc. OFC/NFOEC 2009*, paper OTuJ1.

[30] B. Mukherjee, "WDM optical communication networks: progress and challenges," *IEEE J. Selected Areas Commun.*, vol. 18, no. 10, pp. 1810-1824, Oct. 2000.

[31] Y.-T. Hsueh, M.-F. Huang, S.-H. Fan, and G.-K. Chang, "A novel lightwave centralized bidirectional hybrid access network: seamless integration of RoF with WDM-OFDM-PON," *IEEE Photon. Technol. Lett*., vol.23, no.15, pp.1085, 1087, Aug.1, 2011.

[32] W. Ji and J. Chang, "Design of WDM-RoF-PON for wireless and wire-line access with source-free ONUs," Design of WDM-RoF-PON for wireless and wire-line access with source-free ONUs," *J. Opt. Commun. Netw.*, vol.5, no.2, pp.127-133, Feb. 2013.

[33] I. G. Insua, D. Plettemeier, and C. G. Schaffer, "Simple Remote Heterodyne Radio-Over-Fiber System for Gigabit Per Second Wireless Access," *J. of Lightw. Technol*., vol.28, no.16, pp.2289, 2295, Aug.15, 2010.

[34] ITU-T Recommendation G.694.2, "Spectral grids for WDM applications: CWDM wavelength grid", Dec. 2003.

[35] ITU-T Recommendation G.694.1, "Spectral grids for WDM applications: DWDM frequency grid", Feb. 2012.

[36] S. Smolorz, H. Rohde, E. Gottwald, D. W. Smith, and A. Poustie, "Demonstration of a Coherent UDWDM-PON with Real-Time Processing," *Proc. OFC/NFOEC 2011*, paper PDPD4.

[37] R. Dischler, and F. Buchali, "Transmission of 1.2Tb/s continuous waveband PDM-OFDM-FDM signal with spectral efficiency of 3.3bit/s/Hz over 400km of SSMF," *Proc. OFC/NFOEC 2009*, paper PDPC2.

[38] O. Tipmongkolsilp, S. Zaghloul, and A. Jukan, "The evolution of cellular backhaul technologies: Current issues and future trends," *IEEE Commun. Surveys Tuts*., vol. 13, no. 1, pp. 97–113, First Quart, 2011.

[39] A. Magee, "Synchronization in next-generation mobile backhaul networks," *IEEE Commun. Mag*., vol. 48, no. 10, pp. 110–116, Oct. 2010.

[40] M. Gilson and S. Taylor, "Hybrid Mode Synchronous Ethernet & IEEE-1588 in Wireless TDD Applicationa," *NIST WSTS*, Mar. 2010.

[41] N. Cvijetic, A. Tanaka, Y.-K. Huang, M. Cvijetic, E. Ip, Y. Shao, and T. Wang, "4^{+}G mobile backhaul over OFDMA/TDMA-PON to 200 cell sites per fiber with 10Gb/s upstream burst-mode operation enabling < 1ms transmission latency," *Proc. OFC 2012*, paper PDP5B.7.

[42] N. Cvijetic, "OFDM for Next-Generation Optical Access Networks," *J. Lightwave Technol.*, vol. 30, no. 4, pp. 384–398, Feb. 2012.

[43] R. P. Giddings, and J. M. Tang, "Experimental demonstration and optimisation of a synchronous clock recovery technique for real-time end-to-end optical OFDM transmission at 11.25 Gb/s over 25km SSMF,' *Optics Express*, vol. 19, no. 3, pp. 2831-2845, Jan. 2011.

[44] Z. Cao, F. Li, C. M. Okonkwo, H. P. A. van den Boom, E. Tangdiongga, Q. Tang, J. Tang, J. Yu, L. Chen, and A. M. J. Koonen, "A Synchronized Signaling Insertion and Detection Scheme for Reconfigurable Optical OFDM Access Networks," *J. Lightwave Technol.*, vol. 30, no. 24, pp. 3972–3979, Jul. 2012.

[45] P. Laurencio and M.C.R. Medeiros, "Dynamic range of optical links employing optical single side-band modulation," *IEEE Photon. Technol. Lett.*, vol. 15, pp. 748–750, May 2003.

[46] China Mobile, "C-RAN: the road towards green RAN," White Paper, ver. 2, 2011.

[47] J. Wannstrom, "LTE-advanced." Third Generation Partnership Project (3GPP), May 2012.

[48] CPRI Specification V6.0 (2013-8-30). [Online]. Available: http://www.cpri.info/spec.html

[49] B. Guo, W. Cao, and A. Tao, "CPRI compression transport for LTE and LTE-A signal in C-RAN," *CHINACOM 2012*, pp.843-849.

[50] S. Nanba and A. Agata, "A new IQ data compression scheme for front-haul link in Centralized RAN," *PIMRC Workshops 2013*, pp. 210-214.

[51] Z. Shen, A. Papasakellariou, J. Montojo, D. Gerstenberger, and F. Xu, "Overview of 3GPP LTE-Advanced Carrier Aggregation for 4G Wireless Communications," *IEEE Commun. Mag*., vol. 50, no. 2, pp. 122–130, Feb. 2012.

[52] D. Wake, A. Nkansah, and N.J. Gomes, "Radio Over Fiber Link Design for Next Generation Wireless Systems," *J. Lightwave Technol.*, vol. 28, no. 16, pp. 2456-2464, Aug. 2010.

[53] S.-H. Cho, H. Park, H.-S. Chung, K.-H. Doo, S. Lee, and J.-H. Lee, "Cost-effective Next Generation Mobile Fronthaul Architecture with Multi-IF Carrier Transmission Scheme," *Proc. OFC 2014*, paper Tu2B.6.

[54] M. Morant, R. Llorente, and J. Prat, "LTE-advanced carrier aggregation supporting fully standard 3GPP MIMO by optical polarization multiplexing *Proc. OFC 2014*, paper M3D.2.

[55] C. Kottke, K. Habel, M. Eiselt, H. Griesser, and J. P. Elbers, "Coherent Subcarrier-WDM-PON System with SSB Modulation and Wavelength Reuse," *Proc. OFC 2013*, paper OM2A.3.

[56] C. Ruprecht, Y. Chen, D. Fritzche, J. Hoyningen-Huene, N. Hanik, E. Weis, D. Breuer, and W. Rosenkranz, "37.5-km Urban Field Trial of OFDMA-PON using Colorless ONUs with Dynamic Bandwidth Allocation and TCM," *Proc. OFC 2014*, paper Th3G.5.

[57] "Enhancements for Very High Throughput for Operation in Bands below 6 GHz," *IEEE Std 802.11ac-2013*, pp. 1425, Dec. 18 2013.

[58] Open Base Station Architecture Initiative; BTS System Reference Document 2006, V2.0 [Online]. Available: www.obsai.com.

[59] F. Carvalho and A. Cartaxo, "Study on Electrical Power Distribution Among Coexisting OFDM-Based Wired-Wireless Signals Along Long-Reach Passive Optical Networks", *J. Opt. Commun. Netw.*, vol.5, no.2, pp.813-824, Jul. 2013.

[60] Iperf, [Online] Available: http://iperf.sourceforge.net/

[61] B. L. Dang and I. Niemegeers, "Analysis of IEEE 802.11 in Radio over Fiber Home Networks," in *Proc. IEEE Conf. on Local Comp. Net.*, Nov. 2005, pp. 744-747.

[62] J. Wang, C. Liu, M. Zhu, A. Yi, and G.-K. Chang, "Investigation of Intra/Inter-Band Cross-Modulation in Multi-Band Radio-over-Fiber Systems," in *CLEO 2013*, San Jose, CA, paper CM3G.5.

[63] N. Cvijetic, A. Tanaka, P. N. Ji, S. Murakami, K. Sethuraman, and T. Wang, "First OpenFlow-based software-defined λ-flow architecture for flex-grid OFDMA mobile backhaul over passive optical networks with filterless direct detection ONUs," *OFC/NFOEC 2013*, Paper PDP5B.2.

[64] A. Tanaka, N. Cvijetic, T. Wang, "Beyond 5dB Nonlinear Raman Crosstalk Reduction via PSD Control of 10Gb/s OOK in RF-Video Coexistence Scenarios for Next-Generation PON," *Proc. OFC 2014*, Paper M3I.3.

[65] G. Yazawa, N. Yuki, J. Terada, S. Kimura, and N. Yoshimoto, "High accurately synchronized λ-tunable WDM/TDM-PON using timestamps based time and frequency synchronization for mobile backhaul," *OFC/NFOEC 2013*, Paper JTh2A.06.

[66] S. Bregni, "Measurement of maximum time interval error for telecommunications clock stability characterization," *IEEE Trans. Instrum. Meas.*, vol. 45, no. 5, pp. 900–906, 1996.

[67] K. Werner, H. Asplund, B. Halvarsson, N. Jalden, and D. Figueiredo, "LTE-A Field Measurements: 8x8 MIMO and Carrier Aggregation," *Proc. IEEE Veh. Technol. Conf. (VTC'13 Spring)*, Jun. 2013.

[68] IEEE Std 802.3™-2005: "Part 3: Carrier sense multiple access with collision detection (CSMA/CD) access method and physical layer specifications," Dec. 2005.

[69] IEEE Std 802.3™-2008, New York, USA, Dec. 2008.

[70] P. Vetter, "Next Generation Optical Access Technologies," *Proc. ECOC 2012*, paper Tu.3.G.1.

[71] Y. Ma, Y. Qian, G. Peng, X. Zhou, X. Wang, J. Yu, Y. Luo, X. Yan, and F. Effenberger, "Demonstration of a 40Gb/s Time and Wavelength Division Multiplexed Passive Optical Network Prototype System," *Proc. ECOC 2012*, paper PDP5D.7.

[72] N. Cheng, 'Flexible TWDM PONs," *Proc. OFC 2014*, paper W1D.2.

[73] 3GPP, 3GPP TS 36.104 version 11.9.0 Release 11, 2014.

[74] C.-C. Wei, "Small-signal analysis of OOFDM signal transmission with DML and direct detection," *Opt. Lett.*, vol. 36, no. 2, pp. 151–153, 2011.

[75] Telesystem Innovations, "LTE in a Nutshell," 2010.

[76] X. Liu, F. Effenberger, N. Chand, L. Zhou, and H. Lin, "Efficient Mobile Fronthaul Transmission of Multiple LTE-A Signals with 36.86-Gb/s CPRI-Equivalent Data Rate Using a Directly-Modulated Laser and Fiber Dispersion Mitigation," *Proc. ACP 2014*, paper AF4B.5.

[77] L. Zhou, H. Lin, G. Peng, N. Chand, Z. Wang, F. Wang, and F. Effenberger, "A Novel Optical Access Network: Software-Defined FlexPON," *Proc. OECC 2014*, pp. 688-690.

[78] N. Cvijetic, A. Tanaka, P.N. Ji, K. Sethuraman, S. Murakami, and T. Wang, "SDN and OpenFlow for Dynamic Flex-Grid Optical Access and Aggregation Networks," *J.Lightw. Technol.*, vol. 32, no. 4, pp.864-870, Jul. 2013.

[79] ITU-T, Asymmetric digital subscriber line (ADSL) transceivers, Recommendation G.992.1, June, 1999.

VITA

Ming Zhu received the B.E. degree in Electronics and Information Engineering from Huazhong University of Science and Technology, Wuhan, Hubei, China, in 2010, and the M.S. degree in Electrical and Computer Engineering from the Georgia Institute of Technology. She is currently working toward the Ph.D. degree in the School of Electrical and Computer Engineering at the Georgia Institute of Technology. Her research focuses on radio-over-fiber system and related techniques, WDM-PON, and optical networks for next-generation mobile backhaul and fronthaul.